Università di Genova

DIFI DIPARTIMENTO DI FISICA

Università degli Studi di Genova

Doctoral School

Physics and Nanosciences

Doctoral Course

Physics

XXXVIII Cycle

Nanoparticle-membrane interactions: insights from biomimetic models

Candidate:

Beatrice Leonardini

Supervisors:

Prof. Annalisa Relini

Dr. Ester Canepa

03 June 2026

Le persone che riparano il mondo sono quelle che amano ciò che fanno, indipendentemente dalla grandezza di ciò che fanno.

L'arte di essere fragili
Alessandro D'Avenia

Abstract

Among technology-derived nanomaterials, engineered nanoparticles have been extensively studied to develop novel applications in biology and medicine, including cancer treatment, bioimaging, biosensing, tissue engineering, drug and gene delivery. The majority of these biomedical applications lead to the inevitable interaction between nanoparticles and the cell membrane, which is the first biological barrier that nanoparticles encounter once introduced into the organism. Understanding nanoparticle-membrane interaction mechanisms is therefore a priority in the field, both to investigate the effects of nanoparticle on cell structure and function and to explore their use as synthetic agents for biomedical applications. In this context, several studies have demonstrated that functionalized gold nanoparticles are promising tools due to their remarkable core stability, surface functionalization versatility and compatibility with biological systems.

This thesis investigates the interactions between biomimetic membranes and gold NPs with a sub-6 nm core, functionalized with an amphiphilic coating. Biomimetic membranes provide a controlled and simplified environment to capture molecular details of the interactions that could hardly be studied in real biological membranes, which are too complex. A biophysical approach was employed in this study, using fluorescence spectroscopy, optical microscopy, quartz crystal microbalance measurements, small angle X-ray scattering, dynamic light scattering and zeta potential analysis.

The physicochemical parameters governing gold nanoparticles as synthetic fusogenic agents were investigated using fluorescence assays and quartz crystal microbalance measurements, revealing how the nanoparticles can serve as a potential tool for artificial membrane fusion. Furthermore, the effects of nanoparticles on membrane properties were studied in different biomimetic systems to provide detailed and more complete insights into nanoparticle-membrane interactions. Changes in membrane morphology and permeability were investigated using optical microscopy on cell-sized vesicles. NP-membrane interaction in the presence of osmotic stress was studied using small angle X-ray scattering on small vesicles. Finally, in line with the aim of increasing biomimicry, an optimized protocol for asymmetric membranes with lipid compositions mimicking key features of eukaryotic cell membranes was developed, providing a platform for future studies of NP effects under biologically relevant conditions.

Overall, the findings of this work broaden our understanding of various aspects of nanoparticle-membrane interactions from a fundamental perspective, highlighting key factors that may be relevant for the potential applications of amphiphilic-coated gold nanoparticles.

Contents

Introduction

Over the last decades, interest in nano-sized materials has increasingly grown due to their wide range of applications in fields such as industry, food technology, environmental science, medicine, and pharmaceutical research [1–3]. At the nanoscale, materials exhibit physicochemical properties that differ from those of their bulk counterparts. These unique properties make nanomaterials attractive for new technological and biomedical applications, but also raise safety concerns, as their interactions with biological systems are not yet fully understood [3].

This thesis focuses on the properties and applications of amphiphilic-coated gold nanoparticles (AuNPs). Among the various types of synthetic surface-functionalized nanoparticles [4, 5], AuNPs have attracted significant attention due to their chemical stability, possibility of versatile surface modification and biocompatibility [6, 7]. The optimized design and functionalization of AuNPs are essential to ensure that their physicochemical properties (e.g., size, shape, material composition, and surface chemistry) are tailored to the specific applications and biological environments in which they are employed [8, 9].

The cell membrane plays a key role as the primary interface for NP-cell interactions. Cellular membranes are highly dynamic and complex structures that are essential for life, since they define the boundary between two distinct biological environments [10]. The presence of a membrane allows the formation of differentiated compartments containing various chemical species and biomolecules, within which specific chemical reactions can occur. Cellular compartmentalization is therefore fundamental for the proper functioning of all physiological processes within the cell.

The structure of the cell membrane was described by S. J. Singer and G. L. Nicolson in 1972 with the fluid mosaic model [11]. According to this model, membranes consist of an extremely thin ($\approx 5\,\mathrm{nm}$) phospholipid bilayer containing embedded proteins. The synergy between lipids and proteins ensures the membrane to play a crucial role in cellular communication, vesicle trafficking, selective transport of molecules, signal transduction, and

in maintaining the overall integrity and organization of the cell.

The bilayer structure allows the membrane to be flexible and deformable under mechanical stress, while maintaining selective permeability and compartmentalization. Its fluidity, lateral mobility of lipids, and intrinsic asymmetry between the inner and outer leaflets enable proper protein function, domain formation, and signaling. Moreover, the nanomechanical and geometric properties of the bilayer, including local elasticity and curvature, modulate critical cellular processes such as budding, fission, and fusion as well as interactions with external agents, such ad NPs.

The complexity of cellular membranes has led to the development and application of a wide range of model membrane systems for studying membrane physicochemical properties under controlled conditions. Model membranes (or biomimetic membranes) have a simplified composition compared to cellular membranes while reproducing the lipid bilayer structure. These systems allow the study of membrane interactions with other molecules such as drugs, proteins, peptides, and nanoparticles [12]. The widespread use of model membranes is also favored by their relative ease of preparation in the laboratory and their compatibility with many biophysical analysis techniques.

Among the different types of AuNPs, amphiphilic-coated AuNPs have been extensively studied as promising candidates for interactions with cellular membranes. Several investigations have focused on their cytotoxicity, their entry mechanisms through cell membranes [13] and and their non-disruptive interactions with the lipid bilayer [14]. However, despite the remarkable knowledge gained on these systems, a complete understanding of NP-membrane interactions and their potential applications is still far from being achieved.

In this context, this work provides novel contributions in the application of AuNPs as synthetic fusogenic agents and in the study of their interactions with increasingly biomimetic membrane models. To this end, amphiphilic AuNPs with varying core sizes were employed in combination with biomimetic vesicles of different curvatures and lipid compositions, allowing the exploration of interactions under conditions that progressively approximate biological complexity. A fundamental understanding of the nano-membrane interface can thus enable the rational design of tunable biomedical NPs with controlled behavior.

Thesis outline

The contents of this thesis are organized as follows. When experiments were performed thanks to collaborations, this is explicitly indicated at the beginning of each chapter.

Chapter 1 focuses on a general description of the cell membrane, presented as a structure based on a lipid bilayer formed through a self-assembly process. The different lipid species constituting the membrane are discussed. Subsequently, model membranes are described, with a focus on vesicle-based systems. In the second part, functionalized NPs and their applications in biomedicine are introduced, with particular emphasis on the

amphiphilic-coated gold NPs employed in the experiments presented in this work.

Chapter 2 provides a description of the experimental techniques used to investigate NP-membrane interactions. Each section presents a specific technique, describing the fundamental physical principles on which it is based. Fluorescence assays and quartz crystal microbalance with dissipation monitoring (QCM-D) measurements were used in the experiments described in Chapter 3, while optical microscopy was employed in Chapter 4. Small-angle X-ray scattering (SAXS) was used for experiments in Chapter 5. Dynamic light scattering (DLS) and zeta potential measurements were used to characterize both the NPs and the vesicles.

Chapter 3 describes the physical determinants that govern NP-mediated membrane fusion, with a particular focus on the interplay between AuNP size and vesicle curvature in modulating the fusion of lipid vesicles. To this end, amphiphilic AuNPs were used to induce fusion of zwitterionic lipid vesicles composed of fluid-phase phosphocholines (major components of cellular membranes) and a biologically relevant fraction of cholesterol. This chapter is based on the papers by Leonardini et al., *Nanoscale* (2025), and Leonardini et al., *Advances in Physics X* (2026).

Chapter 4 elucidates the interaction between AuNPs and cell-sized lipid vesicles that provide a powerful platform to probe NP-membrane interactions. Phosphocholine giant unilamellar vesicles were used to investigate morphological changes induced by AuNPs, an aspect that has been largely unexplored in interactions between these NPs and this type of model membrane. The micrometric size of giant vesicles allows direct observation of membrane morphologies at the single-vesicle level using confocal fluorescence microscopy.

Chapter 5 focuses on how membrane-embedded NPs influence bilayer permeability to water, driven by osmotic gradients across vesicle membranes. To probe this effect, SAXS was employed to assess vesicle size changes, which reflect volume variations resulting from water efflux or influx under different osmotic conditions.

Chapter 6 presents an optimization of a protocol for the preparation of asymmetric vesicles. In order to obtain more biomimetic models, membrane asymmetry is a key feature to be reproduced *in vitro*, as it plays an important role in many cellular functions. However, generating asymmetric vesicles remains experimentally challenging. This optimization contributes to the development of improved experimental methods for the preparation of asymmetric vesicles, which can be used in future experiments to study interactions with NPs, whose mechanisms have so far been poorly investigated in lipid membranes of such complexity.

Details on the materials and methods used for vesicle preparation are reported in **Appendix A**. An overview of AuNP synthesis and their characterization is provided in **Appendices B** and **C**.

CHAPTER 1

Lipid membranes and nanoparticles

This chapter introduces the main characteristics of lipid membranes and their interactions with synthetic surface functionalized NPs. It first provides a general overview of the cellular membrane in its native biological context and in simplified biomimetic model systems. Then the main properties of amphiphilic-coated AuNPs are introduced as well as their mechanisms of interaction with lipid membranes.

1.1 The cell membrane

The cell membrane (or plasma membrane) (Figure 1.1) is a thin boundary that separates the interior of the cell from the external environment and is present in all prokaryotic and eukaryotic cells. The membrane should be considered as a dynamic system rather than a static barrier. Despite its small thickness, its complex structure and composition, mainly lipids and proteins, regulate the selective transport of ions and chemical species essential for fundamental cellular processes into and out of the cell. As a selectively permeable barrier, the plasma membrane regulates cellular metabolism by controlling nutrient uptake and intercellular communication [15]. The plasma membrane can be considered as a two-dimensional elastic material. Its thickness is on the order of a few nm, while its lateral dimensions are on the order of µm. Eukaryotic cells typically have diameters in the range $(10 - 50)\,\mu m$, thus roughly modeling the cell as a sphere results in a plasma membrane surface area of approximately $(300 - 8000)\,\mu m^2$. This strong separation of length scales justifies the physical and mathematical treatment of the plasma membrane as a planar sheet. Moreover,due to its flexibility, the membrane is able to change its shape and adopt different morphologies depending on the its functions. Membrane shape changes can be naturally induced by thermal fluctuations or by applied forces. Typical processes involving membrane

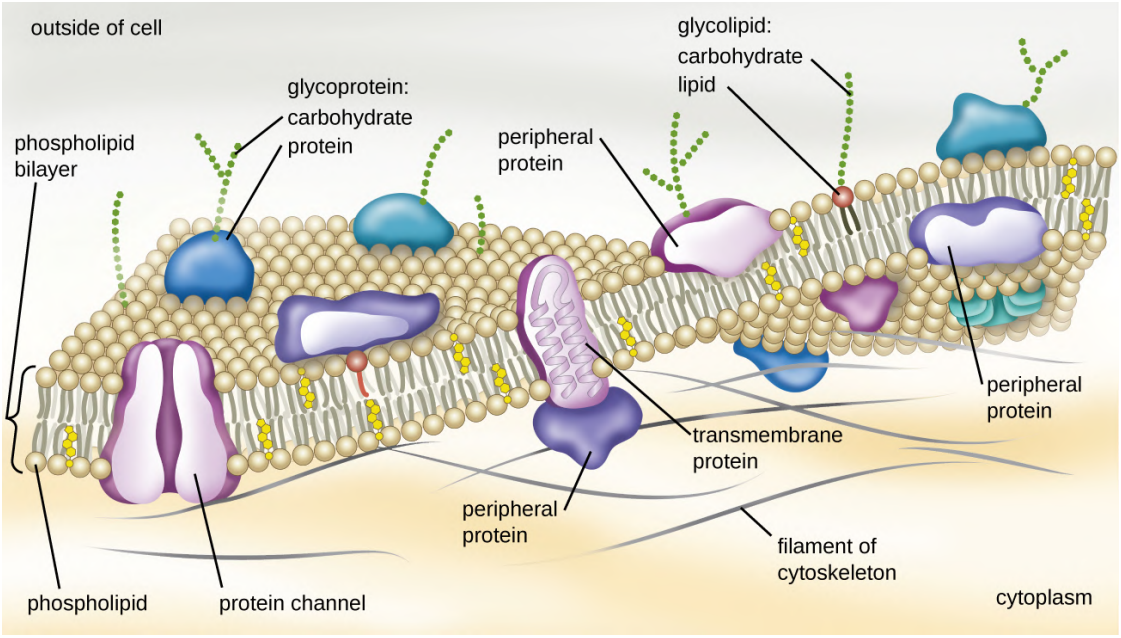

Figure 1.1 – ***Schematic representation of the plasma membrane of a eukaryotic cell.*** *The matrix of the membrane consists of a phospholipid bilayer embedding various protein molecules. On the inner leaflet, a network of filaments known as the cytoskeleton is anchored via specific proteins. Toward the extracellular space, carbohydrate chains extend from the membrane surface. Cholesterol molecules (in yellow) are also present and play a fundamental structural role.*

deformations include budding and fusion. The properties of biological membranes depend on the physicochemical properties of their constituents. As previously mentioned, the main components of biological membranes are lipids, molecules characterized by a hydrophilic region, referred to as the polar head, and a hydrophobic region, known as the apolar tail. For this reason, lipids are classified as amphiphilic or amphipathic molecules. This molecular structure allows lipids, at specific concentrations, to interact with water and spontaneously organize into different structures, including bilayers [16].

1.1.1 Lipid composition

Biological membranes are asymmetric and heterogeneous structures. The monolayers that make up the membrane, also called leaflets, are classified as outer and inner leaflets, depending on whether they face the extracellular environment or the cytosol, respectively. In these two leaflets, both the quantity and type of lipids present are different. This type of asymmetry is known as transverse asymmetry. In addition, the presence of lipid aggregations and clusters along the membrane plane results in lateral heterogeneity [12, 17].

Under physiological conditions, membrane lipids undergo a variety of motions, some of which are extremely rapid. These include molecular vibrations occurring on timescales of approximately $(10^{-14} - 10^{-12})$ s, as well as rotational diffusion on the order of 10^{-9} s. Lateral diffusion of lipids within the same monolayer is also fast, taking place on timescales ranging

from $(10^{-10} - 10^{-6})$ s to cover distances in the range of a few nanometers up to hundreds of nanometers [18]. In contrast, transverse diffusion (or flip-flop) is much slower, typically occurring on timescales from 10^3 s to hours or even days. Indeed, this process involves the passage of polar head groups through the hydrophobic core of the membrane, making it energetically unfavorable. [19]. The asymmetric distribution of lipids in the membrane is essential for proper cell function. For example, in eukaryotic cells, the carbohydrate groups of glycolipids are always oriented toward the exterior of the plasma membranes, where they participate in molecular recognition processes. *In vivo*, the lipid asymmetry is actively maintained by ATP-dependent proteins called flippases and floppases. Defects in these proteins can disrupt cellular processes and contribute to pathological conditions [20].

The three main classes of plasma membrane lipids are glycerophospholipids, sphingolipids, and sterols [20, 21]. In mammalian cells, the outer leaflet is enriched in phospholipids and choline-containing sphingolipids, while the cytoplasmic leaflet mainly contains amine-containing phospholipids (Figure 1.2).

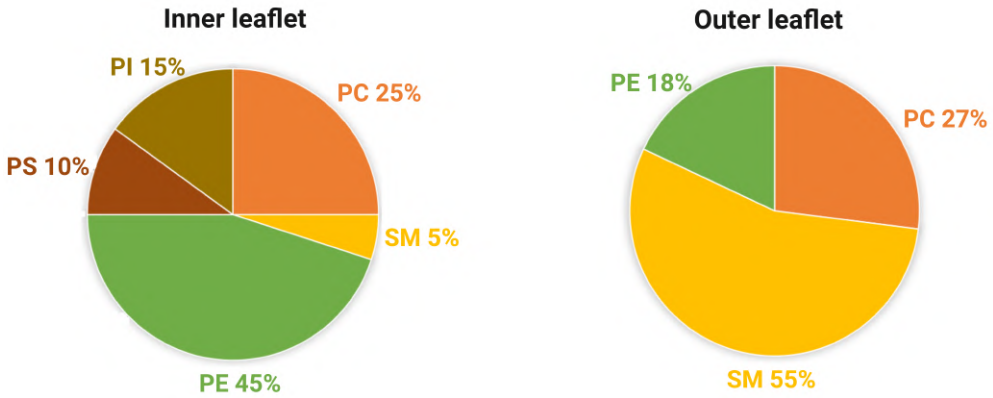

Figure 1.2 – *Percentage distribution of phospholipids in the inner and outer leaflets of the human erythrocyte membrane, including phosphatidylcholine (PC), phosphatidylethanolamine (PE), phosphatidylserine (PS), phosphatidylinositol (PI), phosphatidylglycerol (PG), and sphingomyelin (SM). Adapted from Pignatello et al [22].*

Glycerophospholipids (GPLs) are the most abundant lipids in cell membranes. As shown in Figure 1.3, they consist of two fatty acids of varying composition esterified to glycerol, which is in turn linked to a phosphate group, forming phosphatidic acid. Several alcohol groups can be esterified to the phosphate group, defining the specific type of GPL. Depending on the substituent, phosphatidylcholine (PC), phosphatidylethanolamine (PE), phosphatidylserine (PS), phosphatidylinositol (PI), phosphatidylglycerol (PG) can be obtained. This group of molecules is generally referred to as phosphatides. A broader variety of glycerophospholipids exists. They differ not only in the polar head group but also in the structure of the acyl chains, which can be saturated (without double bonds) or unsaturated (with one or more double bonds), and have double bonds at different positions[1]. The nature of fatty acids strongly influences the physicochemical properties of phospholipids and the membrane behavior.

[1]To compactly indicate the structure of a fatty acid, the notation (XX:Y, n-Z) is used, where XX is the

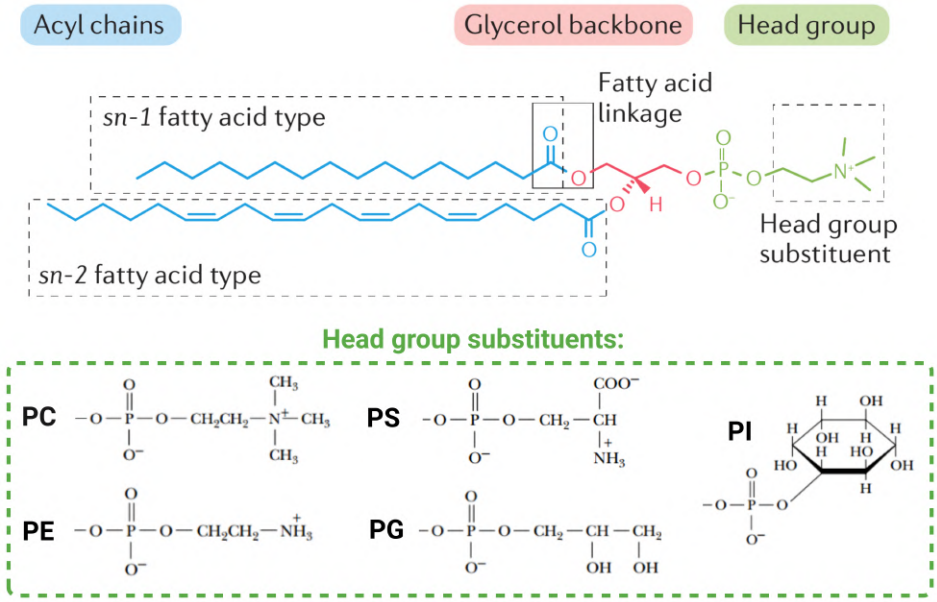

Figure 1.3 – ***Schematic of a glycerophospholipid, and its building blocks.*** *The first block (blue) represents the two fatty acids forming the hydrophobic tails of the phospholipid, esterified to glycerol. Glycerol is shown in pink, linked to the polar head group composed of the phosphate and alcohol groups (green). The main headgroup substituents are represented in the green frame. Adapted from [21].*

Sphingolipids (SLs) are mainly present in the outer leaflet of the plasma membrane. The backbone of sphingolipids is the sphingoid base, which also constitutes one of the two hydrophobic chains of the lipid (Figure 1.4). The main mammalian sphingoid bases are dihydrosphingosine (DHS) and sphingosine (SPH), while DHS and phytosphingosine (PHS) are the main bases in yeast. Typically, a fatty acid is attached to sphingosine via an amide bond, forming ceramide. The lipid head group is then attached to ceramide, and depending on the molecule, the sphingolipid is named accordingly. Different sphingolipid species are distinguished by the sphingoid base, the acyl chain, and the head group.

Sphingomyelins are fundamental for the nervous tissue of higher animals and represent a subclass of phosphorus-containing sphingolipids, in which phosphocholine is esterified to ceramide. Another class of molecules derived from ceramides, present in the membranes of mammalian nervous and muscle tissues, are glycosphingolipids. These consist of a ceramide linked to one or more sugar residues (Figure 1.5**a**). More complex lipids in this category are gangliosides, consisting of a ceramide backbone with three or more esterified sugars, which carry a net negative charge at neutral pH. In plasma membranes, glycosphingolipids are present at lower concentrations compared to other lipid classes and are mainly involved in cell-cell recognition. In particular, gangliosides, which are located in the outer leaflet of cellular membranes, especially in neurons, play a key role in modulating membrane protein function, ion channels, and cellular communication [23] [24].

number of carbon atoms in the chain, Y is the number of double bonds, and Z is the position of the first double bond counting from the ω terminal carbon.

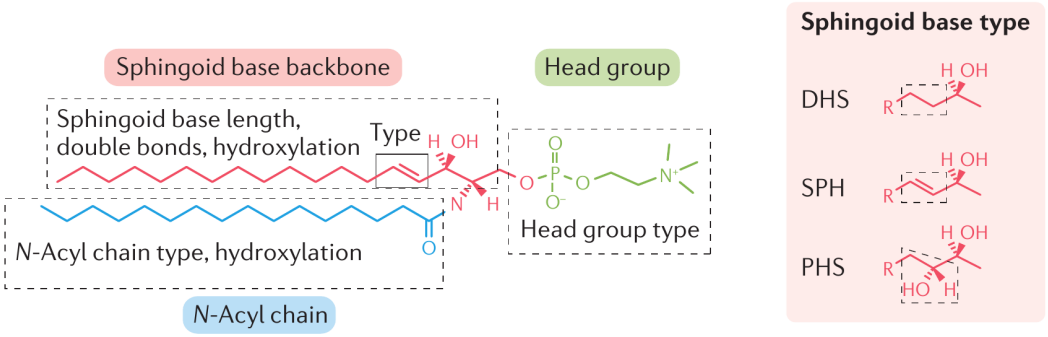

Figure 1.4 – ***Schematic of a sphingolipid, and sphingoid bases***. *Sphingosine (pink) is a carbon amino alcohol that replaces glycerol in glycerophospholipids. Through an amide bond, a fatty acid (N-acyl chain, blue) is attached to sphingosine. These two blocks together form ceramide, to whose the lipid head group is attached (green). The pink inset on the right shows the three sphingoid bases: dihydrosphingosine (DHS), sphingosine (SPH, shown on the left), and phytosphingosine (PHS). Adapted from [21].*

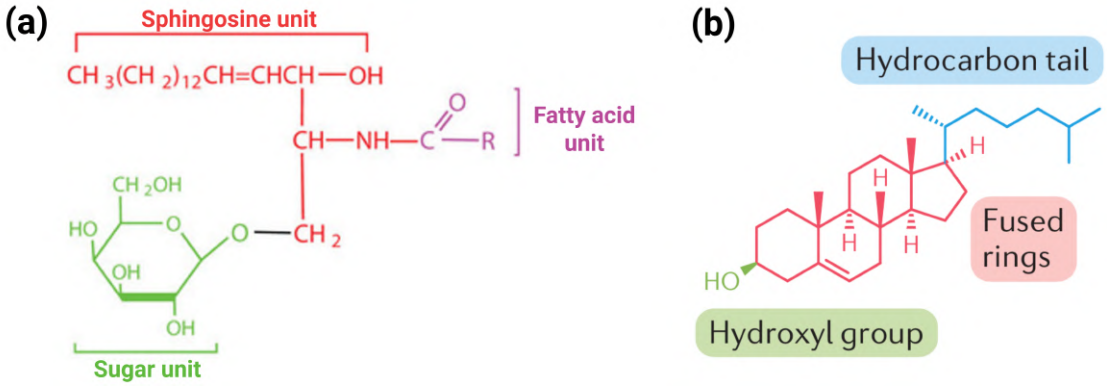

Figure 1.5 – **(a)** *Schematic representation of a glycosphingolipid. One or more head groups (sugar units) can be attached to ceramide, exhibiting different configurations depending on the sugar composition.* **(b)** *Cholesterol consists of 4 steroid rings (pink), with a hydroxyl group (green), two methyl groups, and a carbon aliphatic chain. Adapted from [21].*

Among sterols, cholesterol (chol) is the most abundant in eukaryotic plasma membranes. Its structure is shown in Figure 1.5**b**. Cholesterol consists of three six-membered rings and one five-membered ring, a hydroxyl group, and a hydrophobic side chain. The relatively rigid ring system and weakly polar hydroxyl group have fundamental structural consequences on membranes. Cholesterol positions itself roughly parallel to the acyl chains of phospholipids and perpendicular to the membrane plane, being almost completely immersed in the hydrophobic region of the bilayer, forming a hydrogen bond between its hydroxyl group (green in Figure 1.5) and the carbonyl oxygen of the adjacent phospholipid. Under physiological conditions, the interaction between cholesterol and fatty acids modifies the bilayer behavior, preventing chain crystallization on one hand and reducing fluidity on the other. Furthermore, by making the membrane less deformable, it also decreases its permeability to small polar molecules [22].

1.1.2 Lipid bilayer self-assembly

Lipids belong to a broader class of molecules known as amphiphilic molecules, including surfactants, some copolymers, and proteins. The feature shared by all these compounds is their ambivalent behavior in aqueous environments, which leads them to spontaneously form complex structures in order to minimize the free energy of the system. This is achieved by avoiding exposure of the hydrophobic regions to water, keeping the hydrophobic moieties in contact, and exposing the hydrophilic groups to the surrounding medium. As a consequence of the hydrophobic effect, aggregates such as micelles (spherical or cylindrical), bilayers, and vesicles are formed. Depending on the conditions of the aqueous solution, these aggregates can transform into one another, for example in response to changes in pH, temperature, ionic strength, or amphiphile. The intermolecular interactions within these aggregates are predominantly weak interactions, including van der Waals forces, hydrogen bonding, hydrophobic and electrostatic interactions.

In the following sections, the general thermodynamic principles leading to the aggregation of molecules in solution will be discussed, followed by an analysis of the geometric characteristics of amphiphilic molecules that determine the variety of possible aggregate morphologies [25, 26].

Critical Micelle Concentration (CMC). Consider a solution containing identical solute molecules that aggregate into structures, and let N be the aggregation number, i.e., the number of molecules forming each structure ($N = 1, 2, 3, ...$). Let X_N be the volume fraction of molecules found in aggregates of aggregation number N, and let C be the total solute concentration,

$$C = \sum_{N=0}^{\infty} X_N \, . \tag{1.1}$$

The chemical potential of a molecule within a structure of aggregation number N is:

$$\mu_N = \mu_N^0 + \frac{k_B T}{N} \log \frac{X_N}{N} \tag{1.2}$$

where μ_N^0 is the free energy per molecule in an aggregate of N molecules. The total energy per aggregate is $N\mu_N^0$. Equations (1.1) and (1.2) completely define the system. At thermodynamic equilibrium, all molecules have the same chemical potential. Considering two generic aggregates of size M and N:

$$\mu_N^0 + \frac{k_B T}{N} \log \frac{X_N}{N} = \mu_M^0 + \frac{k_B T}{M} \log \frac{X_M}{M} \tag{1.3}$$

from which the distribution function for X_N is obtained:

$$X_N = N \left\{ \frac{X_M}{M} \exp \left[M \frac{(\mu_M^0 - \mu_N^0)}{k_B T} \right] \right\}^{\frac{N}{M}} \tag{1.4}$$

which can have maxima at multiple values of N. Setting $M = 1$ and rewriting the relation:

$$X_N = N \left\{ X_1 \exp \frac{\mu_1^0 - \mu_N^0}{k_\mathrm{B}T} \right\}^N \tag{1.5}$$

it can be concluded that the necessary condition for forming large stable aggregates is $\mu_N^0 < \mu_1^0$ for some values of N. This condition can be met if μ_N^0 is a decreasing function of N, or if μ_N^0 has a minimum for some N. For simple geometries (cylinders, planes, spheres), a general function for μ_N^0 can be written:

$$\mu_N^0 = \mu_\infty^0 + \frac{\alpha k_\mathrm{B}T}{N^p} \tag{1.6}$$

where $-\alpha k_\mathrm{B}T$ is the monomer-monomer binding energy relative to isolated monomers in solution ($\alpha > 1$ generally) and p is the inverse of the aggregate dimensionality ($p = 1, 1/2, 1/3$ for 1D, 2D, 3D aggregates, respectively). Substituting Eq. (1.6) into Eq. (1.5) gives an expression for X_N:

$$\begin{aligned} X_N = N \left\{ X_1 \exp \frac{\mu_1^0 - \mu_N^0}{k_\mathrm{B}T} \right\}^N = \\ = N \left\{ X_1 \exp \left[\alpha \left(1 - \frac{1}{N^p} \right) \right] \right\}^N \simeq N \left\{ X_1 \, \mathrm{e}^\alpha \right\}^N \ . \end{aligned} \tag{1.7}$$

For low monomer volume fractions X_1, such that $X_1 \, \mathrm{e}^\alpha \ll 1$, we have $X_1 > X_2 > \ldots > X_N$, so that $X_1 \simeq C$. Since X_N must always be less than unity, when $X_1 \simeq \mathrm{e}^{-\alpha}$, all added monomers cannot remain isolated in solution and therefore aggregate. If μ_N^0 follows the monotonically decreasing function in Eq. (1.6), there is always a critical value $(X_1)_\mathrm{c} = \mathrm{CMC} \simeq \mathrm{e}^{-\alpha} \ \ \forall p$, where isolated molecules coexist with an aggregate. This critical value is called the critical aggregation concentration (CAC), or more commonly the critical micelle concentration (CMC) (Figure 1.6).

Geometric Packing Parameters. Different types of amphiphilic molecules exist and can exhibit several physicochemical properties, depending on the size and charge of their polar heads, the length of their apolar chains, and the number of chains. In general, despite the complexity of these molecules, relatively simple geometric parameters can be defined to determine the type of aggregate that can form from a given amphiphilic molecule.

These parameters correspond to the optimal polar head area a_0, the critical hydrophobic tail length l_c (the maximum length the chain can adopt), and the volume of the hydrocarbon tails v. As shown in Figure 1.7, two fundamental opposing forces act at the water-hydrocarbon interface and determine the optimal area per molecule at equilibrium. The repulsive force between polar heads tends to push them apart to maximize exposure to the aqueous phase (energetically favorable), and the attractive interfacial force tends to reduce the area per

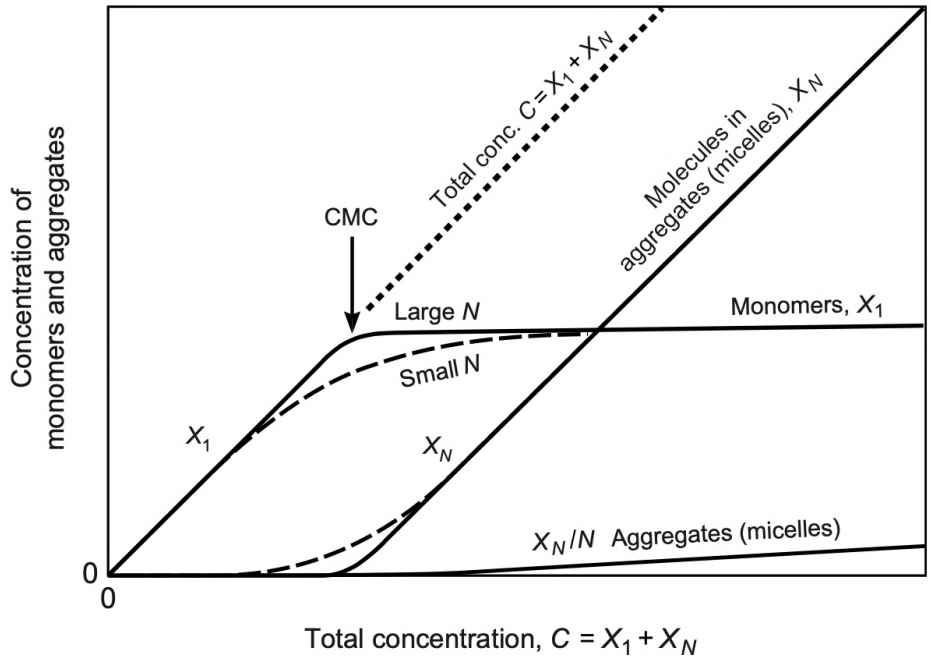

Figure 1.6 – *The graph shows the volume fraction of monomers (X_1) and aggregates of aggregation number N (X_N) as a function of the total solute concentration C. The transition occurs at the CMC, below which the solute exists in the isolated monomer state, and above which aggregates begin to form. For large N, the transition is sharper compared to smaller N (dashed line). Reprinted with permission from [25]. Copyright (2011), Elsevier Inc.*

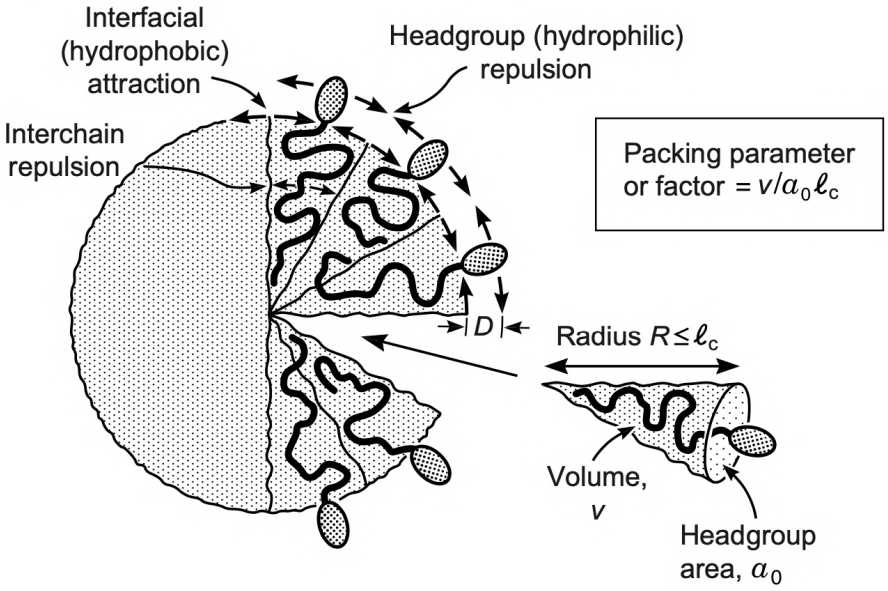

Figure 1.7 – *Representation of general geometric parameters that describe an amphiphilic molecule and the intermolecular forces and hydrocarbon-water interface forces. The balance between the repulsive forces between polar heads and the attractive hydrophobic forces at the interface determines the optimal area a_0, at which the free energy μ_0^N reaches a minimum. Reprinted with permission from [25]. Copyright (2011), Elsevier Inc.*

molecule to minimize exposure of hydrophobic tails to water. The total interfacial free energy μ_N^0 can be written as a function of the area per molecule a, accounting for the attractive and repulsive contributions:

$$\mu_N^0 = \gamma a + \frac{K}{a} \tag{1.8}$$

where γ is the interfacial tension and K is a constant. Differentiating gives the optimal area corresponding to the minimum interaction energy per lipid molecule:

$$\mu_N^0(\text{min}) = 2\gamma a_0 \ , \qquad \text{with } a_0 = \sqrt{\frac{K}{\gamma}} \ . \tag{1.9}$$

Finally, Eq. (1.8) can be rewritten in terms of a_0 to obtain a relation for the free energy in terms of known and measurable parameters:

$$\mu_N^0 = 2\gamma a_0 + \frac{\gamma}{a}(a - a_0)^2 \tag{1.10}$$

A dimensionless parameter called the critical packing parameter $P_c = v/(a_0 l_c)$ can be defined, which determines the aggregate geometry for a given molecule. Changing external conditions (e.g., salt concentration affecting electrostatic forces) can alter this factor. In Figure 1.8, P_c values, amphiphilic molecules shapes and the corresponding aggregates are shown. Amphiphilic molecules that tend to form bilayers have hydrocarbon tails occupying roughly twice the volume per $a_0 l_c$ compared to molecules forming spherical micelles. Therefore, molecules best suited for bilayer formation are those with double hydrocarbon tails. Phospholipids, the most abundant class of lipids in cell membranes, have this characteristic. The presence of double tails increases lipid hydrophobicity, and the CMC ranges between 10^{-10} M and 10^{-6} M, lower than for micelle-forming molecules. Furthermore, Eq. (1.6) can be rewritten with $p = 1/2$:

$$\mu_N^0 = \mu_\infty^0 + \frac{\alpha k_\text{B} T}{\sqrt{N}} \tag{1.11}$$

which, when substituted into Eq. (1.5), gives

$$X_N = N(X_1 \, \mathrm{e}^\alpha)^N \exp\left[-\alpha N^{1/2}\right] \tag{1.12}$$

Above the CMC, when $\mathrm{e}^\alpha \approx 1$, as N increases, the concentration X_N of aggregates of size N decreases exponentially, so that each added lipid aggregates into a planar sheet. The formation of theoretically infinite lipid bilayers is energetically unfavorable in aqueous environments, as hydrophobic edges would remain exposed. This drives bilayers to close onto themselves, joining exposed hydrophobic regions, forming vesicles. This process introduces curvature to the bilayer and requires energy, which must be included in the overall energy balance. Both planar bilayers and vesicles serve as models for studying biological membranes.

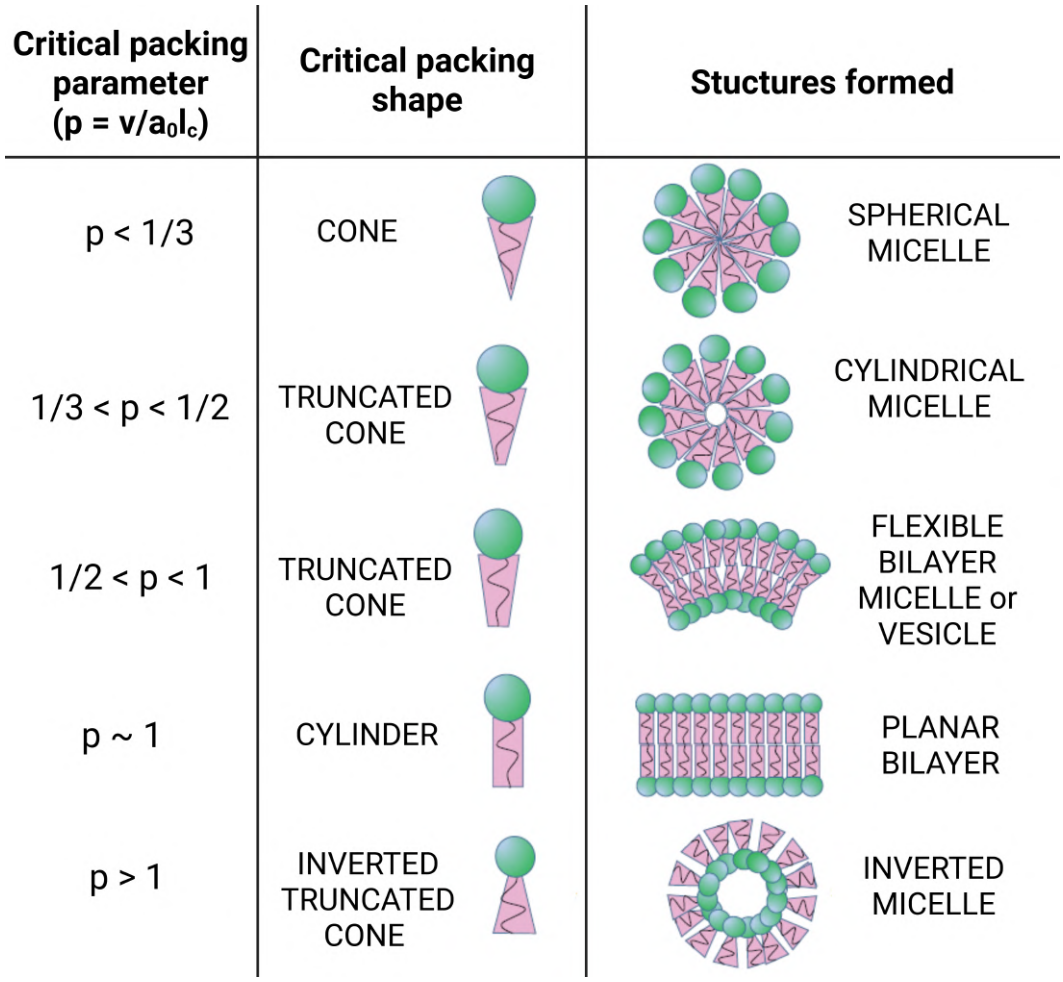

Figure 1.8 – *Packing parameters, packing shapes, and corresponding aggregate structures.*

The fluidity of a membrane depends on its phospholipid composition, cholesterol concentration, and physicochemical parameters of the environment, such as pH, ionic strength, and temperature. The hydrocarbon tails can bend and fold, adopting different orientations depending on the chain length and degree of unsaturation. At low temperatures, lipids are highly ordered and form a gel phase, in which the chains are fully extended, the surface area per lipid is minimal, and bond rotations are restricted. In most cases, increasing the temperature leads to phase transition. In particular, the system shifts from the gel phase or solid-ordered phase (S_o) to a liquid-crystalline or liquid-disordered phase (L_d). This results in increased chain disorder and higher membrane fluidity (Figure 1.9).

The temperature at which the phase transition occurs is called the transition or melting temperature (melting temperature, T_m) [27]. The transition is an endothermic and collective process, during which heat is absorbed by the lipid system and the behaviour of a few molecules influences that of nearby molecules. In heterogeneous membranes, a sufficient amount of sphingolipids and cholesterol induces a third structural phase in the bilayer, called the liquid-ordered phase (L_o), which exhibits acyl chain ordering typical of S_o, but rotational

(molecular orientation) and lateral (molecular position) diffusion similar to that of the L_d state. Below the transition temperature ($T < T_m$), when the system is in the solid-ordered state, cholesterol increases membrane fluidity by reducing acyl chain packing due to its rigid planar structure. Conversely, for $T > T_m$, cholesterol decreases membrane fluidity; its rigid hydrophobic portion intercalates the hydrocarbon chains in their fluid state, promoting a more ordered configuration [28] [29].

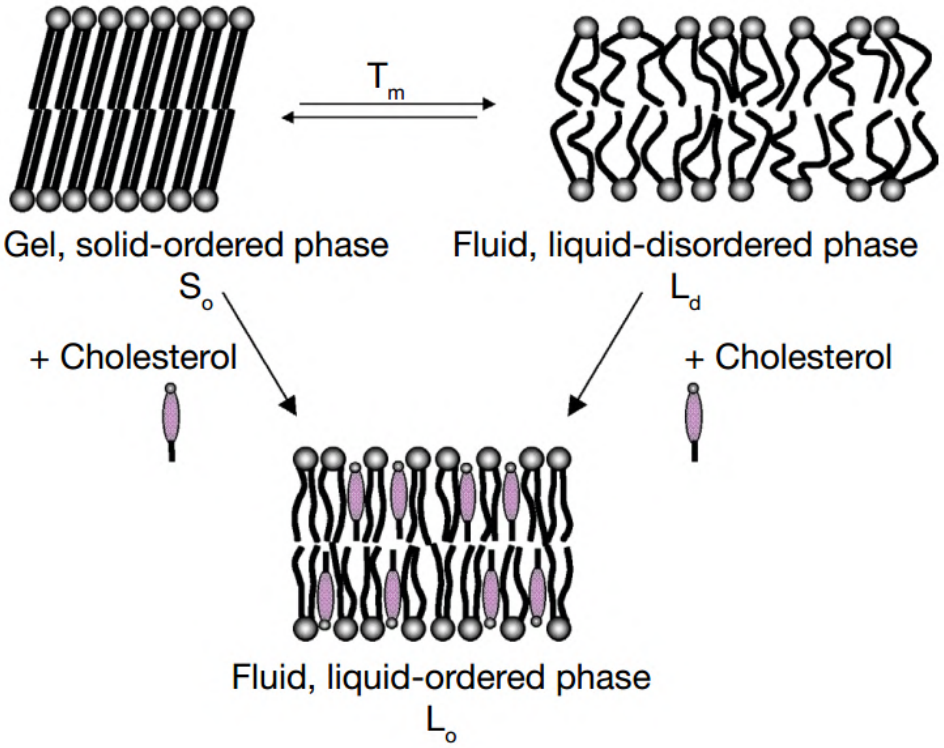

Figure 1.9 – ***Phase transitions in lipid bilayers.*** *The main transition occurs between the gel phase and the liquid-disordered phase, with the melting temperature indicated as T_m. In both the gel and liquid-disordered phases, the addition of cholesterol modifies membrane structure and gives rise to a third structural phase called the liquid-ordered phase. Adapted from [30].*

1.2 Membrane models

Cell membranes are systems that are very difficult to study directly in their native state. Therefore, since the last century, simpler membrane models have been developed to mimic the lipid organization of membranes in their fundamental components. Model membranes are used to investigate the structure and properties of cellular membranes, as well as their interactions with biomolecules (e.g., proteins) and synthetic compounds (e.g., surfactants, drugs and NPs) [31]. The most commonly known and used biomimetic systems can be divided into two categories: model membranes on surfaces and model membranes in solution.

Each of these systems has advantages and limitations, and the choice of the system depends on the phenomenon under study as well as the experimental technique used.

Supported lipid membranes. Supported membranes include lipid monolayers at the air-water interface and supported lipid bilayers (SLBs). Monolayers at the air-water interface are typically prepared by spreading lipids from an organic solution at an aqueous surface. Since these model membranes consist of a single layer, they are often used to study lateral lipid diffusion, since the mobility of molecules is close to that in biological membranes. In the case of SLBS, lipids are arranged with the polar heads of the first monolayer in contact with the substrate (e.g., mica, glass, silicon dioxide), while the hydrocarbon tails are in contact with the tails of the next monolayer, which exposes its heads to the external aqueous environment. The flat topology of SLBs makes them ideal for surface-sensitive techniques such as total internal reflection fluorescence microscopy, reflectometry and diffraction, Langmuir isotherms, QCM-D, and atomic force microscopy. However, strong interactions with the solid support may restrict lipid and protein mobility, denature large transmembrane proteins and affect membrane mechanics and curvature. Variants such as polymer-cushioned SLBs [32] or pore-spanning membranes [33] can partially reduce these drawbacks by decoupling the bilayer from the support.

Small and large unilamellar vesicles. Vesicles are spherical compartments composed of one or more lipid bilayers. In these structures, the membrane is in contact with water both inside and outside. Multilamellar vesicles (MLVs) are composed of several concentric bilayers forming an onion-like structure, while unilamellar vesicles are formed by a single lipid bilayer. Various protocols describe the preparation of vesicles depending on the size. Small and large unilamellar vesicles (SUVs and LUVs) are bilayer vesicles of approximately 50 nm (SUVs) and 50 nm (LUVs) in diameter. Their small size results in highly curved membranes, especially in SUVs. Standard methods for vesicle production typically result in symmetric bilayers, so that the inner and outer monolayers have the same lipid composition. Recently, protocols have also been developed to produce asymmetric vesicles [34]. SUVs and LUVs are not optically resolvable with conventional microscopy, so experiments are typically conducted in bulk using ensemble fluorescence spectroscopy, scattering techniques (e.g., neutrons, X-rays) [35, 36], nuclear magnetic resonance (NMR), electron paramagnetic resonance, and calorimetric techniques. SUVs and LUVs are straightforward to prepare in large quantities with defined compositions. Their main advantages include high reproducibility, suitability for high-throughput assays, and compatibility with reconstitution of fusion proteins and incorporation of NPs. However, their ensemble nature averages over many events, making it difficult to resolve transient intermediates and rare events.

Giant unilamellar vesicles. Giant unilamellar vesicles (GUVs) are cell-sized lipid compartments with diameters typically in the range $(5-100)\,\mu m$. GUV membranes are effectively planar and closely mimic the geometry and mechanical properties of cellular plasma membranes, making them an ideal platform for investigating interactions with external agents

such as NPs. Their principal advantage is that they can be directly observed using optical microscopy. In addition, their large size enables real-time visualization of membrane processes at the single-vesicle level. GUVs can be mechanically and chemically manipulated using techniques such as micropipette aspiration, optical tweezers, electric fields, and microfluidic approaches, providing fine control over membrane tension, curvature, and environmental conditions [37–39]. As a result, GUVs are particularly suited for investigating membrane morphology changes, including budding and tubulation, as well as for quantitative measurements of mechanical parameters such as bending rigidity and membrane tension [40]. In addition, GUV-based experiments generally require smaller amounts of lipid material compared to SUV/LUV preparations. Despite these advantages, GUV preparation protocols can result in low production efficiencies, depending on lipid composition.

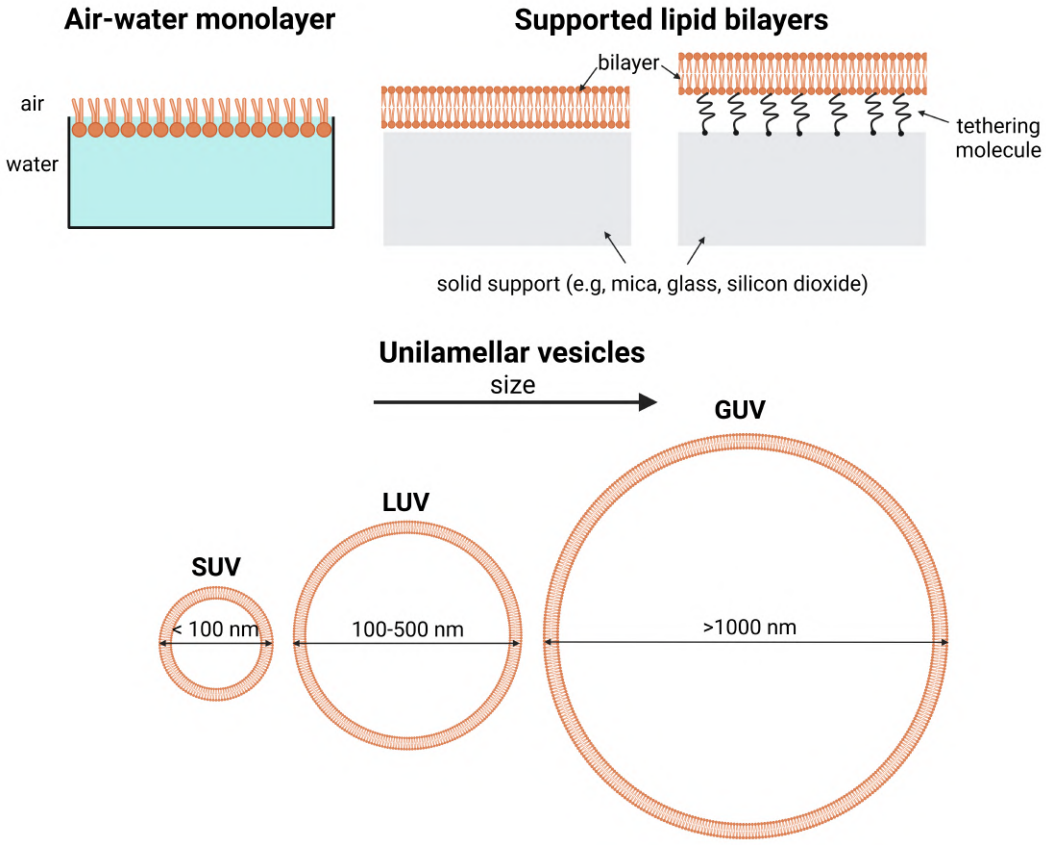

Figure 1.10 – *Examples of model membranes on surfaces (air-water monolayer, SLBs) and in solution (unilamellar vesicles of increasing size). Created in Biorender.*

For the experiments presented in this thesis, I prepared and used vesicles of different sizes. In particular, symmetric SUVs and LUVs were employed in Chapters 3 and 5, symmetric GUVs in Chapter 4, and MLVs and LUVs in Chapter 6.

1.3 The NP-membrane interface

Synthetic surface functionalized NPs have become key tools in a wide range of modern technological applications, due to their unique physicochemical properties arising at the nanoscale. Typically, NPs have sizes in the range $(1 - 200)$ nm, a scale at which materials exhibit a markedly high surface area-to-volume ratio. This feature leads to enhanced surface reactivity and to size-dependent optical, magnetic, and electronic properties that are not observed in bulk materials [7, 41–43].

In this thesis, the focus is on the interaction between NPs and cellular membranes. Therefore, particular attention is given to biomedical applications, where NPs are widely used in medical imaging, diagnostics, therapy, and drug delivery [44–47]. AuNPs, iron oxide NPs and quantum dots are employed to enhance contrast in imaging techniques such as fluorescence imaging, magnetic resonance imaging, enabling more efficient disease detection [6, 48, 49]. In addition, certain metallic NPs such as silver or copper exhibit strong antimicrobial activity and are used in medical devices to prevent infections [50]. In cancer treatment, inorganic NPs are widely used in strategies such as photothermal therapy, allowing localized treatment of tumors with improved efficiency [51, 52]. Functionalized NPs can also be used as carriers for the delivery of therapeutic molecules (e.g, chemotherapeutic agents and drugs) directly to specific tissues or cells, reducing side effects [53, 54]. Understanding the physicochemical factors governing NP-membrane interactions is therefore essential for the rational design of safe and efficient NPs. Their main advantage lies in their tunable physicochemical properties, which enable precise control of their behavior with biological systems both *in vitro* and *in vivo*. Key structural parameters of NPs regulating their interactions at the NP-membrane interface include the material, size, shape of the NP core, and the surface functionalization [55, 56] (Figure 1.11).

The material of the NP core determines its intrinsic functional properties of the NPs, such as optical absorption, magnetic response, catalytic activity and biocompatibility. In addition, NP size and shape influence cellular uptake mechanisms, membrane interactions, and subcellular trafficking [57, 58].

Among these parameters, surface functionalization represents a critical factor enabling the use of NPs in biomedical applications [59]. Due to their high surface free energy, bare NPs tend to be unstable, thus they are typically coated with ligands that form a stabilizing shell around the core. This coating is designed to ensure colloidal stability and solubility in aqueous solutions, as well as to direct the interactions of NPs within biological environments. Surface ligands can be engineered to provide electrostatic or steric stabilization, reduce nonspecific protein adsorption and enhance biocompatibility, Moreover, surface functionalization provides a versatile platform for further functional modifications, including the attachment of therapeutic cargo [60].

NPs can enter cells through different mechanisms, which are generally classified into

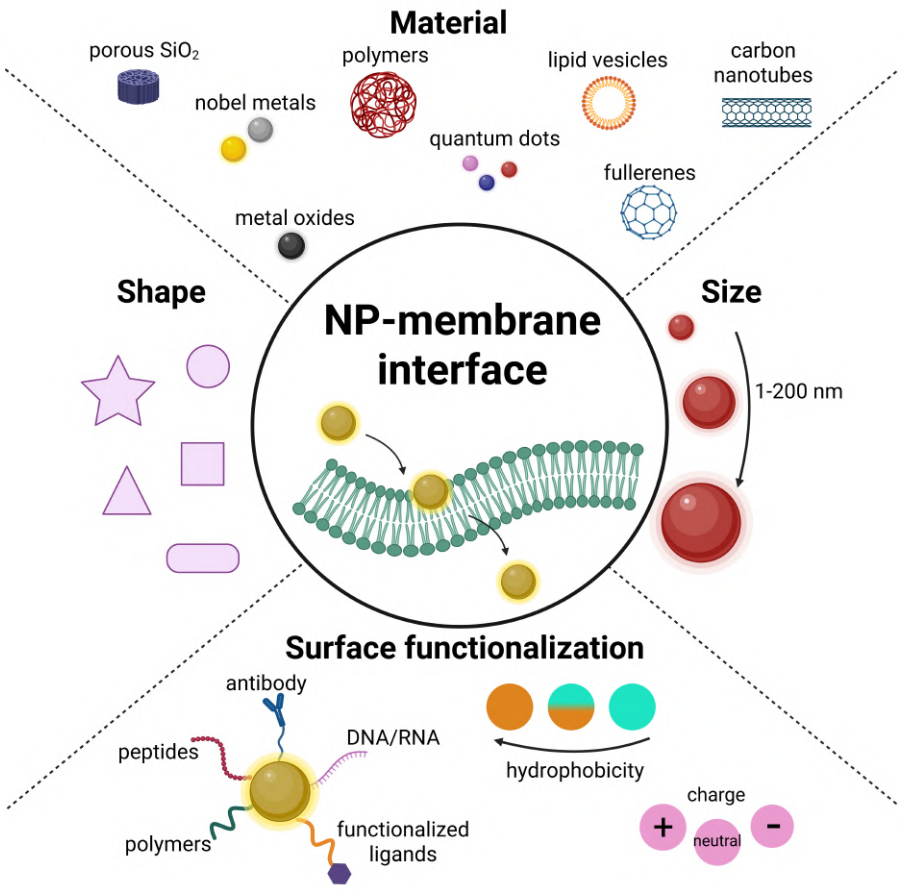

Figure 1.11 – *Schematic representation of the main physicochemical properties of NPs that govern their interactions with biological membranes. NP size, shape, surface properties (charge and hydrophobicity), and material composition influence interactions at the NP-membrane interface. Created in Biorender.*

passive and active processes [61–63]. These mechanisms have been studied both *in vivo*, using living cells, and *in vitro*, using model membrane systems. The specific pathway adopted depends on various factors, primarly the physicochemical properties of NPs (e.g., size, morphology, surface functionalization). In general, cellular internalization occurs via active, energy-dependent pathways, such as endocytosis, which can involve several mechanisms including clathrin-mediated endocytosis, caveolae-mediated endocytosis, macropinocytosis, and phagocytosis [64–67]. On the other hand, passive translocation includes the direct adsorption of NPs onto the membrane surface and their spontaneous penetration into the lipid bilayer [68]. Passive uptake does not require energy from the cell and is mediated by weak interactions between the cell membrane and NPs, such as van der Waals interactions, electrostatic interactions, hydrophobic forces, hydration forces, and also steric repulsion. Thermal fluctuations can also play a role in this process. Importantly, passive translocation can bypass endocytic pathways, preventing entrapment and potential degradation of NPs in endosomes, which is the major limitation of active, energy-dependent cellular internalization [69, 70]. Nevertheless, passive mechanism can lead to membrane damage, including the formation of pores [71].

1.3.1 Amphiphilic ligand-coated AuNPs

AuNPs have emerged as one of the most extensively studied systems in biomedicine due to the advantages offered by gold, including chemical inertness, resistance to oxidation, and excellent biocompatibility. Furthermore, AuNPs provide optical properties arising from localized surface plasmon resonance (LSPR), which enables strong absorption and scattering of light in the visible and near-infrared regions. These properties have been widely exploited for biomedical imaging, biosensing, surface-enhanced Raman scattering (SERS), and photothermal therapy [72]. In addition, the gold surface forms strong bonds with thiolated molecules (Au-S binding energy $(170 - 210)\,\mathrm{kJ\,mol^{-1}}$), enabling precise and versatile control over surface functionalization [6, 59, 73].

Figure 1.12 shows a schematic representation of the AuNPs used in this thesis, consisting of a gold core with a sub-6 nm diameter, functionalized with a mixture of amphiphilic ligands. These AuNPs were synthesized following a thiol-for-oleylamine ligand exange using a passivated thiol coating to obtain particles with diameters between $(2 - 6)\,\mathrm{nm}$, a size comparable to that of the lipid bilayer [74]. The amphiphilic coating is obtained by mixing the apolar alkylthiol *1-octanethiol* (OT) with the anionic thiol *11-mercapto-1-undecanesulfonate* (MUS), which contains an apolar alkyl chain and a charged terminal group, in a 2:1 molar ratio (MUS:OT). These NPs were synthesized by Dr. Ester Canepa during an internship in the group of Prof. Francesco Stellacci at EPFL (Lausanne, Switzerland). A general overview of AuNP synthesis is provided in Appendix B. Depending on the molar ratios used, these ligands determine both the colloidal stability in water and buffer solutions and the surface charge density of the NPs. Moreover, the small size of the NPs conferes to the linear alkyl chains on the NP surface significant ligand flexibility that facilitates the NP interaction with lipid membranes (as explained later).

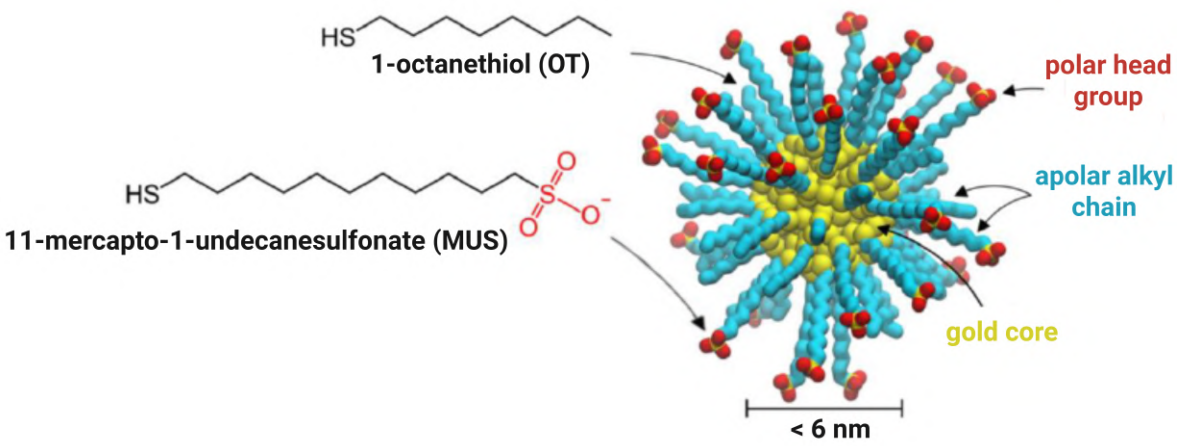

Figure 1.12 – *Cartoon of the amphiphilic AuNPs employed in the experiments described in this thesis. Anionic NPs were prepared using mixtures of MUS:OT. The sulfonate ($-SO_3^-$) terminal group provide electrostatic repulsion, ensuring colloidal stability in aqueous environments and defining the surface charge density of the NPs [74].*

In slico insights into passive NP penetration of amphiphilic AuNPs

The molecular details of MUS:OT NP insertion into lipid bilayers have been extensively studied using computational approaches, including both coarse-grained and atomistic molecular dynamics simulations [75–77]. These investigations indicate that the insertion mechanism is similar to the membrane incorporation of certain amphiphilic peptides such as cell-penetrating peptides (CPPs) [78] [79]. In particular, the hydrophobic and hydrophilic moieties on the NP surface can mimic key features of the natural structure of more complex amphiphilic proteins, whose amphipathicity and conformational flexibility are essential for non-specific interactions with membrane lipids [80]. The insertion of amphiphilic AuNPs into lipid bilayers is favored by the reduction in the hydrophobic ligand surface exposed to water when the NP comes into contact with the bilayer hydrophobic region. Nevetheless, the process initially appears energetically unfavorable because it involves the penetration of charged groups into the hydrophobic core of the bilayer. However, the small size of the AuNPS confers free volume available to each surface ligand, giving them high conformational flexibility. This flexibility allows ligands to reorganize upon membrane insertion, burying the apolar alkyl chains of both OT and MUS within the hydrocarbon region of the lipid tails, and exposing the charged sulfonate groups towards the polar aqueous interface. This ligand rearrangement, commonly referred to as *snorkeling*, enables the NP to adopt a stable anchored configuration within the membrane, which is further supported by local elastic deformation of the bilayer around the NP (Figure 1.13**a**) [75, 81].

Simulations indicate that this configuration is achieved through the sequential steps drived by the translocation of the charged terminal groups across the bilayer [82]. Each translocation step requires overcoming an energy barrier associated with the flipping of the charged groups across the membrane, to reach the final favorable entry state (Figure 1.13**b**). The energetic cost of this process depends on several factors, including ligand composition and structure on the NP surface, as well as membrane lipid composition.

An important factor governing the insertion pathway is the NP size. Ligand flexibility decreases with increasing core size, making the snorkeling rearrangement progressively more difficult. Conversely, larger NPs expose a greater hydrophobic surface area to water, which favors membrane embedding. Therefore, a favorable energetic configuration that is strongly dependent on the composition of the ligand mixture exists. An increase in the hydrophobic fraction of ligands broadens the NP size range that allows spontaneous insertion into lipid bilayers. For the 2:1 MUS:OT AuNPs used in this thesis, experimental and computational studies indicate that NPs with core sizes of approximately $(2-6)$ nm are the most effective at undergoing passive membrane penetration, whereas larger particles or particles with fully charged ligands tend to enter cells mainly through via endocytosis [13, 81, 83, 84].

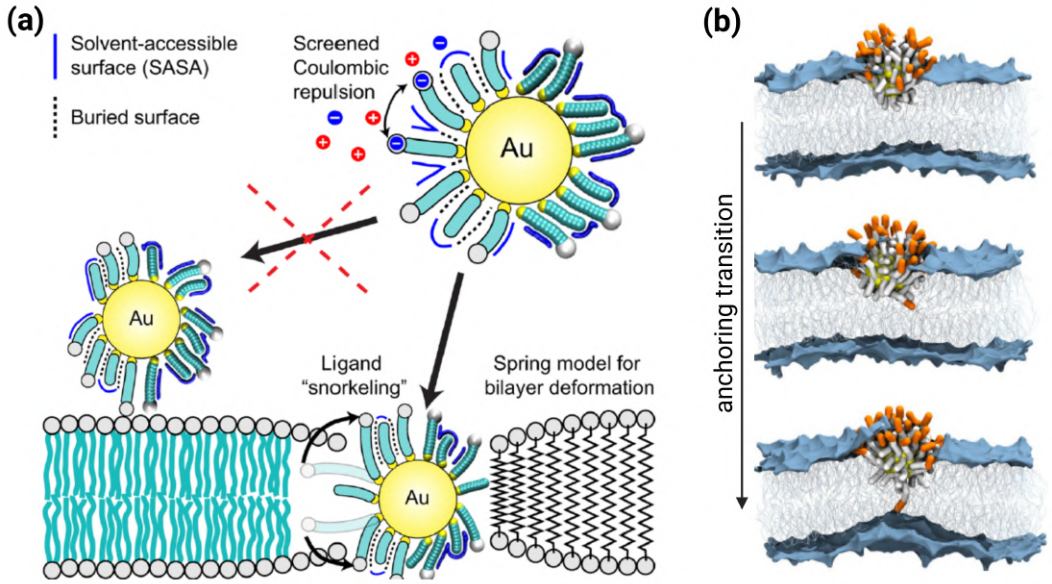

Figure 1.13 – **(a)** *The NP is passively incorporated into the bilayer, instead of remaining adsorbed on the membrane surface via electrostatic interactions. The final transmembrane state of the NP, stabilized by ligand snorkeling, is shown. The ligands rearrange to orient their charged groups out of the bilayer. The bilayer is modeled with a spring-like representation to illustrate its deformation around the NP during insertion. Reprinted with permission from Van Lehn et al [81]. Copyright (2013) American Chemical Society.* **(b)** *After the NP adsorbs onto the bilayer, hydrophobic contacts between the NP hydrophobic ligand surface and the lipid tails trigger partial embedding of the NP into the membrane core. A charged ligand (orange beads indicate the charged terminal groups) facilitates the anchoring transition. Reprinted from Canepa et al [14], licensed under CC BY 4.0.*

AuNPs interactions with lipid membranes

These AuNPs have been shown, both *in vitro* and *in vivo*, to spontaneously penetrate the cellular membrane of various mammalian cells through an energy-independent diffusion process without causing membrane disruption. Verma et al. [13] investigated the cellular uptake of MUS:OT AuNPs in dendritic cells (Figure 1.14**a**) and mouse embryonic fibroblasts at 37 °C and 4 °C. At physiological temperature, the NPs exhibited diffuse intracellular fluorescence, consistent with cytosolic localization. Notably, uptake was also observed at 4 °C, where energy-dependent processes such as endocytosis are suppressed, indicating that MUS:OT NPs can cross the plasma membrane via a passive, energy-independent mechanism.

Direct evidence of NP translocation across the plasma membrane was also obtained using erythrocytes, which are naturally non-endocytic cells [85]. In Figure 1.14**b**, erythrocytes incubated with MUS:OT NPs show diffuse intracellular fluorescence, while no calcein permeation is observed, indicating that the NP interaction does not disrupt the membrane. This suggests that the NPs can enter cells without compromising membrane integrity, achieving a homogeneous cytosolic distribution and avoiding leakage of small hydrophilic molecules. Similar investigations were extended to other cell types, including cancer cell lines [86].

These studies examined NP uptake at different temperatures and with different NP surface compositions, showing that membrane translocation can occur rapidly, often within a few minutes or even less [83]. In addition, these works confirmed that a MUS:OT molar ratio of approximately 2:1 represents the most favorable composition for efficient membrane insertion.

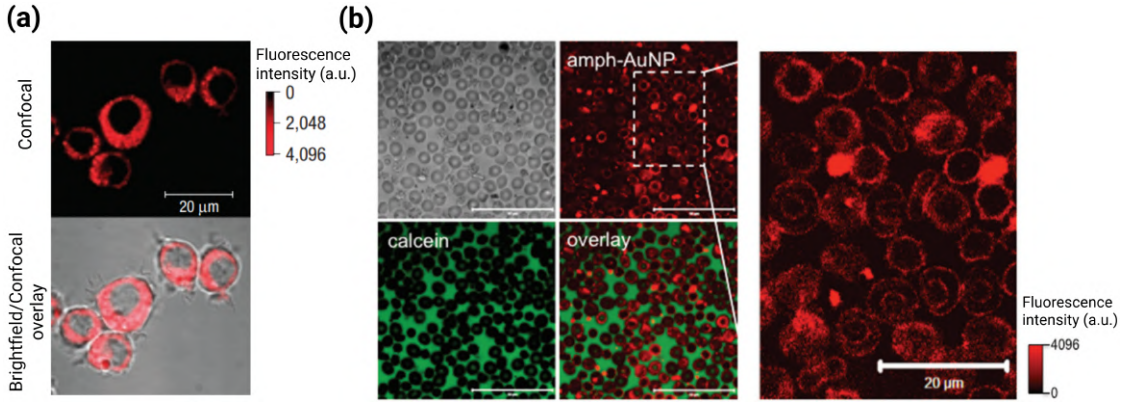

Figure 1.14 – ***Amphiphilic AuNP interactions with real cell membranes in vitro.*** **(a)** *Dendritic cells incubated with BODIPY-labeled (red) MUS:OT (2:1-4.5 nm) AuNPs show diffuse intracellular fluorescence. The NPs were incubated for 3 h in serum-free medium at 37 °C. Reprinted with permission from Verma et al [13]. Copyright (2008) Springer Nature.* **(b)** *Human erythrocytes incubated with BODIPY-labeled MUS:OT (2:1-2.3 nm) AuNPs show diffuse intracellular fluorescence, while no calcein (green) permeation is observed, indicating that the NP interaction does not disrupt the membrane. Cells were incubated with NPs at 0.28 mg mL^{-1} and calcein at 20 µg mL^{-1} for 3 h at 37 °C. Cells were imaged by confocal microscopy (scale bar in the left panel: 50 µm). Reprinted with permission from Atukorale et al [85]. Copyright (2015) RCS.*

Following the initial observations in cells, the mechanisms of interaction between AuNPs and membranes were systematically investigated in biomimetic lipid bilayers. Leakage fluorescence assays and QCM-D experiments demonstrated that both anionic and cationic NPs are able to penetrate neutral zwitterionic bilayers without disrupting the membrane [14]. Moreover, Canepa et al. [87] investigated NP interactions with complex membranes exhibiting phase separation, characterized by the coexistence of disordered regions and ordered domains, mimicking lipid rafts. In this work, atomic force spectroscopy was employed, which, like transmission electron microscopy (TEM), enables the study of NP-membrane interactions without the use of fluorescent probes, thus avoiding potential artifacts from dye-altered ligands behavior. The combination of experimental and computational approaches revealed the time-dependent aggregation of NPs, which perturbs phase separation by disrupting the ordered domains and progressively forming aggregates (Figure 1.15**a**).

Several studies have employed fluid-phase membranes, typically composed of zwitterionic phosphocholine vesicles [88, 89]. In Figure 1.15**b**, cryo-EM images show DOPC vesicles in the fluid phase interacting with MUS:OT NPs with core size in the range of $(2-3)$ nm. These NPs have a core diameter within the range predicted by previous simulations to be most

favorable for stable insertion into lipid bilayers [13, 83]. Notably, these cryo-EM images show the MUS:OT NPs of this size induce significant hemifusion between the fluid membranes of lipid vesicles.

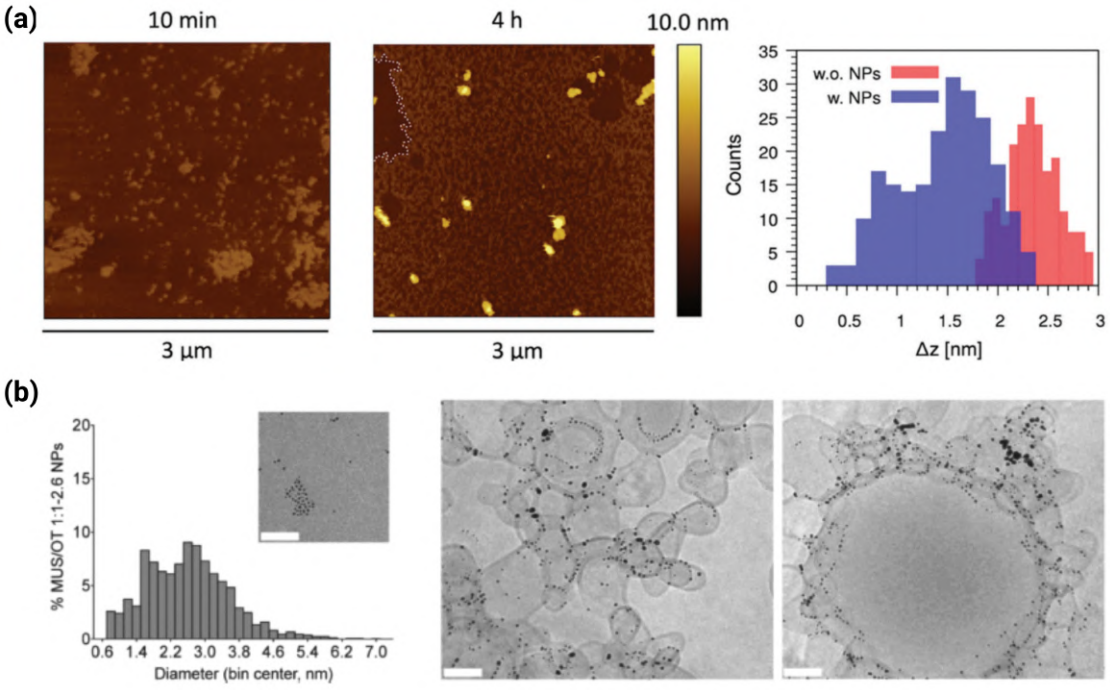

Figure 1.15 – ***Model membranes-amphiphilic AuNP interactions.*** **(a)** *AFM images of biomimetic membranes with raft-like domains incubated with NPs for* 10 min *and* 4 h*. The NPs progressively aggregate over time, leading to disruption of the raft-like domains, as observed in the image at* 4 h *and quantified in the corresponding histogram. Reprinted from Canepa et al. [87], licensed under CC BY-NC 3.0* **(b)** *Size distribution of MUS:OT (1:1-*2.6 nm*) AuNPs and cryo-EM images of DOPC vesicles incubated with the NPs (*0.28 mg mL^{-1} *for* 1 h *at* 25 °C*). Scale bars are* 50 nm*. Reprinted with permission from Atukorale et al [88]. Copyright (2018) American Chemical Society.*

Further studies demonstrated that full membrane fusion can be triggered between DOPC vesicles upon the addition of calcium ions [90]. Subsequently, Canepa et al. investigated the effect of cholesterol on these membranes. They found that, although cholesterol partially inhibits the uptake of NPs [91], it still promotes vesicle-vesicle fusion compared to vesicles without cholesterol [92].

Overall, these studies suggest that MUS:OT AuNPs are promising tools for investigating NP-membrane interactions, with several aspects of their membrane behavior still to be elucidated to develop novel biomedical applications. In the experiments presented in this thesis, AuNPs with different core sizes (< 6 nm) were employed, all functionalized with the same ligand molar ratio (2:1 MUS:OT). This ligand composition was selected because it ensures long-term colloidal stability in ultrapure water and saline buffered solutions at pH 7.4 and, as discussed above, it exhibits the most effective interaction with lipid membranes.

CHAPTER 2

Experimental techniques

This chapter introduces the main experimental techniques employed in this thesis to investigate NP-membrane interactions. These include fluorescence assays, QCM-D, optical microscopy, and SAXS. In addition, DLS and zeta potential measurements were performed to characterize both vesicles and NPs prior to each experiment. The chapter is organized into sections outlining the physical principles of each technique and the experimental setup.

2.1 Fluorescence assays

Fluorescence techniques are well-established and widely used to investigate model membrane systems, due to their sensitivity, temporal resolution, and compatibility with membrane components such as lipids and proteins [93, 94]. Since biological samples are generally transparent to visible light, these techniques are based on the specific labeling of membrane species with fluorescent molecules (or fluorophores). Upon interaction with external light, the fluorophores act as optical probes, whose fluorescence properties are highly sensitive to the surrounding molecular environment, enabling the detection and characterization of membrane structures and dynamics [95–98].

Fluorescence is a type of luminescence in which photons excite a molecule, promoting electronic transitions to higher energy states and resulting in photon emission at longer wavelengths. Upon excitation by an external light source, the fluorophore absorbs a photon with specific energy, promoting an electron from the ground electronic singlet state (S_0) to one of the vibrational levels of the excited singlet state (S_1). This electronically excited state is unstable, and the molecule rapidly undergoes non-radiative relaxation processes, such as vibrational relaxation and conformational rearrangements, which dissipate energy and bring the system to the lowest vibrational level of S_1. During the emission, the fluorophore returns

to one of the vibrational levels of the ground electronic state by emitting a photon with lower energy than the exciting photon, because part of the absorbed energy is lost through non-radiative pathways. This energy difference between excitation and emission is referred to as the Stokes shift [99]. The sequence of electronic transitions and relaxation processes involved in fluorescence is schematically represented by the Jablonski energy diagram, which illustrates the energy levels of the fluorescent molecule and the characteristic lifetime of each transition (Figure 2.1) [100].

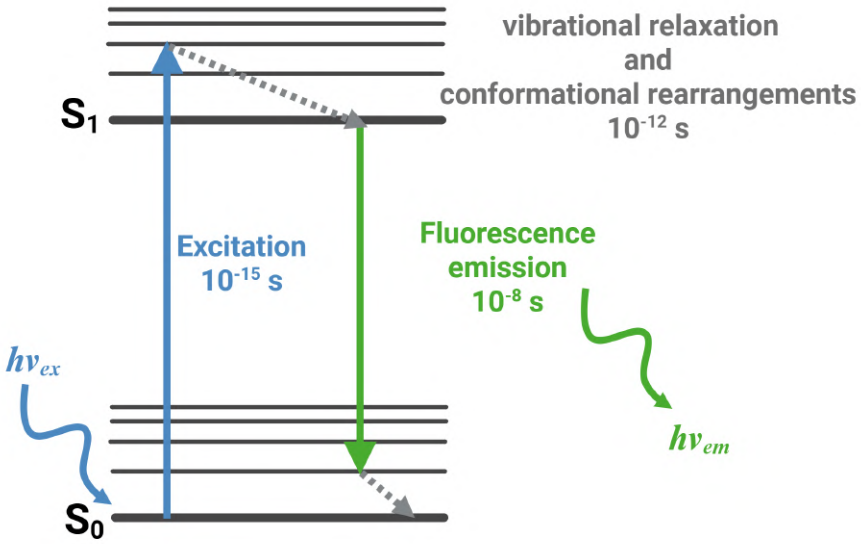

Figure 2.1 – *Schematic Jablonski diagram illustrating the electronic energy levels of a fluorescent molecule and the transitions occuring in the fluorescence process. Photon energies and transition lifetimes are shown. Created in Biorender.*

In this work, fluorescence was employed to elucidate different aspects of NP-membrane interactions. Fluorescence assays enabled the discrimination between vesicle lipid mixing, and content mixing processes, thereby providing complementary insights into the mechanisms underlying NP-induced membrane fusion (Chapter 3). Moreover, fluorescence microscopy was used to investigate NP interactions with GUVs (Chapter 4) whose size allows for direct optical visualization.

2.1.1 Lipid mixing

Lipid mixing is a fluorescence-based assay commonly used in membrane fusion studies. When two vesicles come into contact, their lipid bilayers merge and redistribute within a continuous membrane that envelopes the resulting fused vesicle. This assay serves to quantitively measure if the mixing of lipids from the original vesicles occurs [101, 102].

This fluorimetric method relies on Förster Resonance Energy Transfer (FRET), a photophysical mechanism in which an excited donor fluorophore transfers its energy, via a non-radiative dipole-dipole interaction, to an acceptor fluorophore (Figure 2.2**a**) [100]. The

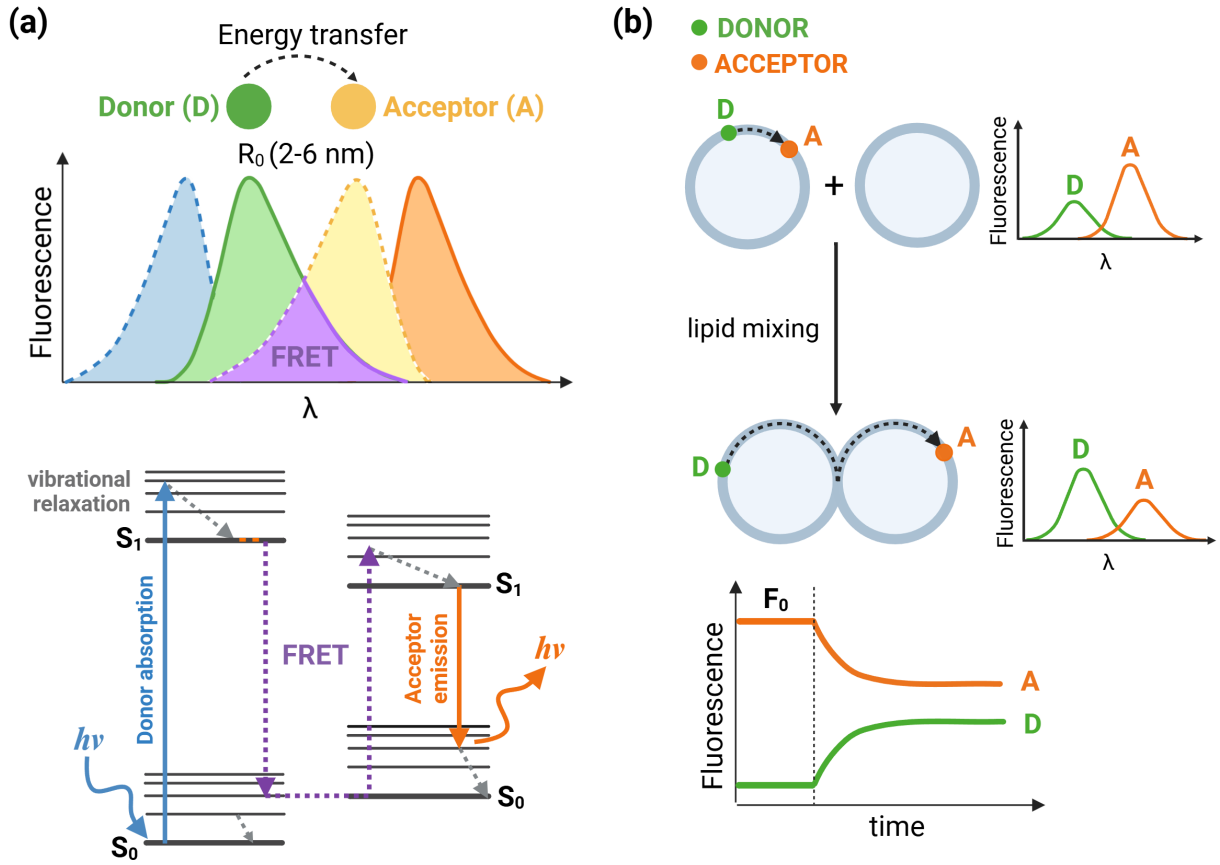

Figure 2.2 – ***Schematic illustration of FRET and its application to lipid mixing assay in model membrane systems.*** **(a)** *The resonance energy transfer mechanism occurs when the emission spectrum of a donor fluorophore (green) overlaps with the absorption spectrum of an acceptor fluorophore (yellow).* R_0 *is the Förster radius, which is the distance corresponding to an energy transfer efficiency of* 50 %*. The upper panel shows the donor and acceptor spectra, highlighting the spectral overlap (purple) between donor emission and acceptor absorption. The lower panel provides a representation of the same mechanism in the form of a Jablonski diagram, illustrating the energy transitions between electronic states and the photophysical processes involved, including donor excitation, vibrational relaxation, non-radiative energy transfer to the acceptor, and the subsequent fluorescence emission of the acceptor.* **(b)** *Application of FRET to monitor lipid mixing between vesicles labeled with donor and acceptor fluorophores and vesicles unlabeled. First, donor and acceptor fluorophores are in close proximity, resulting in donor quenching and enhanced acceptor emission. Upon lipid mixing, the donor-acceptor distance increases, leading to a reduction of FRET efficiency, which is reflected by an increase in donor fluorescence and a decrease in acceptor fluorescence over time. Created in Biorender.*

factors that regulate FRET process include the degree of spectral overlap between the donor emission and the acceptor excitation spectra, the relative orientation of their dipole moments, and most importantly, the distance between donor and acceptor. The FRET efficiency (E) depends on the inverse sixth power of the distance (r) between donor and acceptor, according to the relation:

$$E = \frac{1}{1 + \left(\frac{r}{R_0}\right)^6} \tag{2.1}$$

where R_0 is the Förster radius, which is the distance corresponding to an energy transfer efficiency of 50 %. R_0 is typically in the range $(2 - 6)$ nm. The distance dependence of energy transfer makes FRET a suitable tool for a wide range of biophysical applications, especially because the distances over which FRET occurs are comparable to the length scale of proteins or the thickness of biological membranes. The resonance energy transfer mechanism provides a convenient fluorescence signal to obtain quantitative information of lipid mixing during membrane fusion. This is achieved by incorporating donor- and acceptor-labeled lipid molecules into the bilayer at suitable concentration to optimize their distance [103].

In this thesis, I employed two commonly used lipid fluorophores, the donor *1,2-dioleoyl-sn-glycero-3-phosphoethanolamine-N-(7-nitro-2-1,3-benzoxadiazol-4-yl)*, or NBD-PE, and the acceptor *1,2-dioleoyl-sn-glycero-3-phosphoethanolamine-N-(lissamine rhodamine B sulfonyl)*, or Rhod-PE (see Figure A.2 for the chemical structures). In a typical assay, two vesicle populations are used: one labeled with both donor and acceptor fluorophores, and one unlabeled. Upon fusion between a labeled and an unlabeled vesicle, the labeled lipids redistribute in the newly merged membrane, thus increasing the average distance between donor and acceptor molecules. As a result, FRET efficiency decreases, leading to reduced acceptor emission and a corresponding increase in donor fluorescence emission (Figure 2.2**b**). However, it is important to note that this assay reports only on membrane mixing, not on the complete formation of a single, fully merged vesicle, in which the pore formation is completed allowing the mixing of the vesicles contents.

Lipid mixing assays were employed in the project described in Chapter 3, where all details of equipment specifications and analysis methods are reported.

2.1.2 Content mixing

Content mixing is an assay designed to monitor complete vesicle fusion, which is defined by the full mixing of the aqueous contents of the vesicle lumens [102]. This assay typically employs a fluorescent probe encapsulated at self-quenching concentration within the vesicle lumen. Although the probe can be efficiently excited by external light, its fluorescence emission is strongly suppressed due to the high local concentration. Self-quenching can occur through different mechanisms, such as collisions between two excited fluorophores that lead

to non-radiative relaxation to the ground state, or through the formation of non-excited dimers and energy transfer to these dimers. In a typical experimental setup, two vesicle populations are prepared: one without and one with the fluorescent probe. When fusion occurs, the mixing of vesicle contents leads to probe dilution and a corresponding increase in fluorescence. This signal variation provides a quantitative measure of complete fusion.

Sulforhodamine B (SRB) is a water-soluble dye that exhibits strong self-quenching at high concentrations (e.g, a probe concentration of 50 mM undergoes more than 95 % self-quenching) [90, 92, 104–106]. It was used as fluorescent probe for content mixing assays described in Chapter 3.

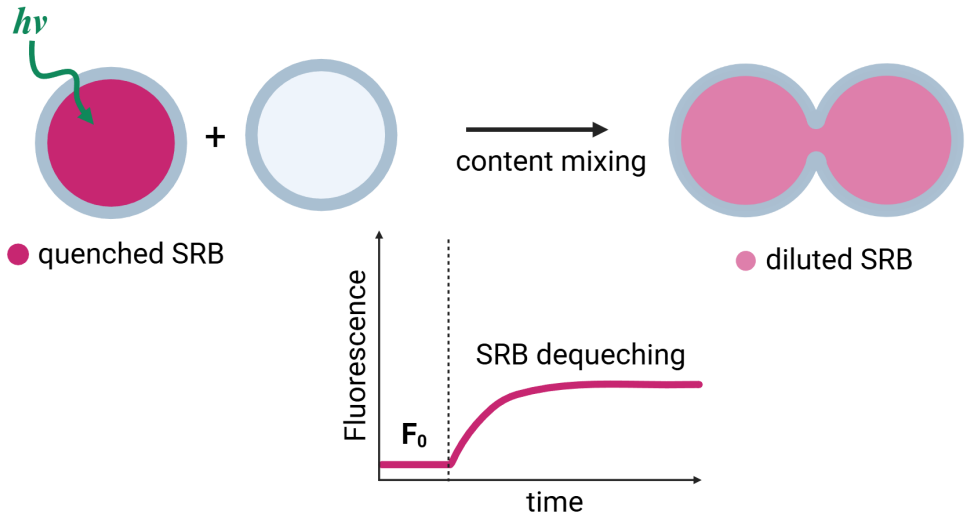

Figure 2.3 – ***Schematic representation of the content mixing assay.*** *A population of vesicles encapsulating sulforhodamine B (SRB) at self-quenching concentrations is excited at a specific wavelength, resulting in a low initial fluorescence signal (F_0). Upon fusion with unlabeled vesicles, mixing of the aqueous contents leads to dilution of SRB and fluorescence dequenching. The resulting time-dependent increase in fluorescence intensity provides a direct measure of vesicle content mixing. Created in Biorender.*

2.2 Quartz crystal microbalance

QCM is an ultrasensitive technique for detecting real-time mass changes on a sensor surface, with a sensitivity on the order of ng cm^{-2}. The sensor is a quartz crystal disk whose oscillation depends on the amount of material deposited on its surface, allowing frequency changes to be directly related to mass variations.

The quartz crystal disk is a piezoelectric material that is driven to oscillate at its resonant frequency f_0 by applying an alternating voltage to the electrodes deposited on the two faces of the disk. The oscillation properties of the sensor are determined by the cutting orientation of the original quartz block from which the disk is obtained. The first cutting orientation, introduced in 1921, was the X-cut, which had limited applications, since it exhibited a

strong temperature dependence [107]. In later years, a more suitable cutting orientation was developed, which is still employed to produce sensors and is known as the AT-cut (Figure 2.4**a**) [108]. The AT-cut disk offers several advantages, including opposite-surface oscillations that reduce net elastic deformation (Figure 2.4**b**), high temperature stability, minimal sensitivity to temperature gradients, and excellent mechanical properties with low energy dissipation, making it ideal for reliable measurements. In addition to the fundamental

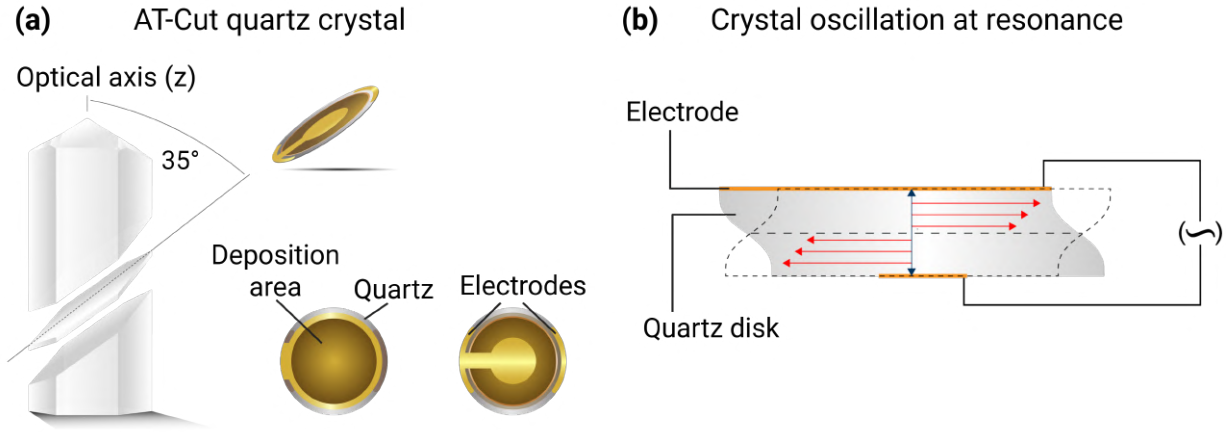

Figure 2.4 – ***Quartz crystal cut and oscillation.*** **(a)** *The AT-cut quartz crystal is oriented at approximately* 35° *with respect to the optical axis (z). The two opposite faces of the QCM sensor are shown: the electrodes, most commonly made of gold, and the active sensing surface, typically made of gold or silicon oxide, which is used for material deposition or surface functionalization.* **(b)** *Sketch of the oscillation mode of a quartz disk driven at its resonance frequency by an alternating driving voltage. For standard QCM devices operating at frequencies around* 5 MHz*, the quartz disk has a thickness of approximately* 300 µm*. Upon excitation, the faces of the disk oscillate in opposite directions, generating a stable mechanical resonance that is converted into an electrical signal due to the piezoelectric effect. Adapted from [109].*

resonant mode, QCM allows the measurement of higher harmonics (or overtones).

The relation between the fundamental frequency f_0 and the frequencies of the higher overtones f_n can be derived by solving the wave equation associated with the sensor oscillations and is given by:

$$f_n = \frac{n\nu}{2h_q} = nf_0 \tag{2.2}$$

where n is the overtone number ($n = 1$ corresponds to the fundamental harmonic; higher harmonics correspond only to antisymmetric (odd) vibrational modes, since these generate a measurable voltage between the electrodes), $\nu = \sqrt{\frac{\mu_q}{\rho_q}}$ is the shear wave velocity, h_q is the thickness of the quartz disk, μ_q is the shear modulus of quartz, ρ_q is the density of quartz, and f_0 is the fundamental resonant frequency. Equation (2.2) shows that the oscillation frequency depends on the thickness of the quartz crystal sensor [110]. From this relation, and by taking into account the variations in the disk thickness due to the addition of material on the sensor surface, it is possible to obtain the Sauerbrey equation [111], formulated in 1959, which expresses a linear relationship between the resonance frequency change of the

oscillating quartz crystal and the corresponding change in mass:

$$\Delta m = -C_f \frac{\Delta f}{n} \tag{2.3}$$

where $\Delta f/n$ is the observed frequency shift (Hz) normalized by the overtone number n, Δm is the change in mass per unit area of the piezoelectrically active surface, and C_f is the sensitivity factor related to the crystal properties [112]. The Sauerbrey equation is valid for rigid layers that behave as homogeneous and uniform extensions of the disk thickness and are strongly coupled to the sensor surface.

In many systems, including the one used in this thesis, QCM is integrated with a dissipation (D) monitoring system (QCM-D), which measures the energy dissipated during mass deposition and provides information on the viscoelastic properties of the sample. Initially, QCM was primarily employed as a mass sensor in air or vacuum. However, advances in electrical circuitry enabled its operation in liquid environments [113–115], making the technique particularly suitable for the investigation of biological samples. Many biological materials are soft and exhibit viscoelastic properties (e.g., proteins and lipid films). When subjected to external forces, such as the vibrations of the quartz crystal, which propagate through the material, they tend to deform undergoing bending, stretching, and compression. The mechanical energy associated with the crystal oscillation is partially converted into internal motion, resulting in friction that is dissipated as heat. This process leads to the damping of the crystal oscillation [116]. As illustrated in [109], viscoelastic layers behave like gelatin on a plate during plate oscillation, with the gelatin not following the motion of the plate in phase.

Dissipation is quantified through the decay-time of the oscillation. As described previously, the sensor is driven into oscillation by an alternating voltage precisely tuned to the resonant frequency of the quartz crystal, ensuring efficient excitation. To measure dissipation, the driving voltage is periodically switched off, more than 200 times per second (Figure 2.5**b**). The oscillation amplitude decreases over time, following an exponentially damped sinusoidal behavior described by:

$$A(t) = A_0 \, \mathrm{e}^{-t/\tau} \sin(2\pi f t + \phi) \tag{2.4}$$

where $A(t)$ is the oscillation amplitude, A_0 is the initial amplitude, t denotes time, τ is the decay-time constant, f is the resonant frequency, and ϕ is the phase. The decay-time constant τ is inversely related to the dissipation factor D, which quantifies the energy losses within the system:

$$D = \frac{1}{2\pi f \tau} \tag{2.5}$$

D is the dissipation factor, f is the resonant frequency, and τ is the decay-time constant. Therefore, QCM-D allows the simultaneous measurement not only of the mass adsorbed on the sensor surface (frequency shift Δf), but also of the mechanical properties of the sample

(changes in energy dissipation ΔD) (Figure 2.5**a**). In particular, ΔD provides information on the viscoelastic properties of the sample such as its stiffness or softness.

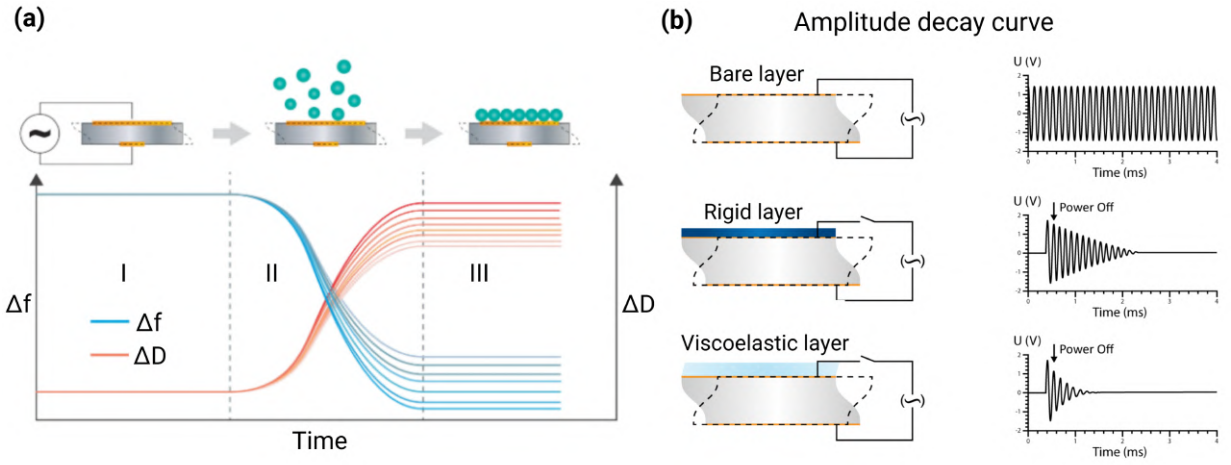

Figure 2.5 – **(a)** *Diagram showing the changes in resonance frequency and dissipation during the deposition of material on the sensor. The frequency decreases over time as material is deposited, untill reaching a stable plateau corresponding to full coverage of the active sensing surface. Simultaneously, the dissipation increases due to the presence of viscoelastic material on the sensor.* **(b)** *Illustration of different layer behaviors during dissipation measurement and the principle of dissipation monitoring. The sensor is excited with an alternating voltage multiple times per second, and the rate of energy damping reveals that viscoelastic materials dissipate energy and at a faster rate than rigid films. Adapted from [109, 117].*

In this thesis, QCM-D was employed to investigate the interaction between lipid vesicles and NPs in the context of membrane fusion studies, as discussed in Chapter 3. In particular, it enabled the quantification of NP uptake into the membrane and the measure of their ability to induce fusion between vesicles.

2.3 Optical microscopy

In this thesis, both label-free and fluorescent dye-based optical microscopy techniques were employed to study NPs interacting with GUVs (see Chapter 4). The size of these vesicles, $(10 - 100)\,\mu m$, is ideal for optical microscopy, allowing investigations at the level of single vesicle, an approach not feasible for smaller model vesicles.

2.3.1 Bright field and phase contrast methods

Bright-field and phase-contrast microscopy are label-free optical methods that are commonly used for the study of biological samples [118]. The main advantages of these techniques are their simplicity and low cost, which make them widely available in biology/biophysics laboratories. Unlike fluorescence microscopy (discussed in the following section), these techniques do not require the addition of external labels to the samples.

In a bright-field microscope, the specimen is placed between a light source and the objective lens. The illumination configuration, known as *dia-illumination* or *transmitted-light illumination*, allows light to pass through the specimen. A condenser lens focuses the light onto the sample, while the objective lens collects both the transmitted and diffracted light to form a magnified intermediate image, which is further enlarged by the eyepiece or recorded by a camera. In biological contexts, samples observed under visible light are often transparent in conventional bright-field microscopy. Since the human eye, as well as photosensors, are sensitive only to changes in light amplitude (i.e., intensity) or wavelength (i.e., color), unstained biological specimens exhibit low intrinsic contrast. From an optical point of view, specimens can be classified into two main categories: *amplitude objects* and *phase objects*. Amplitude objects modify both the amplitude and phase of the transmitted light, whereas phase objects primarily induce phase shifts without significantly affecting the light intensity. For this reason, staining is commonly used to introduce amplitude differences, resulting in changes in light intensity and color after transmission through the specimen.

However, several label-free contrast methods exist, among which the most widely used in biological applications are phase-contrast and differential interference contrast (DIC) microscopy. In this thesis, I focus exclusively on phase-contrast microscopy, which is the technique employed in the experiments presented in Chapter 4. The main goal of optical contrast techniques is to convert phase variations into measurable intensity differences, which can be detected by the eye or by imaging sensors. Optical contrast techniques are based on the selective manipulation of the background (undeviated) light and the object-diffracted light, in order to generate intensity variations in the image plane. From a physical point of view, this represents a diffraction problem based on the formation of constructive and destructive interference. Phase shifts introduced by the specimen are transformed into measurable intensity signals through the controlled interference between the background (undeviated) wave and the object-diffracted waves. Phase contrast microscopy was developed in the 1930s by the Dutch physicist Frits Zernike and became a standard imaging technique by 1942. For this work, Zernike received the Nobel Prize in Physics in 1953 [119]. Phase shifts result from variations in the *optical path length* of light traveling through specimen regions with distinct refractive indices and thicknesses. The optical path length (OPL) is given by

$$\mathrm{OPL} = nd \tag{2.6}$$

where n is the refractive index and d is the physical thickness of the medium. As a consequence, light propagating through the specimen is slowed down and undergoes a corresponding phase shift. The purpose is to bring the light waves into a defined phase relation in order to generate constructive or destructive interference. According to the principle of superposition, when two waves interfere, the amplitude of the resulting light wave is equal to the vector sum of the amplitudes of the individual interfering waves. This results in constructive interference

when the waves are in phase, and destructive interference when they are out of phase. In order to obtain these effect, a phase contrast microscope has to be designed as shown in Figure 2.6**a**, whose fundamental elements are a circular annulus and a phase plate.

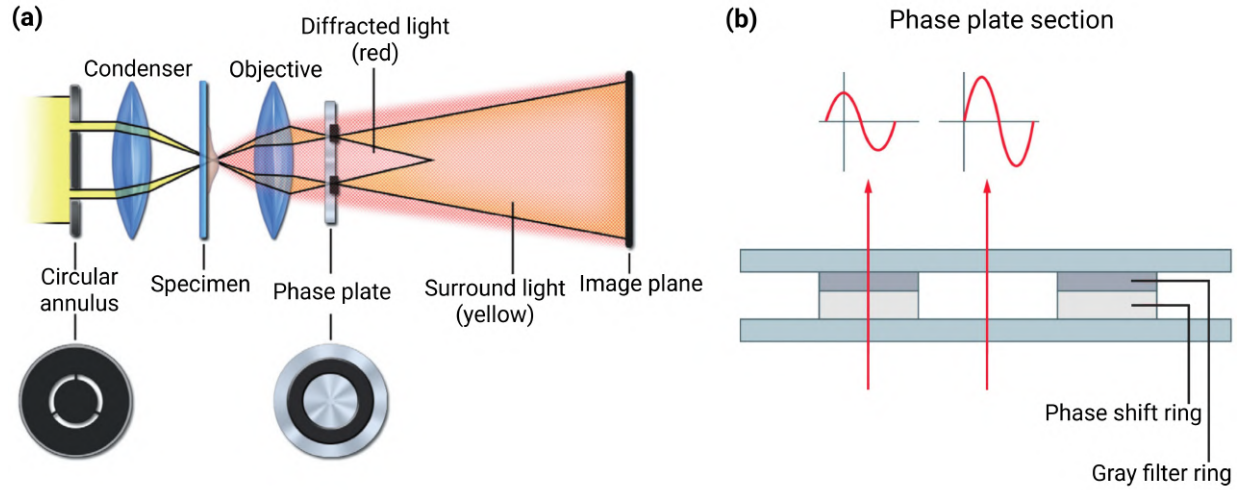

Figure 2.6 – ***Phase contrast microscope.*** **(a)** *Scheme showing the main optical elements of a phase contrast microscope. The circular annulus and the phase plate are the key components of this technique: the annulus modulates the incident light beam, while the phase plate introduces a phase shift between the diffracted and undiffracted light. Reprinted with permission from [118]. Copyright (2013) Wiley-Blackwell.* **(b)** *Section of a phase plate highlighting its two main regions. The central red arrow represents the sample-diffracted light beam, while the red arrow on the left represents undeviated light, passing through the phase shift ring and the grey filter ring. For further details, see the text. Adapted from [120].*

The circular annulus placed in the front aperture of the condenser produces a ring-shaped illumination, which passes through the condenser and is focused onto the specimen. Light passing through the specimen is partially diffracted due to variations in refractive index and optical path length across different regions of the sample, while part of the light remains undeviated. The diffracted light undergoes a phase retardation of $\sim \lambda/4$[1], whereas the undeviated light initially remains unshifted. At this point, all light passes through the objective. In order to create an additional phase shift in the undeviated light and enable interference, a spatial separation between diffracted and undeviated light is required. All non-diffracted rays share the same angle determined by the circular annulus, and the objective focuses them onto the same circle in its focal plane, which coincides with the phase plate annulus. Diffracted light, in contrast, has a continuous angular distribution; the objective spreads it over the entire rear focal plane, with only a small fraction falling on the phase plate annulus. The phase plate performs two actions. First, it advances (positive phase contrast, resulting in destructive interference) or retards (negative phase contrast, resulting in

[1]This $\lambda/4$ phase shift in the diffracted light arises naturally from scattering and diffraction processes within the sample (see [121]). For typical biological specimens, with usual thickness and refractive index, any additional phase shifts are generally small and can be considered negligible.

constructive interference) the phase of the undeviated wave by $\lambda/4$ using the *phase shift ring* (Figure 2.6**b**). Second, it attenuates the intensity of the undeviated light by approximately 70 % using the *gray filter ring*. This combination enhances image contrast and enables phase variations introduced by the specimen to be transformed into detectable intensity differences. For the correct functioning of the phase contrast mechanism, the circular annulus and the phase plate must have exactly the same diameter and be perfectly aligned.

Furthermore, optical artifacts are present in every phase contrast image and are natural consequences of the optical system, i.e., *halos* and *shade-off* (Figure 2.7). Halos appear at the edges of objects, while shade-off occurs in the central regions. Halos exhibit contrast opposite to that of the phase object and are typical for large objects such as cells, nuclei, and GUVs. Halos arise because the separation between direct and diffracted light in the focal plane is not perfect, and some diffracted light passes through the phase plate annulus. Additionally, the phase plate annulus is wider than the zero-order light ring for optical design reasons (approximately 25 % wider), causing these components not to interfere as intended. On the other hand, shade-off is a gradual loss of contrast towards the center of an extended, uniform object, making the central region appear similar to the background. It is also typical of large objects and arises because extended objects diffract less in their central regions and more at their edges.

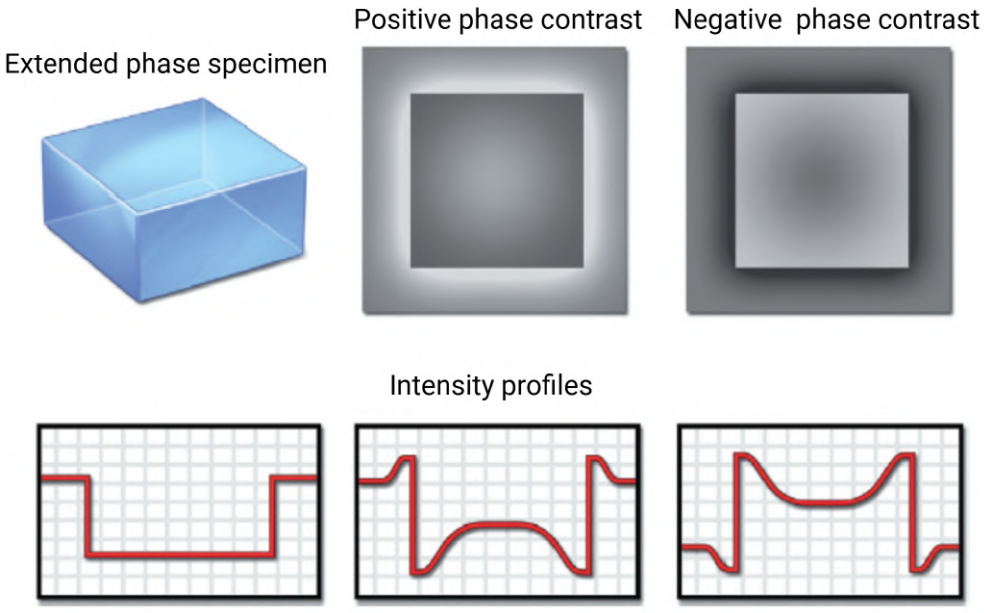

Figure 2.7 – ***Illustration of halo and shade-off effects in phase contrast microscopy.*** *In positive phase contrast, the specimen causes a phase delay: a bright halo appears around dark edges, and the interior shows gradual brightening (shade-off). In negative phase contrast, the specimen advances the phase: a dark halo forms around bright edges, and the interior gradually darkens. Reprinted with permission from [118]. Copyright (2013) Wiley-Blackwell.*

2.3.2 Confocal laser scanning fluorescence microscopy

Phase contrast microscopy is an effective method for studying properties of biological objects without using any dyes. However, resolving finer structural details, (e.g., the presence of tubes or buds in GUVs) remains challenging with this technique. To overcome this limitation, optical microscopy based on fluorescence as a contrast mechanism can be employed to gain better resolution for observing these structural details.

In a traditional wide-field epifluorescence optical microscope, the sample is illuminated simultaneously across the entire field of view, and the detection system collects fluorescent radiation emitted not only from the focal plane but also from out-of-focus planes. This results in a reduction of image contrast and limits the effective spatial resolution of the system. From a theoretical point of view, in 1873 Ernst Abbe demonstrated that the factor limiting the resolution of an optical microscope is the diffraction of light [122]. The parameters that determine the resolution are the aperture angle α of the objective lens and the refractive index n of the surrounding medium. From these quantities, the numerical aperture (NA) can be defined as

$$\mathrm{NA} = n \sin \alpha \tag{2.7}$$

The minimum resolvable distance between two points in the X-Y plane is then given by

$$\Delta x = \frac{\lambda}{2\,\mathrm{NA}} \tag{2.8}$$

where λ is the wavelength of the light used. In wide-field imaging the resolution is typically in the range $(200 - 250)$ nm.

However, in wide-field microscopy the resolution is often limited not by diffraction criteria, but by the low image contrast. Since the excitation is not confined to the focal plane, signals originating from out-of-focus planes contribute to a diffuse background. Moreover, in biological samples, light-scattering processes can redirect photons emitted from out-of-focus regions toward the detection plane, increasing background noise. As a consequence, image contrast, rather than diffraction, often represents the dominant limiting factor. Confocal microscopy overcomes these limitations inherent to wide-field imaging. The first confocal microscope was developed around 1950 by Marvin Minsky. However, this technology achieved widespread development in the 1980s mostly due to advances in optical instrumentation and the invention of laser [123, 124].

The key elements that characterize a confocal microscope are the pinhole and point-by-point scanning of the sample. Figure 2.8 shows a schematic representation of the operating principle of a confocal microscope.

Confocal microscopy is based on an *epi-illumination* configuration, in which the light source and the detector are located on the same side of the sample and share the same objective, which performs the dual function of condenser and imaging objective [118, 125,

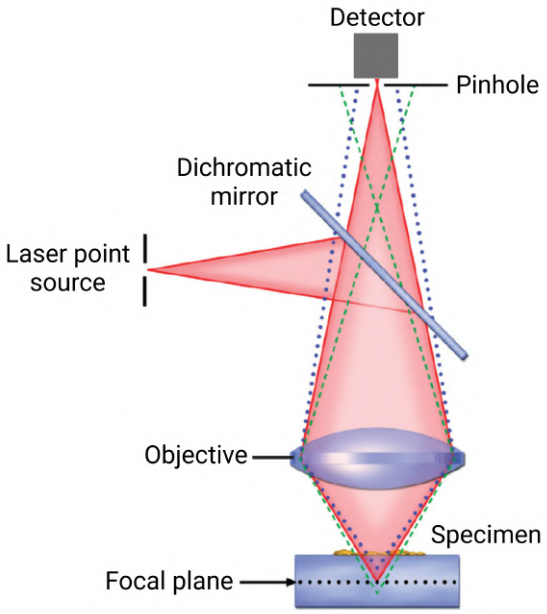

Figure 2.8 – ***Scheme showing the main optical elements of a confocal microscope.*** *The pinhole is the key optical component that allows imaging from a single focal plane (red beam) while preventing light from out-of-focus planes (dashed green lines for a plane below focus and blue lines for a plane above focus) from reaching the detector. For further details, see the text. Reprinted with permission from [118]. Copyright (2013) Wiley-Blackwell.*

126]. Excitation and detection of fluorescence are carried out using the same optical filters employed in wide-field fluorescence microscopy. A laser beam is expanded to illuminate the whole back aperture of the objective, generating a focused spot that is scanned point by point across the sample following a raster trajectory (Figure 2.9). This process, known as point scanning, enables localized illumination of the sample. The crucial optical element of the confocal system is the pinhole, positioned in a plane conjugate to the focal plane of the sample. The pinhole allows fluorescence emitted from the in-focus point to pass through, while largely blocking signals originating from out-of-focus planes. The fluorescence emitted from each excited point is collected by the same objective, directed back along the original optical path, and focused onto the pinhole before reaching the detector, such as a photomultiplier tube. The detector converts the optical signal into an electrical signal, which is digitized and processed by the computer to reconstruct the final image. The confocal image is therefore built sequentially over time and does not exist as a real image that can be directly observed through the microscope eyepiece. A system with this architecture is called a laser scanning confocal microscope (CLSM) and is particularly suited for high-contrast imaging and optical sectioning of thick samples [126]. Figure 2.9 shows the system that enables scanning of the sample. The mechanism is based on the movement of two galvanometer-driven mirrors that oscillate to the X and Y movement of the laser, respectively. In confocal microscopy, the resolution can be improved to approximately $(180 - 220)$ nm.

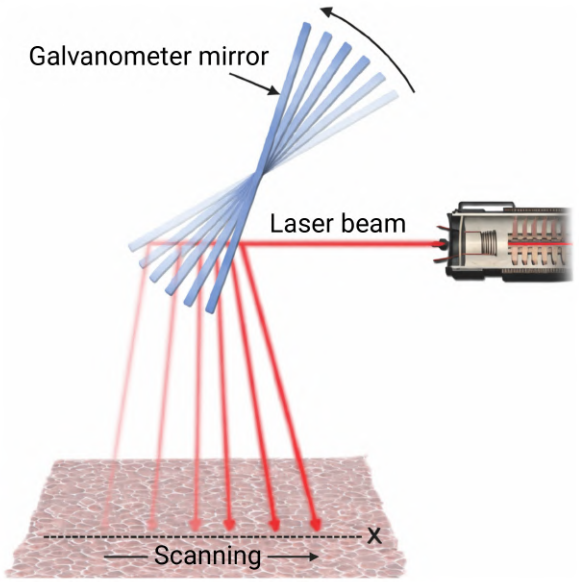

Figure 2.9 – ***Representative sketch of the scanning mechanism on the x-axis.*** *The scanning process distinguishes the confocal microscope from wide-field microscopy and enables improved image resolution by acquiring information from small regions at a time, effectively acquiring the image point by point. Reprinted with permission from [118]. Copyright (2013) Wiley-Blackwell.*

2.4 Small-angle X-ray scattering

SAXS is a non-destructive analytical technique designed to determine the average structure of particle systems in terms of their size and shape. The material can be either solid or liquid and can contain domains (i.e, particles) with different compositions or densities, including solid, liquid, or gaseous phases. The application of SAXS spans numerous fields, from fundamental research to quality control. These applications include the study of polymers, biological materials [127], colloids, metals [128], pharmaceutical products [129], and food materials [130].

The standard operating principle involves propagating X-rays through the sample in transmission mode. Each particle illuminated by the beam produces a scattering signal, and the resulting intensity measurement reflects the average structure of all particles illuminated within the sample [131]. In Figure 2.10, a schematic representation of the SAXS experimental setup is shown.

From a physical perspective, X-rays are electromagnetic waves with wavelengths shorter than approximately 0.3 nm. They are characterized by alternating electric and magnetic fields that are perpendicular to each other and to the direction of propagation. When X-rays irradiate a sample, photons interact with electrons and provide information about fluctuations in the electron density of the samples. The spatial distribution of electrons within the sample is described by the electron density profile, $\rho(\vec{r})$, which represents the local electron density as a function of position.

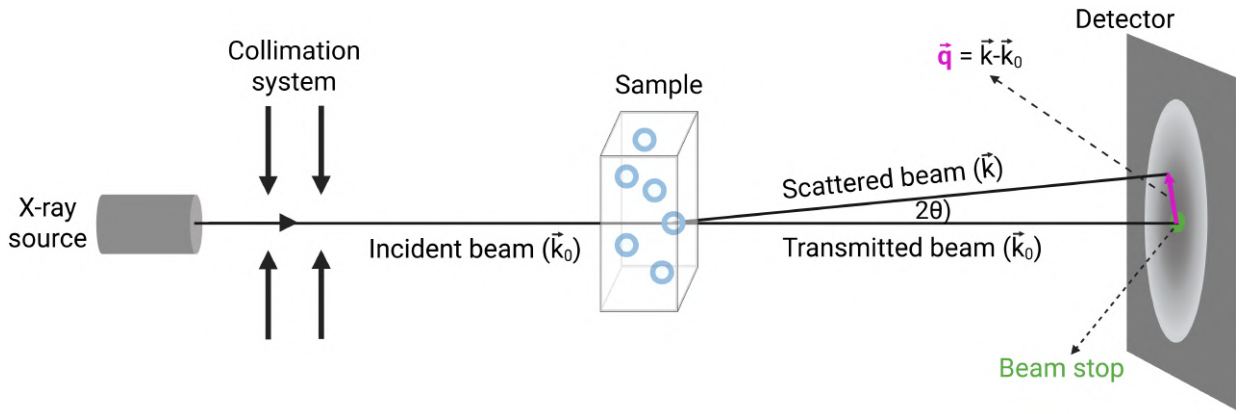

Figure 2.10 – ***Setup of a SAXS experiment in transmission geometry.*** *The X-ray beam emitted from the source passes through a collimation system and illuminates the sample. Part of the beam is transmitted along the original direction ($\vec{k}_0$ is the incident wave vector), while another part is scattered ($\vec{k}$ is the scattered wave vector). The detector measures the intensity of the scattered beam at the angle 2θ, while the direct beam is blocked by a beam stop. The scattering vector is defined as $\vec{q} = \vec{k} - \vec{k}_0$. Created in Biorender.*

The relevant quantity is the electron density contrast between the scattering particles and the surrounding medium, defined as

$$\Delta\rho(\vec{r}) = \rho(\vec{r}) - \rho_s \tag{2.9}$$

where ρ_s is the electron density of the solvent or matrix. Individual atoms scatter radiation in all directions through a process known as *Thomson scattering*, producing an almost constant background at small scattering angles. In contrast, clusters of atoms (the particles) generate an additional contribution known as *excess scattering*, which arises from their larger size and their electron density contrast relative to the surrounding medium. To obtain meaningful structural information such as particle size, shape, or specific surface area, the scattering profile of the medium must be acquired and mathematically subtracted from the scattering profile of the particle solution.

X-ray scattering gives rise to interference phenomena, which can be constructive or destructive depending on the observation angle 2θ, the relative orientation of the atoms, and the distances between them. The resulting interference patterns on the detector reflect the point-to-point variations in intensity across the detection plane. The intensity is the only quantity directly measurable by the detector, as the phase information of the scattered waves is lost during detection. It corresponds to the squared modulus of the scattering amplitude, which is defined as

$$I(\vec{q}) = \left\langle |A(\vec{q})|^2 \right\rangle_\Omega \tag{2.10}$$

where the angular brackets denote averaging over all orientations in isotropic systems. The

scattering amplitude is given by the Fourier transform of the electron density contrast:

$$A(\vec{q}) = \int_V \Delta\rho(\vec{r})\ \mathrm{e}^{\mathrm{i}\vec{q}\cdot\vec{r}}\ \mathrm{d}\vec{r} \tag{2.11}$$

Consequently, the intensity is described as a function of the scattering vector $\vec{q}$ [132, 133], whose magnitude is given by

$$q = |\vec{q}| = \frac{4\pi}{\lambda}\sin\theta \tag{2.12}$$

where λ is the wavelength of the incident radiation, and θ is half of the scattering angle. The scattering vector $\vec{q}$, also referred to as the *momentum transfer*, has dimensions of inverse length (e.g., nm^{-1}). Small-angle scattering experiments are designed to measure $I(q)$ at very small values of $|\vec{q}|$, corresponding to long-range structural information on the nanometer scale. In general, SAXS can resolve structures ranging from approximately 1 nm to 300 nm, although this range may vary depending on the instrument. Additionally, the accessible range can be extended toward smaller scattering angles using USAXS (Ultra-Small-Angle X-Ray Scattering), or toward larger scattering angles using WAXS (Wide-Angle X-Ray Scattering), also known as X-ray Diffraction (XRD).

A crucial requirement for SAXS measurements is the presence of sufficient contrast. In particular, the particles must have an electron density different from that of the surrounding matrix (such as the solvent or host material) in order to be detected. Materials containing elements with higher atomic numbers generally provide stronger contrast and therefore lower detection limits. Conversely, matrices composed of heavy elements must be treated with care due to their strong X-ray absorption. When performing SAXS measurements, absorption effects must also be taken into account, as they can be non-negligible for some samples. In this process, the energy of an incident photon can eject an electron from an atom, leaving it in an excited state. The atom subsequently relaxes back to a stable configuration by rearranging its electrons, emitting radiation with wavelengths different from that of the incident beam. Therefore, in order to obtain high-quality SAXS data, X-ray absorption should be minimized.

2.5 Dynamic light scattering and zeta potential

DLS and zeta potential measurements were performed in this work to characterize the size, surface charge, and colloidal stability of both NPs and vesicles. DLS is a conventional bulk technique used to determine the size of particles dispersed in solution, ranging from sub-nanometer to micrometer scales. It employs a laser to illuminate the sample and detects time dependent-fluctuations in the intensity of the scattered light, from which information about sample-averaged size can be obtained. Zeta potential measurements are derived from electrophoretic mobility under an applied electric field and allow the determination of the electrostatic potential in the vicinity of the surface of dispersed colloidal particles.

2.5.1 DLS measurements

A particle in solution undergoes a random and continuous motion in all directions, which is uncorrelated with the motion of the other particles. This phenomenon, known as *Brownian motion*, arises from random collisions between the particle and the surrounding solvent molecules, which are smaller in size and driven by thermal agitation [134]. By solving the equation of motion for a particle of mass m immersed in a homogeneous fluid, the mean squared displacement of the particle in three dimensions and in the long-time approximation is given by

$$\langle r^2(t) \rangle \simeq \frac{6 k_\mathrm{B} T}{m\gamma}\, t \tag{2.13}$$

where k_B is the Boltzmann constant, T is the temperature, and γ is the friction coefficient per unit mass (which has the dimensions of a frequency). From this relation, the Einstein's relation, which defines the diffusion coefficient D, can be obtained:

$$D = \frac{k_\mathrm{B} T}{m\gamma} \tag{2.14}$$

The Einstein's relation can be applied to the diffusive motion of a spherical particle immersed in a viscous fluid under laminar flow conditions, leading to the Stokes-Einstein's equation:

$$D = \frac{k_\mathrm{B} T}{3\pi\eta D_H} \tag{2.15}$$

η is the solvent viscosity and D_H is the particle hydrodynamic diameter.

In a DLS experiment, the sample is illuminated with a laser beam, which interacts with the particles dispersed in solution [135, 136]. The light scattered by the particles is collected at fixed angles, typically at 173° (backscattering configuration) or at 90° (Figure 2.11). As the particles undergo Brownian motion, their relative positions continuously change over time, resulting in fluctuations in the intensity of the scattered light. These fluctuations produce an interference dynamic pattern consisting of alternating regions of constructive and destructive interference. Regions where the scattered waves add coherently generate intensity maxima, while regions where they combine out of phase result in a reduction or cancellation of the detected intensity. To characterize the fluctuations, the first quantity that is considered is the electric field autocorrelation function:

$$G_1(\tau) = \langle E_S^*(t)\, E_S(t+\tau) \rangle = \langle E_S^*(0)\, E_S(\tau) \rangle \tag{2.16}$$

Since the measured quantity is the light intensity rather than the electric field, it is convenient to define the second-order autocorrelation function in terms of the intensity

$$G_2(\tau) = \langle I_S(0)\, I_S(\tau) \rangle \tag{2.17}$$

A simple relation exists between these two correlation functions, known as Siegert's relation [137], which is valid for a Gaussian electric field

$$G_2(\tau) = \langle I_S \rangle^2 + \beta \, |G_1(\tau)|^2 \tag{2.18}$$

where β is an instrumental factor that depends on the geometry of the detection optics and the alignment of the setup.

It is common to use the reduced first and second order correlation functions, defined as

$$g_1(\tau) = \frac{G_1(\tau)}{\langle I_S \rangle} \quad \text{and} \quad g_2(\tau) = \frac{G_2(\tau)}{\langle I_S \rangle^2} \tag{2.19}$$

Subsequentely,

$$g_2(\tau) = 1 + \beta |g_1(\tau)|^2 \tag{2.20}$$

For a monodisperse particle population:

$$|g_1(\tau)|^2 = \mathrm{e}^{-2\Gamma\tau} \tag{2.21}$$

where $\Gamma = D|\mathbf{K}|^2$, and $\mathbf{K}$ is the scattering vector. This leads to

$$g_2(\tau) = 1 + \beta \, \mathrm{e}^{-2\Gamma\tau} \tag{2.22}$$

The intensity correlation function contains all of the information regarding the diffusion of particles within the sample. By analyzing this function, the diffusion coefficient D can be determined, and consequently the particle diameter can be calculated (Figure 2.11).

However, samples are often not monodisperse and exhibit a continuous distribution of particle sizes with a certain degree of polydispersity. The electric field correlation function can be expressed as an integral over the probability density of decay rates Γ, meaning that the total signal is the sum of contributions from all particles, with each contribution weighted by the particle scattering intensity, which depends on the particle size and its optical properties:

$$g_1(\tau) = \int G(\Gamma) \, \mathrm{e}^{-\Gamma\tau} \, \mathrm{d}\Gamma \tag{2.23}$$

Obtaining information about particle sizes requires inverting this integral, but the inversion process tends to smooth the data and amplify the experimental noise, thus small variations in the measured data can lead to large differences in the results. To address this issue, the cumulant analysis is commonly used. This approach approximates the correlation function as a sum of exponentials:

$$g_1(\tau) = \mathrm{e}^{\left(-\bar{\Gamma}\tau - \frac{\mu_2}{2!}\tau^2 + \frac{\mu_3}{3!}\tau^3 - \cdots\right)} \tag{2.24}$$

where $\bar{\Gamma} = \int \Gamma \, G(\Gamma) \, \mathrm{d}\Gamma$ is the average decay rate. The second cumulant μ_2 corresponds to

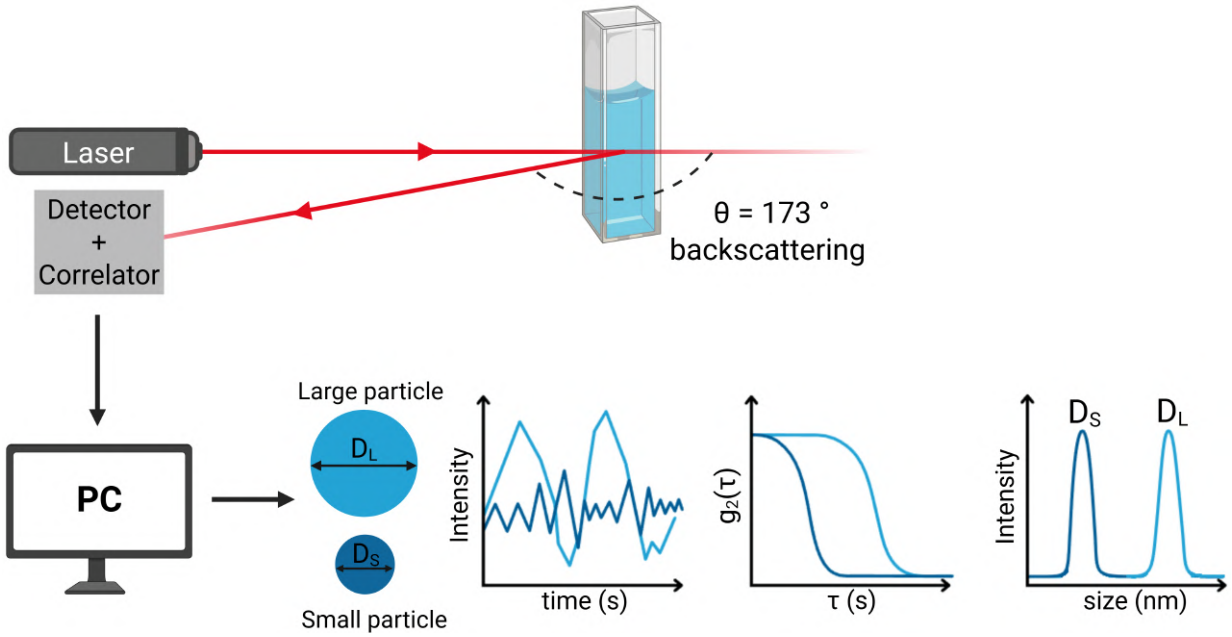

Figure 2.11 – ***Schematic representation of the DLS principle.*** *A laser beam illuminates the sample, and the light is collected by a detector. The backscattering detection mode ($\theta = 173°$) is used to maximize the detected signal and minimize multiple scattering effects in concentrated or opaque samples. Temporal fluctuations of the scattered intensity, caused by the Brownian motion of the particles, are analyzed through the intensity autocorrelation function $g_2(\tau)$. Large particles produce slowly varying intensity fluctuations, whereas small particles generate faster fluctuations. The decay time of the autocorrelation function is used to determine the diffusion coefficient and, consequently, the particle size distribution. Created in Biorender.*

the variance of the decay rates and provides a measure of the sample polydispersity:

$$\mu_2 = \langle(\Gamma - \bar{\Gamma})^2\rangle = \int (\Gamma - \bar{\Gamma})^2 \, G(\Gamma) \, \mathrm{d}\Gamma \tag{2.25}$$

The third cumulant μ_3 describes the skewness of the distribution. Higher-order cumulants can be included for highly polydisperse systems, but usually only the first few are used. In addition to intensity-weighted distributions, DLS can also provide volume- and number-weighted size distributions, which can be reported for data interpretation, as in this thesis. These distributions are not directly measured, but are derived from the intensity distribution using model-dependent transformations based on Mie scattering theory [138], which requires knowledge of the optical properties of the system, including the refractive index and absorption of both particles and solvent [139].

2.5.2 Zeta potential measurements

Zeta potential measurements are used to assess the colloidal stability of particles dispersed in solution [135, 140, 141]. If particles in solution are characterized by a high positive or high negative zeta potential, electrostatic repulsion dominates and prevents particle aggregation.

When dispersed in solution, a particle with a charged surface influences the distribution of ions in the surrounding interfacial region, leading to an increased concentration of counter-ions (ions with charge opposite to that of the particle) close to its surface. Figure 2.12**a** schematically shows the different charge layers that form around a negatively charged colloidal particle. A negatively charged particle surface was taken as a reference, consistent with the particles studied in this thesis. The first layer, consisting of ions strongly bound to the particle surface, is known as the *Stern layer*. Further from the surface, a region of more loosely associated ions is present, referred to as the diffuse layer. Together, these two regions constitute the electrical double layer, which forms a stable entity with the particle and moves together with it when the particle is in motion. Beyond a certain boundary, known as the *slipping plane*, the ions no longer move with the particle. The zeta potential is defined as the electrostatic potential at the slipping plane.

Zeta potential measurements are commonly performed using electrophoresis, a technique based on the motion of dispersed particles relative to the suspending liquid under the application of an external electric field. When a constant electric field is applied, particles migrate toward the electrode of opposite polarity (Figure 2.12**b**).

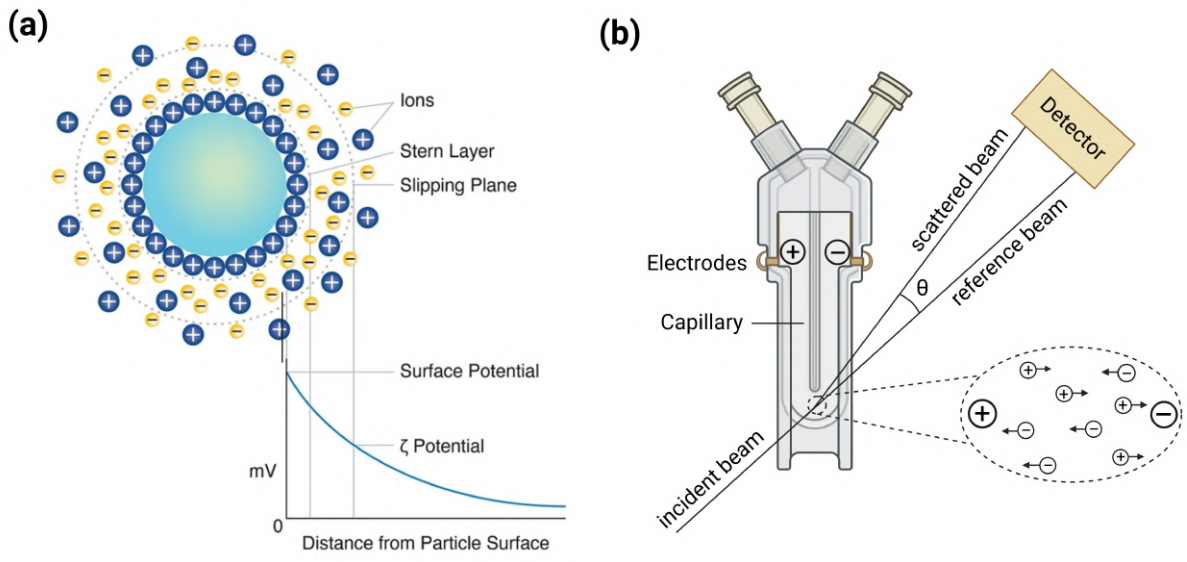

Figure 2.12 – ***Schematic representation of the zeta potential and its measurement principle.*** **(a)** *Ions present in solution form distinct layers around a charged particle according to their interaction with the particle. Depending on how strongly these ions are bound, different planes can be defined. The zeta potential is calculated at the slipping plane, which is the most external layer of ions that moves together with the particle during its motion.* **(b)** *Inside the capillary of a zeta potential cuvette, charged particles move toward electrodes of opposite sign. An incident beam illuminates the moving particles, and the scattered light is detected together with a reference beam. Using the LDV method, the electrophoretic mobility of the particles is determined, allowing the calculation of the zeta potential as shown by Equation (2.27). Created in Biorender.*

During this motion, particles experience a viscous drag force exerted by the surrounding

fluid. After a short transient time, the electric driving force and the viscous drag force, resulting in a constant particle velocity. From the measurement of this velocity, the electrophoretic mobility U_E can be calculated as

$$U_E = \frac{v}{E} \tag{2.26}$$

where v is the particle velocity and E is the applied electric field.

The relation between electrophoretic mobility and zeta potential is given by the Henry's equation:

$$U_E = \frac{2\,\varepsilon\,\zeta\,f(\kappa a)}{3\,\eta} \tag{2.27}$$

where ζ is the zeta potential, ε is the dielectric constant η is the viscosity, and $f(\kappa a)$ is Henry's function, which depends on the ratio between the particle radius a and the reciprocal of the Debye length κ. For large particles or concentrated solutions, where the thickness of the electric double layer is small compared to the particle radius ($\kappa a \gg 1$), the Smoluchowski limit is valid, and $f(\kappa a) = 1.5$. In contrast, for small particles or dilute solutions, where the double layer is thicker than the particle radius ($\kappa a \ll 1$), the Hückel limit applies, with $f(\kappa a) = 1.0$.

The electrophoretic mobility is experimentally determined by Laser Doppler Velocimetry (LDV) [142]. A laser beam is directed onto the sample and the light scattered by the moving particles is collected at a fixed angle and recombined with a reference beam, producing an interference signal. Due to the *Doppler effect*, when a light source or scatterer moves relative to the detector, the frequency of the detected light is shifted. The frequency of the resulting intensity fluctuations is proportional to the particle velocity. This technique provides the value of the zeta potential. To determine its sign, an optical modulator is introduced into the system. The modulator consists of an oscillating mirror operating at a known frequency, which induces a frequency shift in the reference beam. By comparing the frequency of the scattered light with that of the reference beam, it is possible to determine whether the scattered light has undergone an increase or a decrease in frequency. This information allows the direction of particle motion to be established, and consequently the sign of the particle charge.

Zeta potential values between -30 mV and 30 mV are generally associated with limited colloidal stability, as electrostatic repulsive forces may be insufficient to prevent particle aggregation over time. In contrast, zeta potential values higher than 30 mV or lower than -30 mV indicate stable systems, due to stronger electrostatic repulsion between particles.

CHAPTER 3

NP-mediated membrane fusion

The results of the investigation of NP-mediated lipid membrane fusion are presented in this chapter. The project investigates the fusogenic role of AuNPs in promoting the fusion of lipid vesicles, with particular attention to the role of NP size and membrane curvature in regulating the efficacy of the fusion process.

I carried out fluorescence assay experiments at the University of Genoa (UniGe) and QCM-D measurements at the Italian Institute of Technology (IIT). The latter measurements were performed in collaboration with Dr. Silvia Dante (Materials Characterization Facility, IIT, Morego, Genoa). In addition, this study was conducted in collaboration with the computational group of Prof. Giulia Rossi (UniGe), who provided a molecular-level interpretation of the experimental results through molecular dynamics simulations. This chapter reports all the experimental results and the main computational findings, which are presented in Leonardini et al. [143].

3.1 Introduction: biomimetic membrane fusion

Membrane fusion is a biological process in which two initially separate membrane compartments merge, leading to the mixing of both membrane lipids and internal aqueous contents [144]. It enables a variety of essential cellular functions, including extracellular trafficking [145], synaptic transmission [146], fertilization [147], and viral entry [148]. Due to the key role of these mechanisms, it is crucial to understand how fusion occurs, which minimal components are required, what triggers it, and how it progresses. This knowledge is necessary not only to address mechanistic questions in basic research, but also to develop synthetic systems that control and mimic lipid membrane fusion for biomedical applications, including targeted drug delivery systems [149–151].

Vesicle fusion is a multi-step process (Figure 3.1). During the initial stage of fusion (*docking*), the two membranes are closely apposed and are separated by only a few nanometers ($< 5\,\text{nm}$). This stage is followed by the formation of a narrow lipid bridge between the apposed membranes, known as *stalk*, which represents a key intermediate in membrane fusion. During stalk formation, mixing of the lipids of the outer membrane leaflets occurs. The stalk then expands and becomes thinner forming the *hemifusion diaphragm*. The following step is the formation of the *fusion pore*, which allows mixing of both the inner leaflet lipids and the aqueous contents. These stages are general intermediates of the fusion process and can be observed both *in vivo* and in *in vitro* systems. In general, the kinetics of membrane fusion is regulated by energy barriers that have to be overcome to complete the fusion process [152].

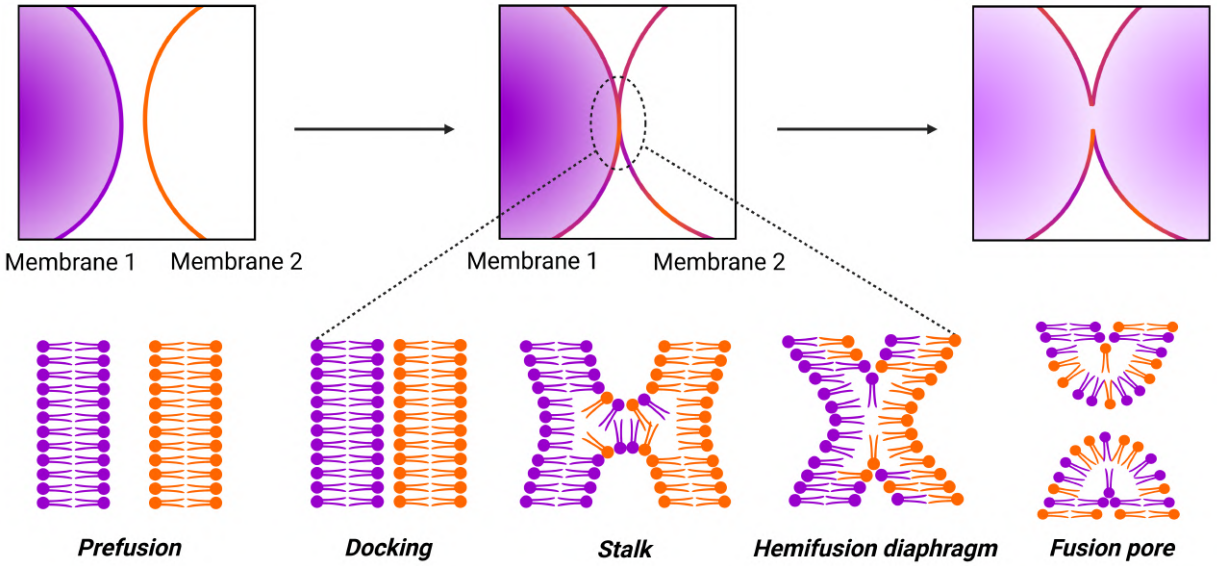

Figure 3.1 – ***Membrane fusion mechanism.*** *The upper row represents a low resolution view of two membranes, with their aqueous compartments, coming into contact. In the lower row is represented what happens from a molecular point of view. In the initial state, the two vesicles are well-separated. After overcoming the dehydration barrier, vesicle membranes are close and hydrophobic contacts between apposed membranes occur, leading to the stalk formation and the mixing of outer leaflet lipids. From the hemifusion diaphragm the process proceeds to the fusion pore formation, resulting into a single vesicle with mixed lipids and mixed contents from the two starting vesicles. Reprinted from Leonardini et al. [153], licensed under CC BY-NC 3.0.*

In the biological context, the fusion of lipid vesicles with target membranes is precisely controlled by sophisticated families of fusogenic proteins [154]. A representative example is the Soluble N-ethylmaleimide-sensitive factor Attachment protein REceptors (SNARE) family, which mediates synaptic transmission in neuronal cells (Figure 3.2**a**) [155–157].

In vivo, these protein-mediated mechanisms are indispensable for ensuring both the efficiency and specificity of the fusion process. Nevertheless, each stage of fusion is also strongly modulated by the surrounding physico-chemical environment, particularly lipid composition, ionic conditions, pH, and temperature, which collectively shape the membrane

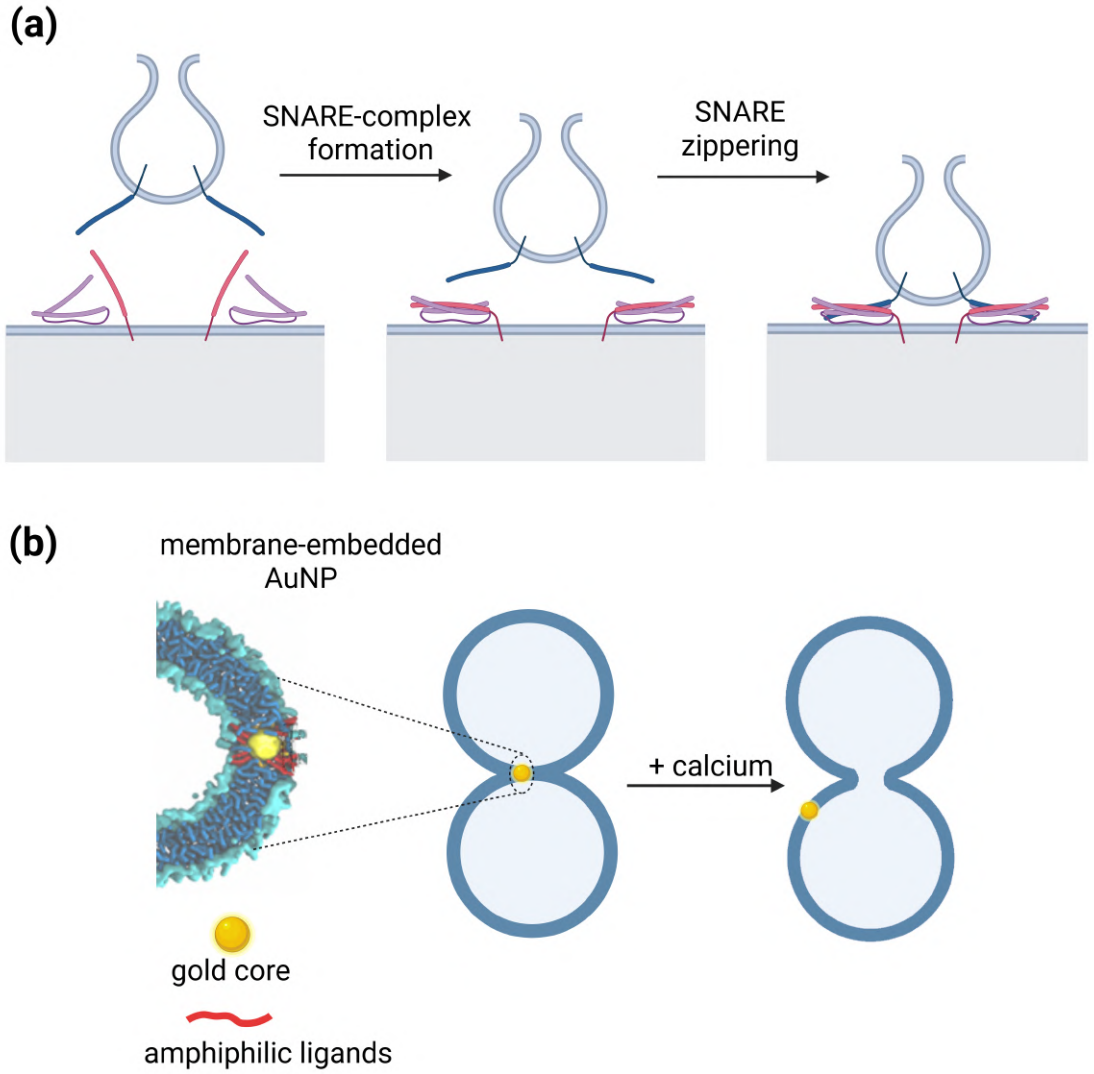

Figure 3.2 – ***Examples of membrane fusion mechanisms in vivo and in vitro.*** **(a)** *Schematic representation of the SNARE-mediated fusion mechanism.* **(b)** *AuNPs penetrate into the hydrophobic region of the lipid bilayer thanks to their amphiphilic coating and surface charge. The AuNPs presence reduces the critical energy barriers for initial membrane apposition and stalk formation, while fusion pore formation is triggered by calcium ions. Reprinted from Leonardini et al. [153], licensed under CC BY-NC 3.0.*

energy landscape. Lipids play a fundamental role, regulating membrane curvature, elasticity, and mechanical properties. Lipids promoting negative spontaneous curvature and membrane fluidity enhance stalk and pore formation [158], whereas rigid membranes disfavour fusion [159]. Cholesterol can modulate membrane fusion in a context-dependent manner, either promoting or inhibiting the process. In systems where fusion is a mediated process, e.g., by proteins or synthetic agents, cholesterol has been shown to enhance fusion by increasing line tension at domain interfaces or by modulating the activity of fusion mediators [92, 160–162]. Conversely, in model membranes, cholesterol can increase membrane bending rigidity, stabilizing hemifusion intermediates and hindering pore formation [159, 163, 164]. For example, in GUV-based systems, cholesterol has been reported to reduce fusion efficiency while increasing

mechanical resistance to pore opening [159, 164]. Furthermore, the presence of charged lipids can facilitate docking between membranes of opposite charge through electrostatic interactions [165, 166]. Ionic concentrations and pH levels are additional parameters that have to be finely tuned for fusion efficacy. Ions are classic fusogens, which lower membrane hydration barriers, create bridges between charged lipid headgroups, and promote close membrane proximity [167, 168]. pH also influences the charge state of lipids; for example, *in vivo*, certain viral fusion proteins act as pH sensors, with acidic conditions triggering conformational changes that initiate the fusion process [169, 170]. Temperature can also regulate membrane fluidity by modulating lipid phase transitions, and lateral mobility of both lipids and proteins involved in the fusion process [171, 172].

Artificial membrane fusion systems are designed to replicate protein-mediated fusion mechanisms in a controlled environment for specific applications. Synthetic fusogenic agents that mimic *in vivo* processes include fusogenic peptide sequences [151, 173, 174], complementary oligonucleotide strands [175–177], polymers [178, 179], and engineered inorganic NPs [90, 180–182]. Biomimetic studies with NPs have shown that their major advantage as fusogenic agents lies in their tunable physico-chemical properties. Key structural parameters of NPs include the material, size, shape of the NP core, and the surface functionalization. These characteristics determine how effectively NPs interact with lipid membranes and promote fusion [92, 183, 184].

The amphiphilic AuNPs employed for this thesis work tend to insert and stabilize within the hydrophobic core of the membrane, thereby activating fusion pathways that closely resemble protein-inspired fusogenic mechanisms [90]. These NPs reduce the critical energy barriers associated with the initial membrane approach and stalk formation through sulfonate-lipid interactions, and, upon calcium triggering, the stalk expands into a fusion pore. Figure 3.2**b** schematically illustrates this mechanism.

In this chapter, I explore how the interplay between NP size and membrane curvature affects vesicle fusion. Vesicles composed of DOPC and cholesterol were used. Previous studies showed that NPs can induce fusion of DOPC vesicles, which otherwise do not fuse spontaneously. Moreover, Canepa et al. demonstrated that increasing cholesterol content enhances fusion efficiency by promoting hydrophobic contacts between apposing membranes. Simulations further suggested that cholesterol accumulation at the stalk may contribute to its stabilization. The aim of this work is to elucidate mechanisms underlying vesicle fusion with different NP sizes and membrane curvatures, which influence local membrane deformations and the stability of fusion intermediates. To this end, experimental and computational approaches were combined to provide a detailed view of the process.

3.2 Materials and methods

3.2.1 Lipid vesicles preparation and characterization

Vesicle preparation. DOPC vesicles containing a biologically relevant cholesterol fraction (DOPC:chol 70:30 $\frac{\text{mol}}{\text{mol}}$) were prepared. MLVs were obtained by hydrating a dry DOPC/chol lipid film, followed by sonication of the lipid suspension. For lipid mixing and QCM-D experiments, the hydration was performed using a buffer containing 2.5 mM Trizma® base and 50 mM NaCl (pH 7.4), whereas for content mixing experiments an aqueous solution containing 50 mM self-quenched SRB and 2.5 mM Trizma® base (pH 7.4) was used.

Subsequently, unilamellar vesicles were obtained by extrusion using an Avanti Mini-Extruder (Avanti Polar Lipids) equipped with polycarbonate membranes of varying pore sizes (Whatman) (see Appendix A for more details).

For the FRET-based lipid mixing assay (Section 2.1.1), vesicle bilayers were labeled with 0.5 mol % of a donor lipid (18:1 NBD-PE) and 0.5 mol % of an acceptor lipid (18:1 Rhod-PE). Two distinct populations of vesicles (LUVs and SUVs) with different membrane curvatures were prepared. LUVs unlabeled and labeled with NBD-PE and Rhod-PE were obtained by extruding MLVs 25 times through a 0.1 µm membrane. SUVs were obtained via sequential extrusion through progressively smaller pore membranes: 31 times through 0.1 µm, and 0.05 µm membranes, and 13 times through 0.03 µm membrane.

For the content mixing assay (Section 2.1.2), two distinct vesicles population were prepared. SRB-loaded LUVs were obtained by extruding MLVs 19 times through 0.1 µm membrane. For SRB-loaded SUVs, 17, 17, and 13 extrusions were performed through 0.1 µm, 0.05 µm, and 0.03 µm membranes, respectively. Subsequently, vesicles were purified from unencapsulated SRB using a minicolumn centrifugation technique (Sephadex® G-50 Medium gel, centrifugation at 3000 rpm for $(1-2)$ min) to remove dye from the external medium, ensuring that SRB remained only in the vesicle lumen. Lipid concentrations were 2 mg mL^{-1}.

For the QCM-D experiments, unlabeled DOPC:chol 70:30 LUVs were prepared by extrusion at a lipid concentration of 4 mg mL^{-1}.

All vesicle suspensions were stored at 4 °C, with fluorescent batches protected from light.

Vesicle characterization. The hydrodynamic diameters of the vesicles were characterized by DLS measurements conducted at room temperature using a Zetasizer Nano ZS instrument (Malvern Panalytical). The scattered light was collected in backscattering mode at 173°. Measurements were performed on vesicles immediately after extrusion without further dilution, except for SRB-loaded vesicles, for which sizes were determined after filtration. The results are reported in Figure 3.3.

3.2.2 AuNPs characterization

Monodisperse AuNPs with a ligand ratio of 2:1 MUS:OT (68 mol % MUS and 32 mol% OT) and two different gold core diameters, (2.4 ± 0.4) nm and (4.8 ± 0.5) nm, were employed. Hereafter, they will be referred to as small and large AuNPs, respectively. Brief details on the AuNP synthesis are reported in Appendix B. After the synthesis, small and large AuNPs were characterized by Transmission Electron Microscopy (TEM) and ^{1}H Nuclear Magnetic Resonance (NMR) to determine the core size and the ligand ratio, respectively.

I prepared AuNP suspensions in aqueous solution at concentrations of $0.73\,\mathrm{mg\,mL^{-1}}$ for small NPs and $5\,\mathrm{mg\,mL^{-1}}$ for large NPs. This adjustment ensured that an equivalent volume of NP solution was added in fluorescence experiments, corresponding to the same number of particles for small and large AuNPs in the cuvette. Before all experiments, AuNPs were sonicated in an ultrasonic bath for a few seconds. In general, these AuNPs exhibited remarkable long-term colloidal stability in water, and their dispersions did not require further manipulation before use. The molecular weight (MW) of the small NPs was calculated to be $68.689\,\mathrm{g\,mol^{-1}}$, while that of the large NPs was $470.836\,\mathrm{g\,mol^{-1}}$. See Appendix C for details on MW calculation. DLS and zeta potential control measurements were performed prior to all experiments involving lipid vesicles. DLS data confirmed the absence of aggregates and provided the hydrodynamic diameters of the AuNPs, while Zeta Potential measurements indicated the colloidal stability of the AuNP suspensions. UV-Vis spectra were acquired to evaluate the absorbance of NPs at the LSPR peak using a UV-1900 spectrophotometer (Shimadzu). The characterization data are reported in Figure 3.4 and Table 3.1.

3.3 Experimental methods

3.3.1 Fluorescence assays

I investigated fusion mechanisms triggered by calcium ions (Ca^{2+}) and mediated by small and large AuNPs, for both curvatures of lipid vesicles. Fluorescence experiments were conducted at 25 °C using a Fluorolog-3 spectrofluorometer (Horiba Jobin-Ivon) with a Suprasil® quartz cuvette (Hellma®, semi-micro, light path 10 mm × 4 mm) under continuous stirring. For each experiment, the final lipid concentration was 0.32 mM in a total volume of 850 µL.

For the lipid mixing assay, unlabeled vesicles and vesicles labeled with NBD-PE and Rhod-PE were mixed in a 4:1 molar ratio. Samples were excited at $\lambda_{exc} = 470\,\mathrm{nm}$, corresponding to the characteristic excitation maximum of the donor fluorophore NBD-PE. The fluorescence emission of NBD-PE was monitored over time at $\lambda_{em,1} = 530\,\mathrm{nm}$, while the emission of the acceptor fluorophore Rhod-PE ($\lambda_{exc} = 540\,\mathrm{nm}$) was recorded at $\lambda_{em,2} = 585\,\mathrm{nm}$.

For the content mixing assay, unlabeled vesicles and SRB-loaded vesicles were mixed at a 2:1 molar ratio. SRB was excited at $\lambda_{exc} = 565\,\mathrm{nm}$ and its fluorescence emission was continuously recorded at $\lambda_{em} = 586\,\mathrm{nm}$.

For experiments with large vesicles, a fixed molar ratio $R = \frac{\text{mol lipids}}{\text{mol NPs}} = 5800$ (≈ 13 AuNPs per vesicle) was used. For small vesicles, experiments were performed at $R = 5800$ (≈ 3 AuNPs per vesicle) and $R = 2320$ (≈ 7 AuNPs per vesicle). The value of R in the cuvette was estimated from the volume of stock solution added and the AuNP molecular weight. The number of vesicles was estimated using the number of lipids per vesicle, calculated as:

$$N_{\text{tot}} = \frac{4\pi(\frac{d}{2})^2 + 4\pi(\frac{d}{2} - h)^2}{a} \tag{3.1}$$

where d is the vesicle diameter, h is the bilayer thickness ($\approx 5\,\text{nm}$), and a is the headgroup area ($\approx 0.71\,\text{nm}^2$ for phosphocholine). For each AuNP size, the same volume (4.4 µL for $R = 5800$ and 11 µL for $R = 2320$) was added from stock solutions at different concentrations ($0.73\,\text{mg}\,\text{mL}^{-1}$ for small NPs and $5\,\text{mg}\,\text{mL}^{-1}$ for large NPs) to obtain the same number of AuNPs in cuvette. In both lipid and content mixing experiments, fusion was triggered by adding 10 µL of a 170 mM $CaCl_2$ stock solution to achieve a final Ca^{2+} concentration of 2 mM. Unless otherwise specified, AuNPs were incubated with vesicles for 15 min before Ca^{2+} addition.

For lipid mixing experiments (see Figure 3.5**a** for a representative fluorescence signal raw curve), time-dependent rhodamine emission data, $F_{\text{Rhod}}(t)$, were normalized by the initial fluorescence measured in control experiments without AuNPs, $F^{\text{blank}}_{0,\text{Rhod}}$, as follows:

$$\Delta F^{\text{Rhod}}_{\text{norm}}(\%) = \frac{F_{\text{Rhod}}(t) - F_{0,\text{Rhod}}}{F^{\text{blank}}_{0,\text{Rhod}}} \cdot 100 \tag{3.2}$$

For content mixing experiments (see Figure 3.7**a** for a representative fluorescence signal raw curve), SRB fluorescence data were normalized using the maximum fluorescence after vesicle lysis with detergent (0.9 % w/v sodium cholate), $F_{\text{max,SRB}}$, as follows:

$$\Delta F^{\text{SRB}}_{\text{norm}}(\%) = \frac{F_{\text{SRB}}(t) - F_{0,\text{SRB}}}{F_{\text{max,SRB}} - F_{0,\text{SRB}}} \cdot 100 \tag{3.3}$$

where $F_{0,\text{Rhod/SRB}}$ is the mean fluorescence before Ca^{2+} addition, $F_{\text{Rhod/SRB}}(t)$ is the fluorescence signal during the recording, and $F_{\text{max,SRB}}$ is the maximum fluorescence measured after vesicle rupture.

3.3.2 QCM-D

DOPC:chol 70:30 unlabelled LUVs were freshly prepared before the experiments. All measurements were performed using a QCM-Z500 microbalance (KSV Finland LLC) at a fixed temperature of 25 °C, employing a thermostated flow chamber. The same experimental procedure was followed for experiments with both small and large AuNPs. Gold-coated sensors were used to enable the formation of a supported vesicle layer (SVL). Starting from a vesicle stock concentration of $4\,\text{mg}\,\text{mL}^{-1}$, the vesicles were diluted to a final concentration

of 0.25 mg mL^{-1} prior to injection into the chamber. First, the adsorption of vesicles on the sensor was monitored. Once the frequency signal stabilized at a plateau, excess of unsupported vesicles was rinsed out. Subsequently, aliquots of 0.01 mg mL^{-1} small AuNPs or 0.07 mg mL^{-1} large AuNPs were added to the chamber to obtain the same particle concentration of 0.15 µM. The uptake of AuNPs into the membrane was recorded until the frequency signal reached a plateau, followed by a rinsing step to remove unbound AuNPs. The number of AuNPs per vesicle was estimated as follows (see Figure 3.6**a,b** for step numbering). First, for each overtone ($3^{rd}, 5^{th}, 7^{th}, 9^{th}, 11^{th}$), Δf_{SVL} was calculated as the difference between the average frequency values between step 2 and step 3 and the average frequency before the addition of vesicles (step 1). Second, Δf_{NP} was calculated as the difference between the average frequency values between step 4 and step 5 and the average between step 2 and step 3. The mean value for each Δf was obtained by averaging all overtones. The mass changes, Δm_{SVL} and Δm_{NP}, were derived using a modified Sauerbrey model [91] to account for the viscoelastic properties of the system:

$$\Delta m = -C_f \frac{\Delta f}{\sqrt{n}} \tag{3.4}$$

where C_f is the sensitivity coefficient of the quartz crystal sensor 17.7 ng cm^{-2} Hz^{-1}, n is the overtone number, and $\Delta f/\sqrt{n}$ is the normalized frequency Δf_{norm}. Finally, the mass of a vesicle of 100 nm diameter (m_{ves}) and the mass of a single NP (m_{NP}) were used to calculate the number of vesicles on the sensor, $N_{ves} = \Delta m_{SVL}/m_{ves}$, and the number of NPs on the sensor, $N_{NP} = \Delta m_{NP}/m_{NP}$, respectively. The ratio $R = N_{NP}/N_{ves}$ was then calculated.

To evaluate the net mass attached to the SVL+AuNP layer, for each overtone the difference in frequency between the point after step 8 and the point before step 7 was calculated.

3.4 Results and discussion

Experimental results. DLS measurements performed on the vesicles after extrusion provided information on their hydrodynamic diameters. Analysis of the intensity size distributions (Figure 3.3) confirmed that the two vesicle populations are well-separated in size for all preparations (unlabeled vesicles, labeled vesicles for lipid mixing and SRB-labeled vesicles for content mixing). In the following, one population will be referred to as large vesicles and labeled with a representative diameter of 100 nm, whereas the other population will be referred to as small vesicles and labeled with a representative diameter of 50 nm.

Regarding the NPs, Figure 3.4**a,d** shows TEM images of the gold cores acquired immediately after synthesis, together with the corresponding histograms of the core size distributions (Figure 3.4**b,e**). This technique provides information on the core sizes while neglecting the contribution of the amphiphilic coating. To gain further insights into the overall nanoparticle

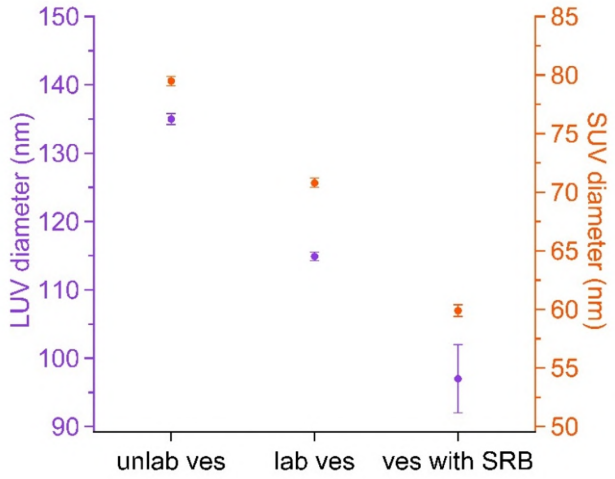

Figure 3.3 – *Hydrodynamic diameters of large and small lipid vesicles measured for unlabeled vesicles, vesicles labeled with NBD-PE and Rhod-PE, and vesicles loaded with self-quenched SRB. Mean values were obtained from intensity-weighted size distributions ($N = 18$). Error bars were calculated using Student's t-statistics with a confidence level of 95 %. Reprinted from Leonardini et al. [143], licensed under CC BY-NC 3.0.*

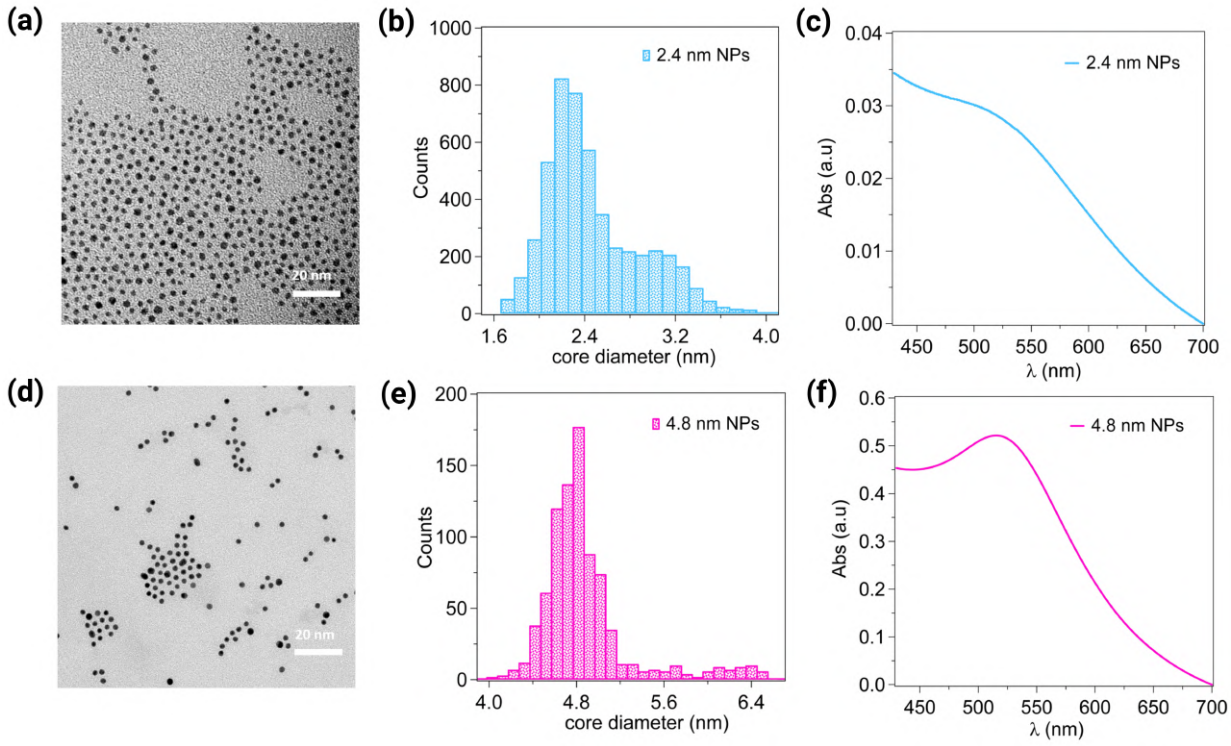

Figure 3.4 – **(a, d)** *Bright-field TEM images of monodisperse 2:1 MUS:OT small and large AuNPs, with gold core diameters of* (2.4 ± 0.4) nm *and* (4.8 ± 0.5) nm, *respectively.* **(b, e)** *Distributions of the gold core diameters.* **(c, f)** *UV-Vis spectra of small and large AuNPs acquired in ultrapure Milli-Q water at the same nanoparticle molar concentration of* 0.11 µM, *corresponding to* 0.05 mg mL^{-1} *for large AuNPs and* 0.008 mg mL^{-1} *for small AuNPs. Reprinted from Leonardini et al. [143], licensed under CC BY-NC 3.0.*

size, DLS measurements of the hydrodynamic diameter were performed both in water and in the experimental buffer. The values obtained from these measurements indicate that the NPs can be clearly distinguished into two populations with different sizes. In addition, the zeta potential was measured in both water and buffer, and the high absolute values obtained ($|\zeta| > 30$ mV) indicate that the NPs exhibit good colloidal stability under both conditions. All the data are summarized in Table 3.1.

Table 3.1 – *AuNPs were characterized after synthesis by TEM and ^{1}H-NMR, and before each experiment to assess their size (DLS) and colloidal stability (ζ-potential).*

TEM[a]	^{1}H-NMR[b]	DLS – hydrodynamic diameter (nm)[c]		ζ-potential (mV)[d]	
core diameter (nm)	OT mol %	water	buffer	water	buffer
2.4 ± 0.4	32 ± 5	2.9 ± 0.4	8.4 ± 0.7	-51 ± 4	-43 ± 3
4.8 ± 0.4	32 ± 5	5.7 ± 1.4	10.8 ± 0.9	-59 ± 3	-45 ± 3

[a] *mean ± one standard deviation.*
[b] *mean ± error calculated using Student's statistics (95 % confidence level, $N = 3$).*
[c] *mean ± error calculated using Student's statistics (95 % confidence level, at least $N = 12$).*
[d] *mean ± error calculated using Student's statistics (95 % confidence level, at least $N = 6$).*

The NP-mediated vesicle fusion process was investigated by combining fluorescence spectroscopy assays and QCM-D measurements. Membrane fusion was first probed using a lipid mixing fluorescence assay based on FRET between the donor lipid, NBD-PE, and the acceptor lipid, Rhod-PE. For these experiments, an unlabeled vesicle population and a population labeled with the two FRET probes were mixed and incubated with small or large AuNPs. Fusion was triggered by adding 2 mM Ca^{2+}, and temporal changes in the FRET signal were monitored. In Figure 3.5**a**, representative raw curves of lipid mixing are shown. The initial fluorescence signal is similar in the control experiment and in the presence of small NPs, while it is lower in the case of large NPs. This effect arises from the different absorbance properties of the AuNPs, as shown in Figure 3.4**a,d**. In particular, large AuNPs exhibit higher absorbance around the localized surface plasmon resonance peak (≈ 520 nm) compared to small AuNPs at the same concentration. As a consequence, the emission from the donor lipid NBD-PE (≈ 530 nm) is partially absorbed by the AuNPs and is therefore not fully transferred to the acceptor lipid Rhod-PE.

As discussed in Section 3.3.1, LUV experiments were conducted at the molar ratio R = 5800 ($\approx$ 13 AuNPs per vesicle), and SUVs experiments were performed at R = 5800 ($\approx$ 3 AuNPs per vesicle) and R = 2320 ($\approx$ 7 AuNPs per vesicle). Figure 3.5 show the time course of FRET-based lipid mixing signals for LUVs at R = 5800 (Figure 3.5**b**), SUVs at R = 5800 (Figure 3.5**c**) and R = 2320 (Figure 3.5**d**). Compared to the control experiment without NPs (green curve), which exhibits a flat Rhod-PE fluorescence signal, experiments with NPs show a decrease in Rhod-PE fluorescence after Ca^{2+} injection (blue and pink curves), indicating that lipid mixing occurred. This increased the spatial distance between

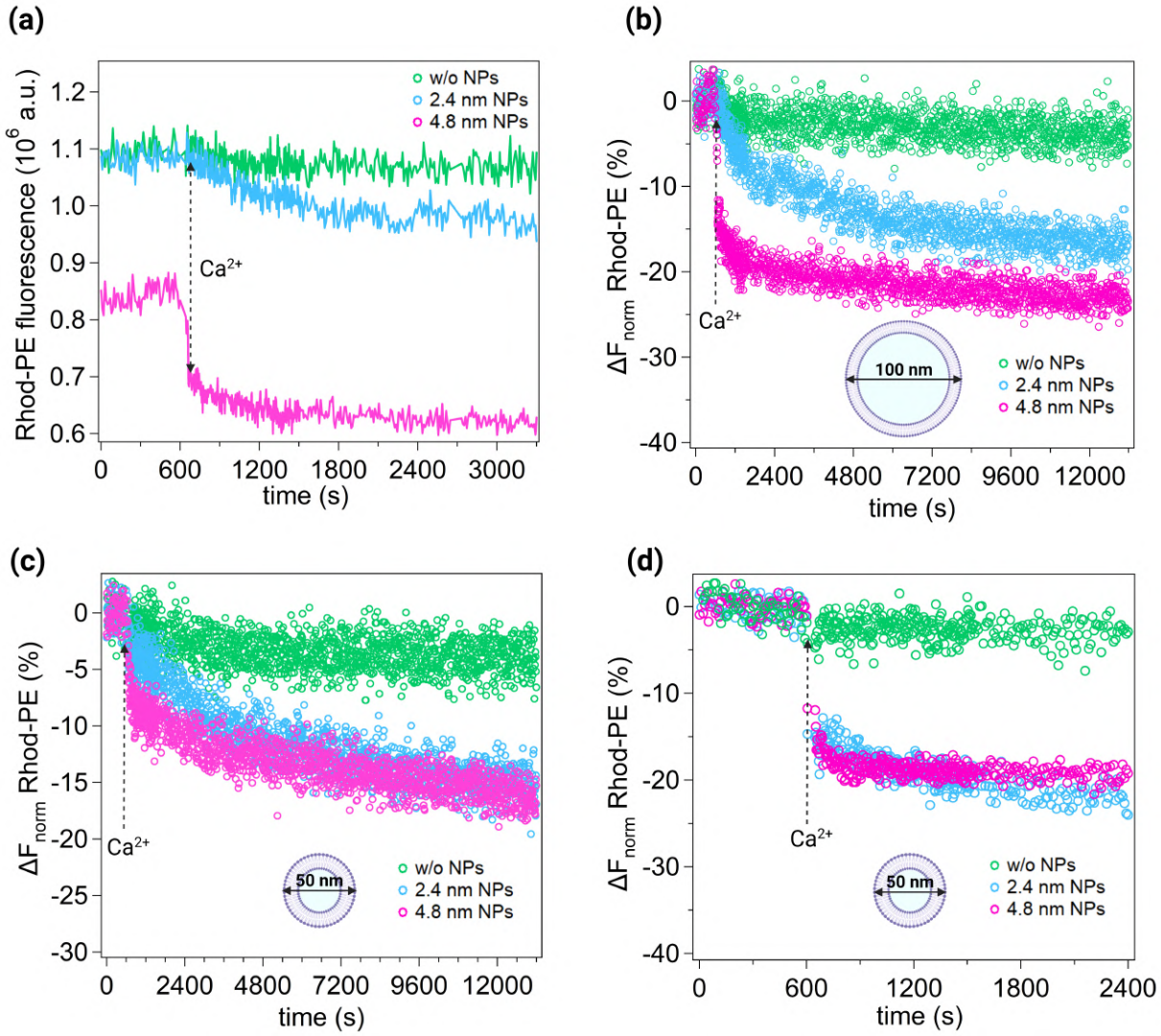

Figure 3.5 – ***Lipid mixing assay.*** **(a)** *Representative raw curves of lipid mixing experiments performed in the absence of NPs (green curve) and in the presence of small and large NPs (blue and pink curves, respectively). The curves show the initial fluorescence intensity (F_0) and the decrease in Rhod-PE fluorescence signal following Ca^{2+} injection. The differences observed in the F_0 values of Rhod-PE between small and large NPs are discussed in the text.* **(b-d)** *Normalized reduction (%) of the real-time Rhod-PE fluorescence signal. A lipid mixing assay based on FRET was performed using DOPC:chol 70:30 (mol %) vesicles with different membrane curvatures. LUVs and SUVs were preincubated for 15 min with AuNPs at a molar ratio $R = 5800$ for LUVs* **(b)** *and $R = 5800$* **(c)** *and $R = 2320$* **(d)** *for SUVs. Only the last 10 minutes of the preincubation are shown. After Ca^{2+} injection (2 mM at 600 s; dashed arrows), lipid mixing led to a decrease in the Rhod-PE fluorescence signal in the presence of both small and large NPs. This behaviour, observed for both vesicle curvatures, indicates membrane remodelling due to vesicle-vesicle interactions mediated by AuNPs. Adapted from Leonardini et al. [143], licensed under CC BY-NC 3.0.*

FRET donor and acceptor, resulting in a decreased acceptor signal. For LUVs, the Rhod-PE fluorescence intensity decreases until reaching a stable signal after a few hours. In SUVs experiments, a decrease in Rhod-PE fluorescence is also observed for both values of R. In the condition with fewer NPs per vesicle, the fluorescence reaches a more stable signal at longer times compared to the condition with a higher number of NPs per vesicle, where the plateau is reached approximately 30 min after Ca^{2+} addition.

To further investigate interactions between vesicles and AuNPs of different sizes, QCM-D measurements were performed using DOPC:chol 70:30 mol % LUVs. Gold-coated QCM sensors were employed to form a supported vesicle layer (SVL), allowing vesicles to adhere without merging [185]. This provides a viscoelastic system suitable for studying interactions with NPs and other vesicles. Interactions between $(2-5)$ nm core size AuNPs and membranes have been previously demonstrated using confocal, electron, atomic force microscopy, and electrophysiology studies [87, 88, 186]. Figure 3.6 shows two representative QCM-D experiments, one performed with large NPs and the other with small NPs, with all the experimental steps indicated. Consistent with the findings obtained from the other techniques and with our previous SVL results [91, 92], QCM-D data showed that small AuNPs passively penetrate the membrane. Large AuNPs also stably interact with the membrane, but their entry kinetics are slower (steps 3-4). The number of NPs per vesicle was estimated to be approximately 94 for small AuNPs and 84 for large AuNPs. Following NP uptake, QCM-D was used to detect mass changes induced by vesicle fusion events. Ca^{2+}-triggered vesicle fusion was tested for both NP sizes. Control measurements were performed by injecting additional Ca^{2+}-free vesicles (step 5), showing no significant frequency changes. After ≈ 15 minutes, a rinse was performed (step 6), followed by the addition of vesicles with 2 mM Ca^{2+} (step 7), and a final rinse to remove unbound material (step 8). Different behaviours of the SVL were observed in the presence of small and large NPs. With large NPs, a larger frequency decrease was observed compared to small NPs, indicating that more vesicles bind to the SVL. This behaviour was coherent with dissipation measurements: a decrease in frequency corresponded to an increase in dissipation, suggesting increased viscoelasticity due to water-filled vesicles, more pronounced with large NPs. After the final rinse, frequency increased and dissipation decreased in the presence of large NPs, indicating removal of weakly bound material. No material was washed away with small NPs, revealing stable vesicle attachment. In both cases, after step 8, a fraction of vesicles remained bound to the SVL, suggesting hemifusion or fusion events. The remaining mass after the final rinse (step 8) was found to be similar for small and large NPs, corresponding to $(1.18 \pm 0.07)\,\mu g\,cm^{-2}$ and $(1.28 \pm 0.05)\,\mu g\,cm^{-2}$, respectively (see Section 3.3.1 for calculation details).

To distinguish hemifusion from complete fusion, content mixing assays were performed using the self-quenched dye SRB [92, 104]. Two vesicle populations with the same size and lipid composition were prepared: one loaded with 50 mM SRB [90, 105] and the other without dye. Upon fusion, vesicle contents mix, leading to dilution of SRB, its dequenching,

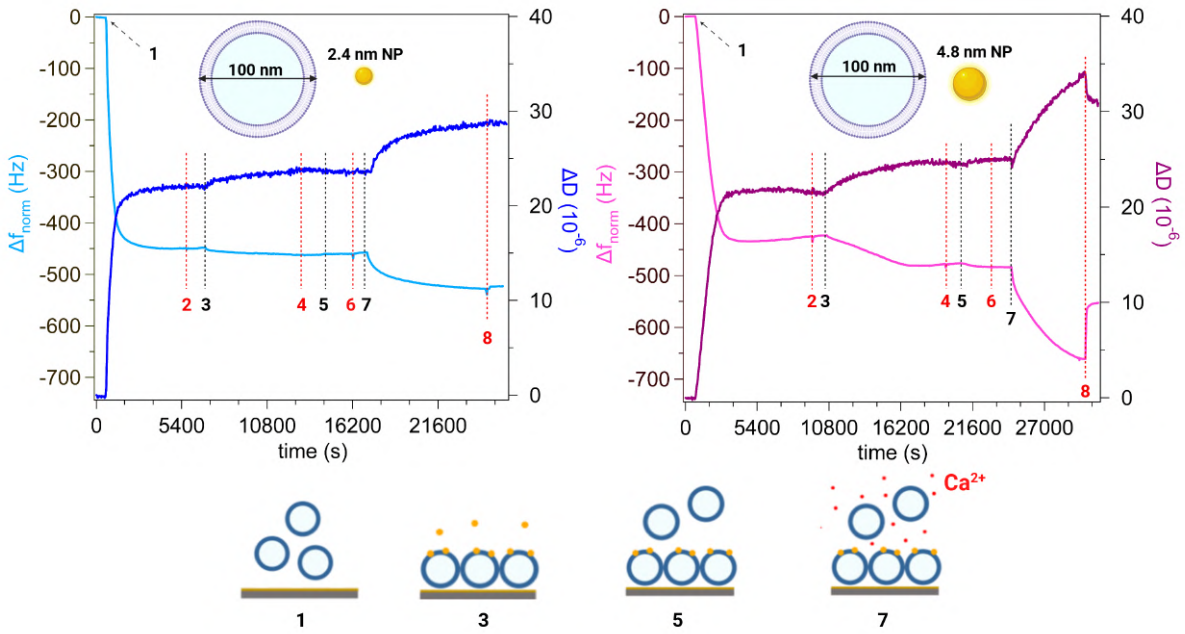

Figure 3.6 – ***QCM-D measurements.*** *Representative QCM-D curves (5^{th} overtone) showing the normalized frequency shift (ΔF_{norm}) and dissipation (ΔD).* **(a)** *Experiments involving small NPs interacting with large DOPC:chol 70:30 (mol%) vesicles.* **(b)** *Experiments involving large NPs interacting with large DOPC:chol 70:30 (mol%) vesicles. Both experiments were performed under identical conditions (lipid concentration* $0.25\,\mathrm{mg\,mL^{-1}}$ *and AuNP concentration* $0.15\,\mu\mathrm{M}$*) and followed the same experimental procedure, with the individual steps numbered in the graphs. The red dashed lines indicate rinsing steps, during which a complete exchange of solution in the QCM-D chamber occurs and all material not adhered to the sensor surface is removed. The black dashed lines indicate the steps represented by the cartoons shown below the graphs. The gold-coated sensor was allowed to equilibrate in buffer for 600 s prior to vesicle addition. The first pronounced decrease in frequency corresponds to the formation of the supported vesicle layer (SVL) (1, vesicle addition; 2, rinse of vesicles not adhering to the sensor). The second decrease corresponds to the uptake of AuNPs into the membrane (3, NP addition; 4, rinse of non-uptaken NPs). Subsequently, a control step was performed by introducing vesicles in the absence of calcium into the chamber (5, vesicle addition; 6, rinse). The third step (7, vesicle and* Ca^{2+} *addition; 8, rinse) corresponds to vesicle fusion or hemifusion with the SVL, triggered by the presence of calcium (red points in cartoon 7). Cartoons are not to scale. See Section 3.3.2 for full details on the experimental setup and data analysis. Adapted from Leonardini et al. [143], licensed under CC BY-NC 3.0.*

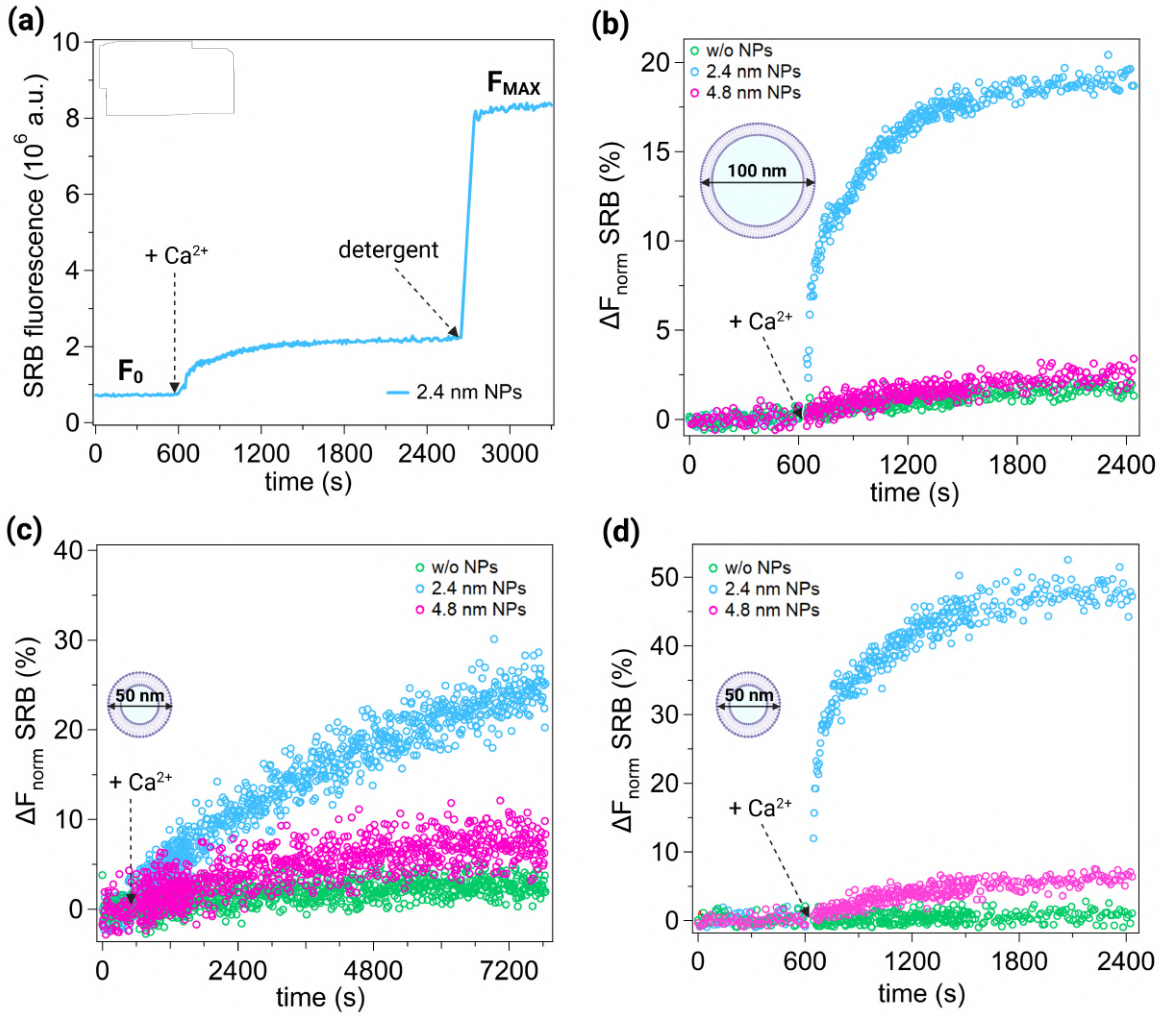

Figure 3.7 – ***Content mixing assay.*** **(a)** *Representative raw curve of a content mixing experiment with small NPs, showing the initial fluorescence level F_0, the Ca^{2+} injection, the increase in fluorescence signal due to SRB dilution, and the addition of the detergent sodium cholate, which causes the rupture of vesicles and results in the maximum dilution of SRB (F_{max}).* **(b, c)** *Normalized increases (%) of real-time SRB fluorescence signal of DOPC:chol 70:30 vesicles of different membrane curvatures are shown. LUVs and SUVs were incubated for* 15 min *with AuNPs at a molar ratio $R = 5800$, corresponding to 13 AuNPs per vesicle and 3 AuNPs per vesicle, respectively.* **(d)** *SUVs were incubated at $R = 2320$ (7 AuNPs per vesicle). Only the last* 10 min *of preincubation are shown in each plot. After* 600 s, 2 mM Ca^{2+} *were added (dashed arrows). In the presence of vesicles with membranes of low curvature (i.e. LUVs), the fluorescence emission of SRB (%) increases significantly when vesicles are incubated with small AuNPs (blue curve), suggesting mixing of vesicle contents. However, when large AuNPs are used (pink curve), an increase in SRB fluorescence emission is not observed and the signal overlaps that of the control without AuNPs (green curve). In the presence of more curved membranes (i.e. SUVs), a significant increase in the SRB signal is observed with small NPs (blue curve), while, unlike the case with LUVs, even with large NPs a slight increase in fluorescence is observed (pink curve). The latter is indeed distinct from the control experiment (green curve). Adapted from Leonardini et al. [143], licensed under CC BY-NC 3.0.*

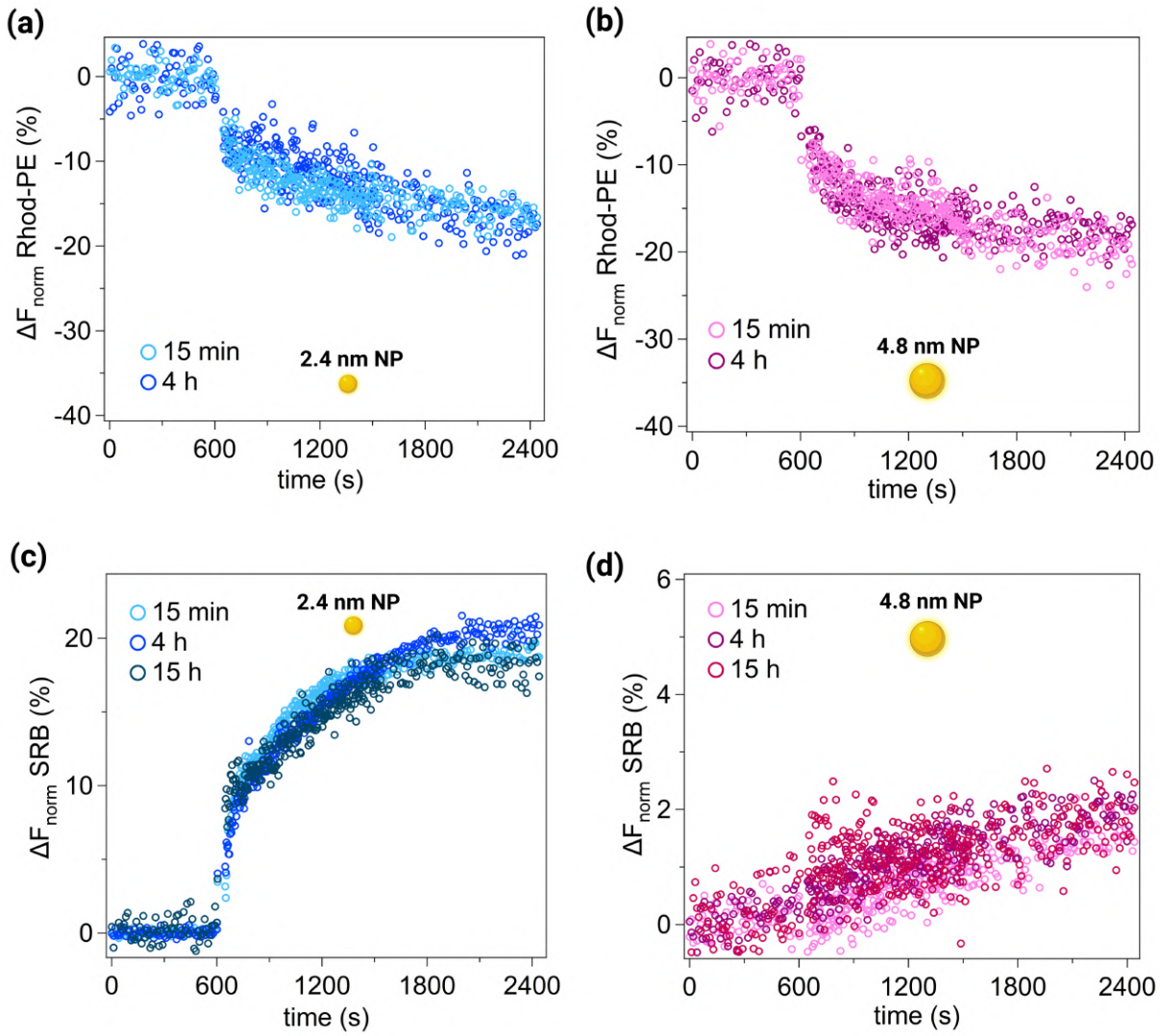

Figure 3.8 – *Real-time lipid mixing and content mixing fluorescence assays at different preincubation times of small and large AuNPs with DOPC:chol 70:30 LUVs.*
(a, b) *Normalized decrease (%) of Rhod-PE emission signal due to lipid mixing after calcium injection.* **(c, d)** *Normalized increase (%) of SRB emission signal due to vesicle content mixing after calcium injection. Reprinted from Leonardini et al. [143], licensed under CC BY-NC 3.0.*

and an increase in the fluorescence signal. Figure 3.7**a** shows a representative raw SRB fluorescence trace as a function of time. The system initially displays a baseline fluorescence level (F_0). After the addition of 2 mM Ca^{2+} (dashed arrow), the fluorescence increases due to fusion events occurring in the system. Once a stable signal is reached, a detergent is added to disrupt all vesicles and determine the maximum fluorescence level of the system (F_{max}) in each experiment. This value is required to normalize the fluorescence curves, as described in Section 3.3.1. LUVs and SUVs were preincubated for 15 min with small or large AuNPs. Experiments used the same lipid/NP ratios as lipid mixing experiments. Small AuNPs (blue curves) induced a rapid increase in SRB fluorescence within seconds of Ca^{2+} addition, reaching a plateau of approximately 18 % within a few seconds from 30 min in the presence of large vesicles. In contrast, the curve of the control experiment and the curve with large AuNPs overlap, indicating that large NPs do not induce fusion with low-curvature membranes (Figure 3.7**b**). With highly curved membranes and a low number of NPs, small NPs exhibit different fusion kinetics (blue curve), while the fusion curve associated with larger NPs no longer overlaps with that of the control experiment (Figure 3.7**c**). Upon increasing the number of small NPs per vesicle in highly curved membranes, a pronounced content mixing is observed for small NPs, reaching a plateau value of approximately 48%. The pink curve, instead, also shows detectable fusion, distinct from the control (green curve) without AuNPs, indicating that higher membrane curvature promotes fusion events even in the presence of larger NPs (Figure 3.7**d**).

Additionally, lipid and content mixing assays at various AuNPs preincubation times were conducted. For lipid mixing, I tested incubation times of 5 min and 4 h, while for content mixing, I tested 5 min, 4 h, and overnight (15 h). As shown in Figure 3.8, the curves at different incubation times appear to overlap, indicating the same time trend.

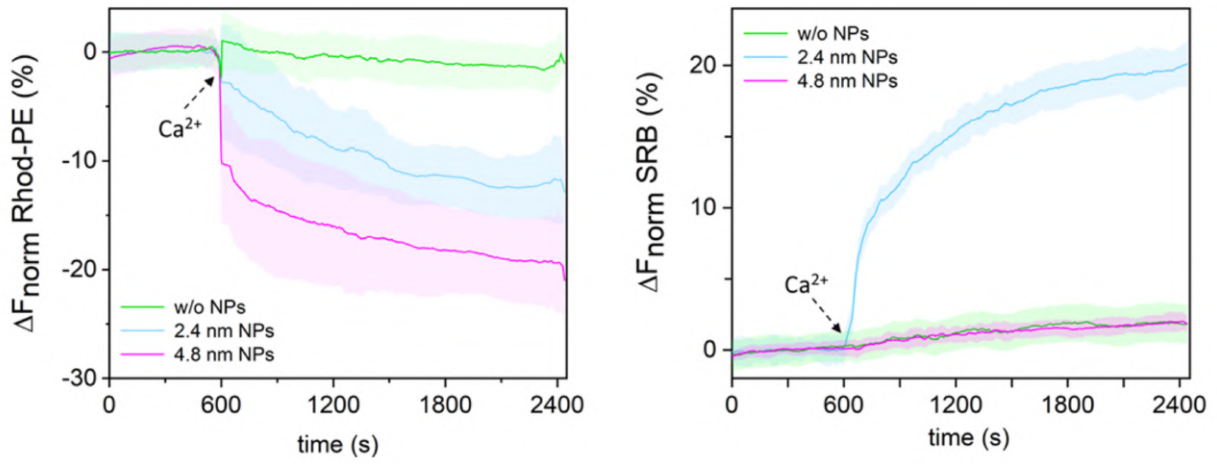

Figure 3.9 – *For lipid (left) and content (right) mixing experiments, at least 3 replicates were performed using two different LUVs batches. The resulting mean curves with their corresponding standard deviations are shown. The curves have been smoothed using a moving average. Reprinted from Leonardini et al. [143], licensed under CC BY-NC 3.0.*

To verify the reproducibility of the fusion curves acquired, experiments were repeated using different LUV batches. The resulting replicates (at least 3) were overlaid, and mean curves with corresponding standard deviations are shown in Figure 3.9. The smoothed curves confirm that the characteristic behaviors of both small (blue) and larger (pink) AuNPs are consistent across batches. These results support the robustness of the kinetic trends reported in the previous experiments.

Computational results. To add molecular details and help interpret the experimental results on the interplay between the NP and vesicle sizes, molecular dynamics (MD) simulations exploiting sub-molecular resolution coarse-grained (CG) models have been employed. The lipid bilayers (DOPC with 30 mol % cholesterol) and the MUS:OT AuNPs have been modeled with the Martini CG force-field [92, 183, 187].

The simulations focused on stalk formation of vesicles with different membrane curvatures. In particular, vesicles with diameters of 17 and 30 nm were considered. Although these sizes do not exactly match the experimental ones due to computational limitations, they allow for a meaningful comparison of curvature-dependent effects. Regarding the NPs, CG models of AuNPs with core diameters of 2 and 4 nm were employed. Umbrella sampling simulations were used to calculate the free energy profiles associated with the stalk formation [188]. As a collective variable, a modified version [183] of the chain coordinate (ξ_{ch}), originally developed by Hub et al. [163], was employed. For each simulation box in the pre-stalk configuration, a single NP was positioned so that its surface was approximately 2 nm away from the facing membrane. In the initial configuration, the NP spontaneously interacts with the upper bilayer through the charged terminal groups of the MUS ligands. An example of the simulation set-up is shown in Figure 3.10**a**, the absorbed state is referred as (A) and the stalk state is referred as (S) (see [143] for details of the system preparation). The state A was set as the zero of free energy, and the stalk stability was quantified as

$$|\Delta G| = |G_{\mathrm{min},S} - G_{\mathrm{min},A}| \tag{3.5}$$

The stalk formation is started by the establishment of a hydrophobic contact between a lipid from the opposing membrane and the hydrophobic ligands of the AuNP. Upon this interaction, the charged MUS terminal groups exposed to the aqueous phase reorganize to favor the hydrophobic connection, separating into one group anchoring the NP to the distal leaflet, and the second group surrounding the circular edge of the stalk (Figure 3.10**b**). Analysis of the free energy profiles shows that the S state corresponds to the most stable configuration. For vesicles with a diameter of 30 nm, the energy barriers are comparable for the two NP sizes. However, the free energy minimum associated with the stalk is deeper for the smaller NP core, indicating that 2 nm NPs promote stalk formation more effectively than 4 nm NPs. A similar trend is observed for membranes with higher curvature, although the

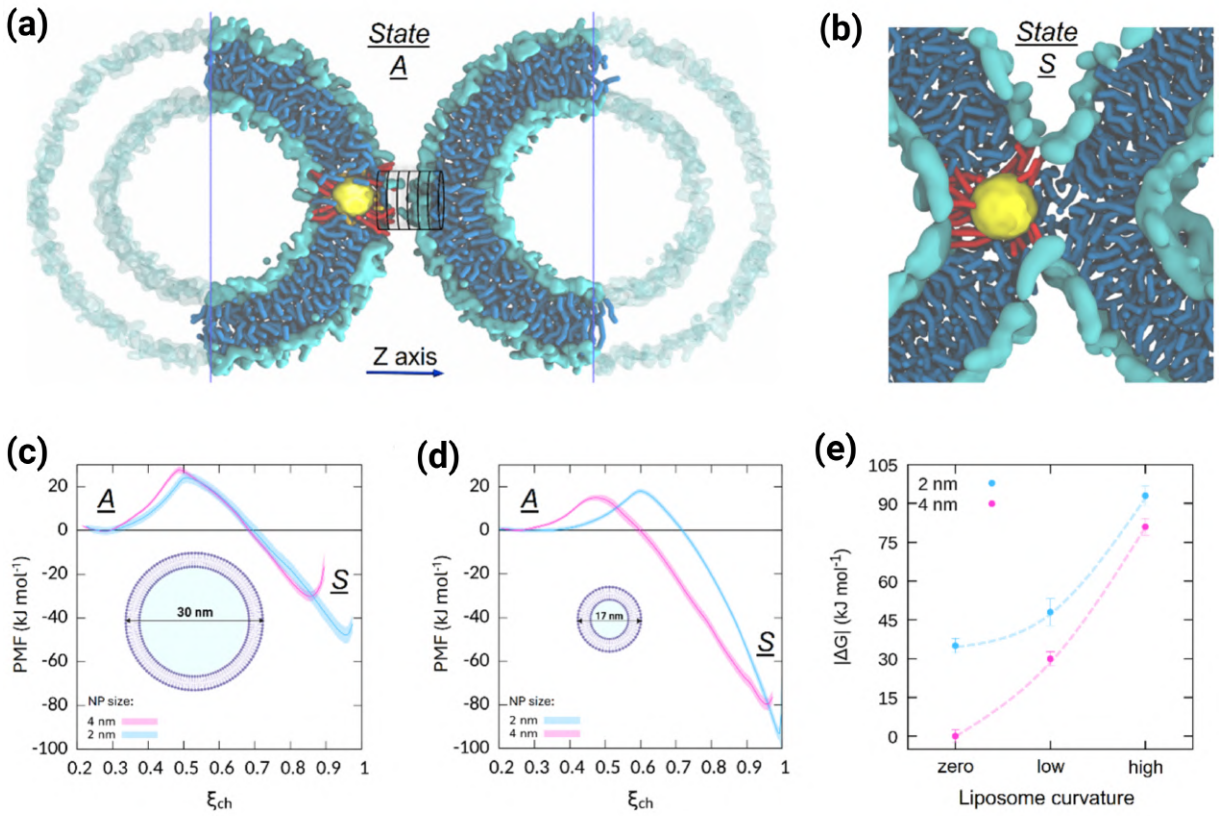

Figure 3.10 – ***Molecular dynamics simulations of stalk formation.*** **(a)** *Set-up of the simulation box showing a single vesicle interacting with itself in the region of the embedded NP thanks to periodic boundary conditions. The cilinder position used to define the coordinate chain (ξ_{ch}) is also represented. Lipid heads are in cyan, lipid tails in blue, the NP core in yellow, MUS ligands in red.* **(b)** *Snapshot of MUS ligands during stalk formation. Bottom ligands anchor the NP core to the distal leaflet, while top ligands surround the stalk edge, promoting hydrophobic membrane contacts.* **(c)** *Free energy profiles of stalk formation for the (30 nm) vesicle with both NP sizes. The energy is set to zero in state A, and in state S the minimum is more stable with small NPs compared to large NPs.* **(d)** *Free energy profiles of stalk formation for the (17 nm) vesicle with both NP sizes. For the highly curved vesicles, the difference between the minima of the two NP sizes is reduced.* **(e)** *Graph summarizing the free energy values (taken at maxima and minima, with their standard deviations) as a function of membrane curvature: zero corresponds to flat membranes (from Brosio et al. [183]), low and high to vesicles with diameters of 30 nm and 17 nm, respectively. Reprinted from Leonardini et al. [143], licensed under CC BY-NC 3.0.*

difference in the free energy minimum of the stalk state between the two NP sizes is further reduced. Figure 3.10e presents the results for curved membranes together with previously reported data for flat membranes [183]. These results show that increasing membrane curvature stabilizes the stalk relative to the pre-stalk state for both NP sizes, making the effect of the NP core size less critical in more highly curved vesicles. This is also due to the fact that smaller NPs promote the formation of a continuous lipid stalk in all cases of curvature, whereas larger NPs require increased membrane curvature to partially stabilize a lipid-mediated connection. In addition, cholesterol plays a key role particularly in the inner leaflet and in the vicinity of the NPs, since it preferentially accumulates in the inner leaflet and in the vicinity of the NPs in selected membrane regions, where it enhances the stability of the stalk [143].

3.5 Conclusions

Combining experimental and computational results, it has been shown that small AuNPs are more effective than larger AuNPs in mediating fusion between phosphatidylcholine vesicles. Lipid-mixing assays indicate that membrane lipid rearrangements occur in the presence of both small and large AuNPs. However, content mixing experiments show that the fusion process always proceeds to pore formation in the presence of small AuNPs, whereas large AuNPs promote fusion only in highly curved membranes. These findings are further supported by QCM experiments, which show that both NPs sizes are able to penetrate the lipid bilayer, and only systems containing small AuNPs exhibit stable vesicle-vesicle interactions. Computational results helped to elucidate the molecular mechanisms driving these interactions. The size of the NP core determines its curvature, which as a consequence regulates the conformational flexibility of the surface ligands [81, 183]. For this reason, the higher curvature of small NPs enables greater ligand flexibility, leading to the stabilization of a thicker stalk structure, in agreement with previous findings. In addition, the reduced steric bulk of smaller NPs allows the formation of a continuous hydrophobic bridge between opposing membranes. The extent of this hydrophobic connection increases with vesicle curvature and plays a crucial role in enabling the transition from the stalk intermediate to the hemifused state.

Overall, these results indicate that, by fine-tuning these physical determinants, AuNPs are a promising synthetic fusion machinery for the development of tailored drug delivery tools.

CHAPTER 4

Giant unilamellar vesicles doped with NPs

This chapter investigates the interaction between AuNPs and GUVs. I performed these experiments during a visiting research period in the group of Dr. Rumiana Dimova at the Max Planck Institute of Colloids and Interfaces in Potsdam, Germany. Conventional optical and confocal microscopy were employed to study membrane remodeling induced by NP embedding.

4.1 Introduction: NP-GUV interactions

GUVs are a robust and widely used membrane model system which provide an ideal platform for studying NP-membrane interactions under well-controlled conditions [37]. GUVs are cell-sized vesicles that enable the investigation of membrane responses to external perturbations (e.g., NP uptake) [189–192] and direct visualization of membrane remodeling phenomena (e.g., tubulation, budding, and shape transformations) [193], as well as the detection of membrane poration and leakage [194, 195]. Due to their size, GUV-based systems are highly compatible with optical microscopy techniques. These approaches allow real-time observation of membrane behavior and enable several properties to be probed in the same experiment. Furthermore, structural changes and dynamic processes can be studied at the single-vesicle level. Representative images of a GUV acquired using different optical techniques are shown in Figure 4.1.

To characterize the interactions between NPs and GUVs, several experimental approaches can be employed depending on the properties under investigation. To demonstrate NP insertion into membranes, Atukorale et al. [88] applied the colocalization approach. In these experiments, fluorescent NPs and labeled lipids are used to reveal the NP uptake into lipid membranes by visualizing regions in which the fluorescence of the NPs overlaps with that of

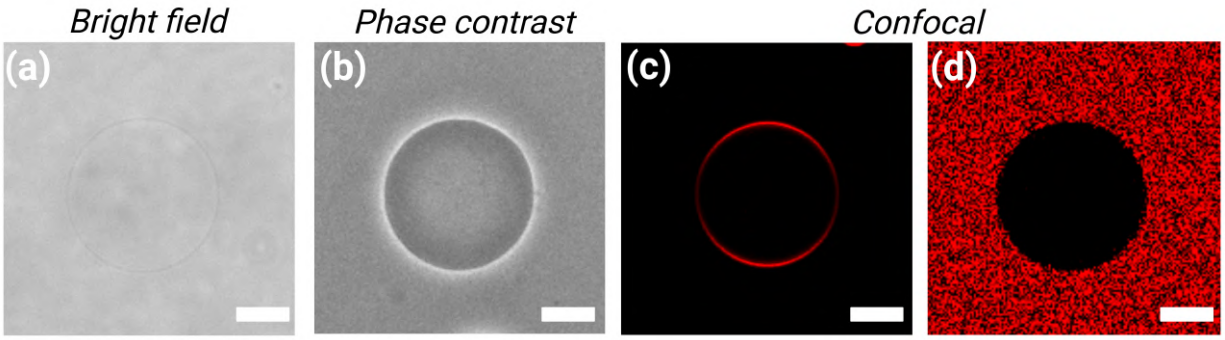

Figure 4.1 – ***Representative images of a GUV obtained using different optical techniques***. *In bright-field imaging* **(a)**, *the vesicle is difficult to observe due to its transparency in visible light. Vesicle visibility is enhanced in phase-contrast microscopy* **(b)** *due to refractive index differences between the vesicle interior and exterior. Images* **(c)** *and* **(d)** *show, respectively, a labeled vesicle membrane and a dark vesicle lumen in a fluorescent external medium, acquired using confocal fluorescence microscopy. Scale bars are* 25 µm.

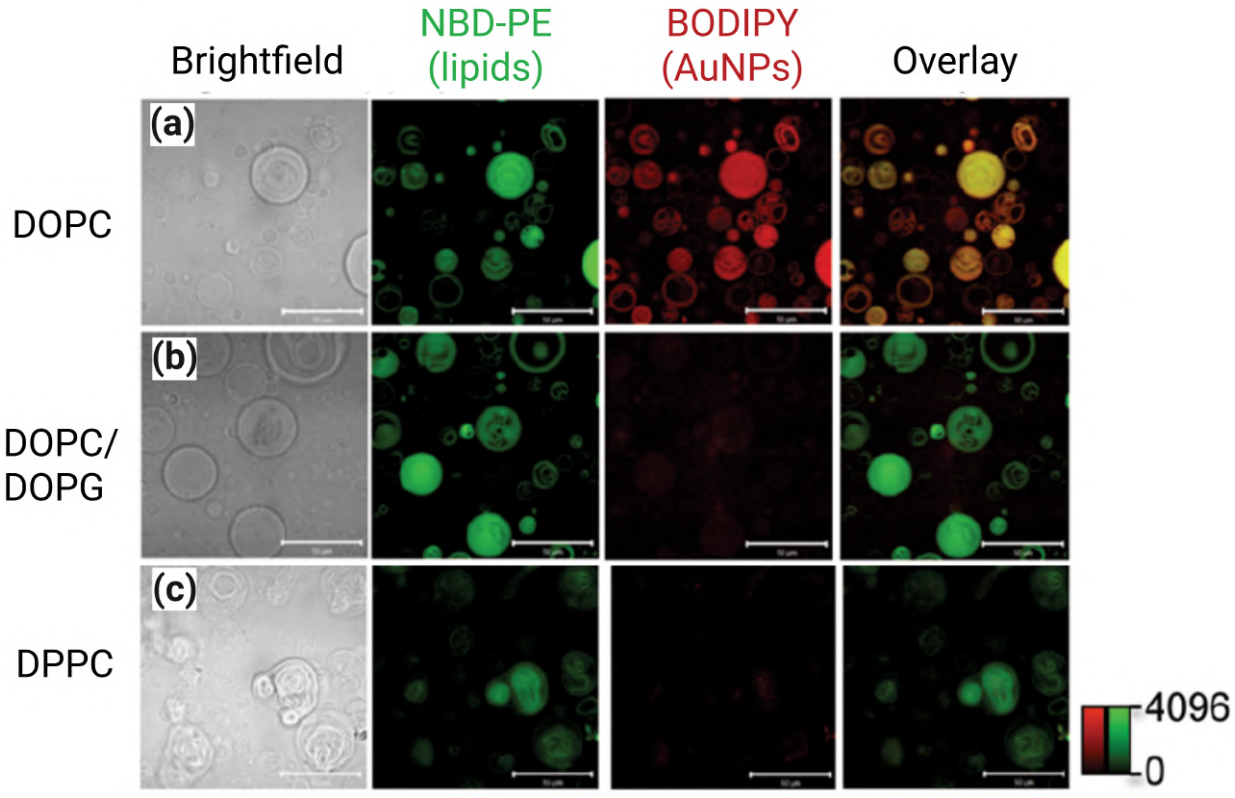

Figure 4.2 – ***Brightfield and confocal images of GMVs incubated with fluorescently labeled NPs.*** *BODIPY-labeled MUS:OT NPs (size range* $(2-3)$ nm*) incubated with NBD-PE-labeled GMVs are shown. In* **(a)**, *DOPC GMVs exhibit visible NP incorporation within the membrane. In* **(b)**, *80:20 DOPC:DOPG GMVs show no detectable NP incorporation in the membrane. In* **(c)**, *DPPC GMVs hinder NPs uptake due to the gel-phase nature of the membrane. Samples were incubated for* 1 h *at* 25 °C. *GMVs were prepared in* 50 mM *sucrose solution and diluted in* 50 mM *glucose solution. Scale bars are* 50 µm. *Reprinted with permission from Atukorale et al. [88]. Copyright (2018) American Chemical Society.*

the lipids and allowing a direct assessment of NP incorporation into the membrane [196–199].

These studies have revealed how membrane charge and phase influence interactions with amphiphilic NPs. In Figure 4.2, the interactions of MUS/OT BODIPY-labeled NPs with DOPC giant multilamellar vesicles (GMVs), DOPC/DOPG GMVs, and DPPC GMVs are compared. NPs are clearly embedded in zwitterionic fluid-phase DOPC GMV membranes, whereas they are excluded from anionc DOPC/DOPG membranes (Figure 4.2**a,b**). Atukorale et al. also showed that confocal imaging revealed a 4.9-fold lower BODIPY signal in DOPC/DOPG GMVs compared to DOPC GMVs. Furthermore, to assess the impact of membrane phase and fluidity on NP adsorption, BODIPY-labeled NPs were incubated with DPPC GMVs. The results showed that NP uptake is strongly inhibited in gel-phase DPPC GMVs, with no detectable BODIPY signal (Figure 4.2**c**). All GMVs were prepared in 50 mM sucrose and diluted in 50 mM glucose, the same solutions used in the experiments described in this chapter.

Other fluorescence-based techniques, such as Laurdan generalized polarization, can probe GUV membrane fluidity [200], and similarly fluorescence recovery after photobleaching (FRAP) can provide quantitative information on membrane lipid diffusivity [199]. In addition, particle-tracking approaches enable monitoring of NP dynamics on the membrane and their impact on overall membrane mobility [201, 202]. To gain further insight into membrane stability upon NP incubation, the mechanical properties of vesicles can be investigated, such as membrane tension and membrane curvature [203–205].

NP embedding can also influence vesicle morphology. The morphological changes can be analyzed by examining vesicle shape [194] and the presence of internal or external structures, including tubules, buds, and small vesicles [206, 207], thereby allowing the classification of vesicle structures. In addition to the mechanical and morphological aspects, membrane stability can also be evaluated by probing membrane integrity, in particular by assessing its permeability [195, 207]. This can be achieved by monitoring the permeation of molecules or fluorescent probes across the vesicle membrane, either outward or inward, depending on the leakage assay protocol employed. These techniques allow a detailed characterization of both the structural and functional changes in membranes, revealing how NPs specifically modulate GUV properties.

In this chapter, I employed DOPC GUVs and non-fluorescent 2:1 MUS:OT NPs. While many studies have focused on NP insertion into membranes, there is limited knowledge about the effects of NPs on GUV membrane morphology. To this end, fluorescence microscopy was used to visualize vesicle deformations upon NP incubation, with particular attention to the distribution of vesicle morphologies. In addition, membrane poration was monitored using a fluorescence-based assay and phase-contrast microscopy.

4.2 Materials and methods

4.2.1 GUVs preparation

GUVs composed of DOPC were prepared using the electroformation method [208]. Stock solutions of DOPC in chloroform were prepared at a concentration of 3 mM and stored at −20 °C. Fresh batches of GUVs were prepared prior to each experiment following a standard electroformation protocol. Electroformation was performed using two indium tin oxide (ITO)-coated glass plates (Präzisions Glas & Optik, Iserlohn, Germany). The plates were cleaned sequentially with pure water, ethanol, chloroform, ethanol and water prior to use. Subsequently, 10 µL of the lipid solution was evenly spread on each plate. The coated plates were then placed in a vacuum desiccator for at least one hour to allow complete evaporation of the chloroform. Once the solvent had fully evaporated, the two glass plates were assembled using a rectangular Teflon spacer to create the electroformation chamber. The chamber was then filled with 2 mL of an aqueous sucrose solution with an osmolarity of 50 mOsm/kg. The osmolarity was adjusted using a freezing-point osmometer (Gonotec Osmomat 3000, Berlin, Germany). Prior to use, the solution was filtered through 0.2 µm cellulose acetate membrane filters (Whatman PURADISC 30/0.2 CA).

Electroformation was performed by applying an alternating voltage of 1.6 V peak-to-peak at a frequency of 10 Hz. Following electroswelling, the vesicle suspension, with a final lipid concentration of 30 µM, was gently collected using a pipette and subsequently used in the experiments. Additional details regarding the electroformation procedure are provided in the Appendix A.

4.2.2 AuNPs characterization

Monodisperse AuNPs with a ligand ratio of 2:1 MUS:OT (68 mol % MUS and 32 mol % OT) and a gold core diameter of (3.2 ± 0.3) nm were employed. In contrast to Chapter 3, size-dependent effects are not the primary focus of this study; therefore, an intermediate NP diameter was selected. The NPs were synthesized using the same protocol as that employed in Chapter 3. See Appendix B for further details on the synthesis of AuNPs. Figure 4.3 shows TEM images of the AuNP cores immediately after synthesis, and the corresponding histograms of the core size distributions. AuNPs were characterized by TEM and ^{1}H-NMR to determine the core size and the ligand ratio after the synthesis. AuNP suspensions were prepared in Milli-Q ultrapure water at concentrations of 1.6 mg mL^{-1}. Before all experiments, AuNPs were sonicated in an ultrasonic bath for a few minutes. In general, these AuNPs exhibited remarkable long-term colloidal stability in water, and their dispersions did not require further manipulation before use. The molecular weight of the small NPs was calculated to be 151 163 g mol^{-1} (see Appendix C for the calculation). DLS and zeta potential measurements were performed prior to all experiments involving lipid

vesicles with a Zetasizer Nano ZS (Malvern Panalytical, UK). DLS measurements were performed to evaluate the hydrodynamic diameter both in water and in the external glucose solution. In addition, zeta potential measurements indicated that the NPs exhibit good colloidal stability in both solutions. All the data are summarized in Table 4.1.

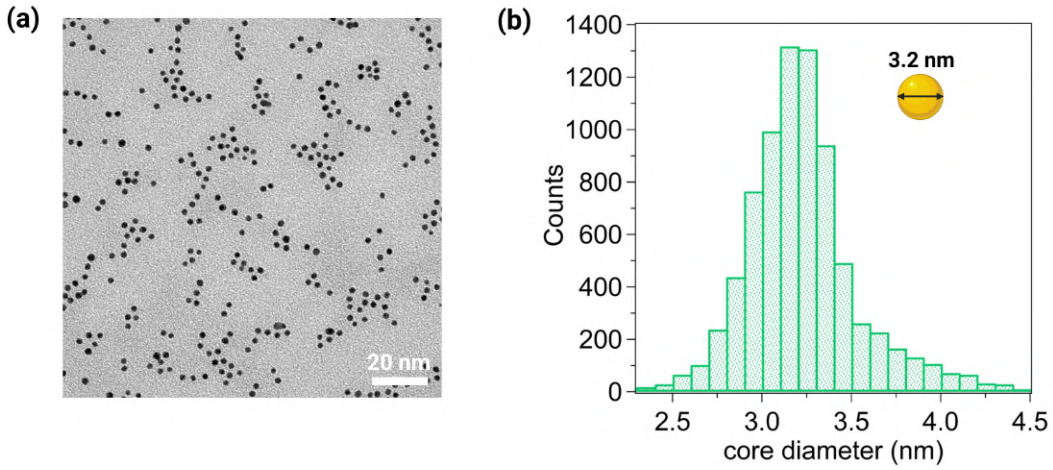

Figure 4.3 – **(a)** *Bright-field TEM image of monodisperse 2:1 MUS:OT AuNPs, with gold core diameters of* (3.2 ± 0.3) nm. **(b)** *Distributions of the gold core diameter.*

Table 4.1 – *AuNPs were characterized after synthesis by TEM and* ^{1}*H-NMR, and before each experiment to assess their size (DLS) and colloidal stability (ζ-potential).*

TEM[a]	^{1}H-NMR[b]	DLS – hydrodynamic diameter (nm)[c]		ζ-potential (mV)[d]	
core diameter (nm)	OT mol %	water	ext. sol.	water	ext. sol.
3.2 ± 0.3	32 ± 5	7.2 ± 1.7	10.8 ± 1.1	-47 ± 3	-43 ± 6

[a] *mean ± one standard deviation.*
[b] *mean ± error calculated using Student's statistics (95 % confidence level,* $N = 3$*).*
[c] *mean ± error calculated using Student's statistics (95 % confidence level, at least* $N = 12$*).*
[d] *mean ± error calculated using Student's statistics (95 % confidence level, at least* $N = 6$*).*

4.2.3 In-bulk experiments

Two sets of experiments were performed to investigate the morphology and permeability of GUVs. GUVs prepared in sucrose solutions were diluted 1:4 in isotonic glucose solutions (50 mOsm/kg). Prior to GUV deposition, glass slides were passivated with Bovine Serum Albumin (BSA) (10 µL from a 2 mg mL^{-1} batch was spread on the slide and left for 20 min at room temperature) and subsequently rinsed with Milli-Q ultrapure water. For experiments with NPs, glucose solutions containing 0.02 mg mL^{-1} NPs were prepared, at 50 mOsm/kg. In all cases, imaging was performed after 15 min of incubation at room temperature. For membrane morphology studies, DOPC GUVs were labeled with 0.5 % Rhod-PE and incubated

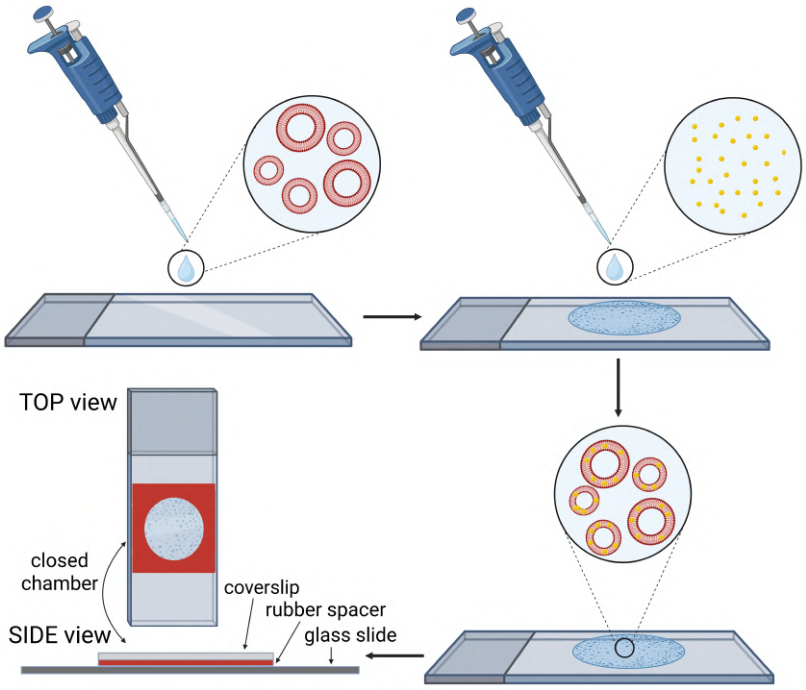

Figure 4.4 – ***Experimental setup for NP-induced pertubation of GUV morphology.*** *Rhod-PE-labeled GUVs were deposited on BSA-passivated glass slides and incubated in isotonic glucose solutions, with or without NPs. Sealing with a Teflon spacer and a coverslip formed a closed chamber, ensuring osmotic equilibrium and enabling controlled membrane-NP interactions under bulk conditions for GUV morphology analysis.*

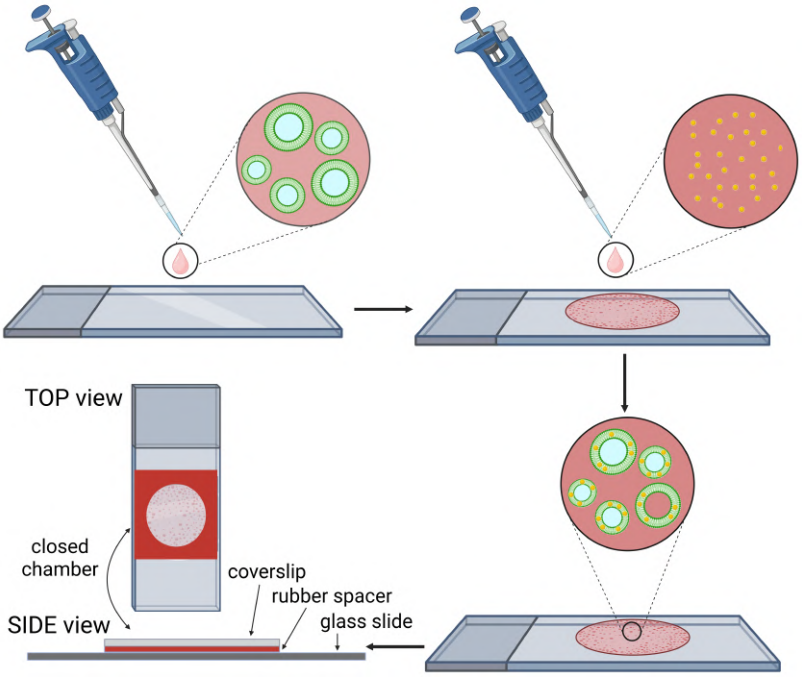

Figure 4.5 – ***Experimental setup for NP-induced pertubation of GUV permeability.*** *NBD-PE-labeled GUVs dispersed in SRB-glucose solutions were deposited on BSA-passivated glass slides and incubated in isotonic solutions, with or without NPs. After sealing, a closed chamber was formed, ensuring osmotic equilibrium and enabling controlled membrane-NP interactions under bulk conditions to evaluate SRB permeability into the vesicles.*

in glucose solutions (with or without NPs) under osmotic equilibrium in a closed chamber (Figure 4.4).

For permeability measurements, DOPC GUVs were labeled with 0.5 % NBD-PE and incubated in glucose solutions containing 2.5 µM SRB (with or without NPs) under osmotic equilibrium in a closed chamber (Figure 4.5). In both cases, the final lipid concentration on the glass slide was 7.5 µM, while the final NP concentration was 0.11 µM. The corresponding lipid-to-nanoparticle molar ratio was therefore $R = \frac{\text{mol lipids}}{\text{mol NPs}} \approx 70$.

4.2.4 Confocal microscopy

GUVs were observed using a confocal laser scanning microscope (Leica Microsystems SP8, LIA Compact Supply Unit, Wetzlar, Germany). For GUVs fluorescently labeled with 0.5 mol % Rhod-PE, images were acquired using an HC PL FLUOTAR L 20× dry objective (NA 0.40) equipped with phase-contrast illumination, and an HC PL APO CS2 63× oil immersion objective (NA 1.40) for higher-magnification imaging. Fluorescence excitation was provided by a solid-state laser at $\lambda = 552$ nm, and emission was collected in the $(562 - 630)$ nm spectral window using a hybrid HyD detector. Simultaneously, transmitted-light images were recorded using a photomultiplier tube (PMT) detector. For permeability experiments, GUV images were acquired using an HC PL FLUOTAR L 20× dry objective (NA 0.40) equipped with phase-contrast illumination. GUVs labeled with 0.5 mol % NBD-PE were excited using a solid-state laser at $\lambda = 488$ nm. The external solution containing SRB was excited at the same wavelength. Fluorescence emission was collected in the $(498 - 550)$ nm spectral window using a PMT detector. To minimize spectral cross-talk between the NBD-PE and SRB fluorescence channels, signals were acquired in sequential scanning mode. Simultaneously, phase-contrast images were recorded using a PMT detector. Each measurement returned an output consisting of 3 channels (NBD-PE, SRB, and transmitted light), in which the signal was collected in the sequential mode. For each acquisition, z-stacks were collected with a step size of approximately ≈ 0.5 µm, and images were acquired at a resolution of 512×512 pixels. All the images were analyzed using LAS X Office software (v. 1.4.7.28982).

4.3 Results and discussion

Using Rhod-PE-labeled fluorescent vesicles, I was able to observe and evaluate GUV morphology variations before and after NP incubation. Vesicles were analyzed individually from the acquired images and classified according to their shape and membrane structure. Since some membrane structures can arise intrinsically during the GUV preparation process [209, 210], a systematic morphological analysis is necessary. To ensure reproducibility, a total of at least 400 vesicles were analyzed from three different vesicle batches, acquiring at least 15 images per batch, each corresponding to a distinct region of the chamber. In addition, vesicle

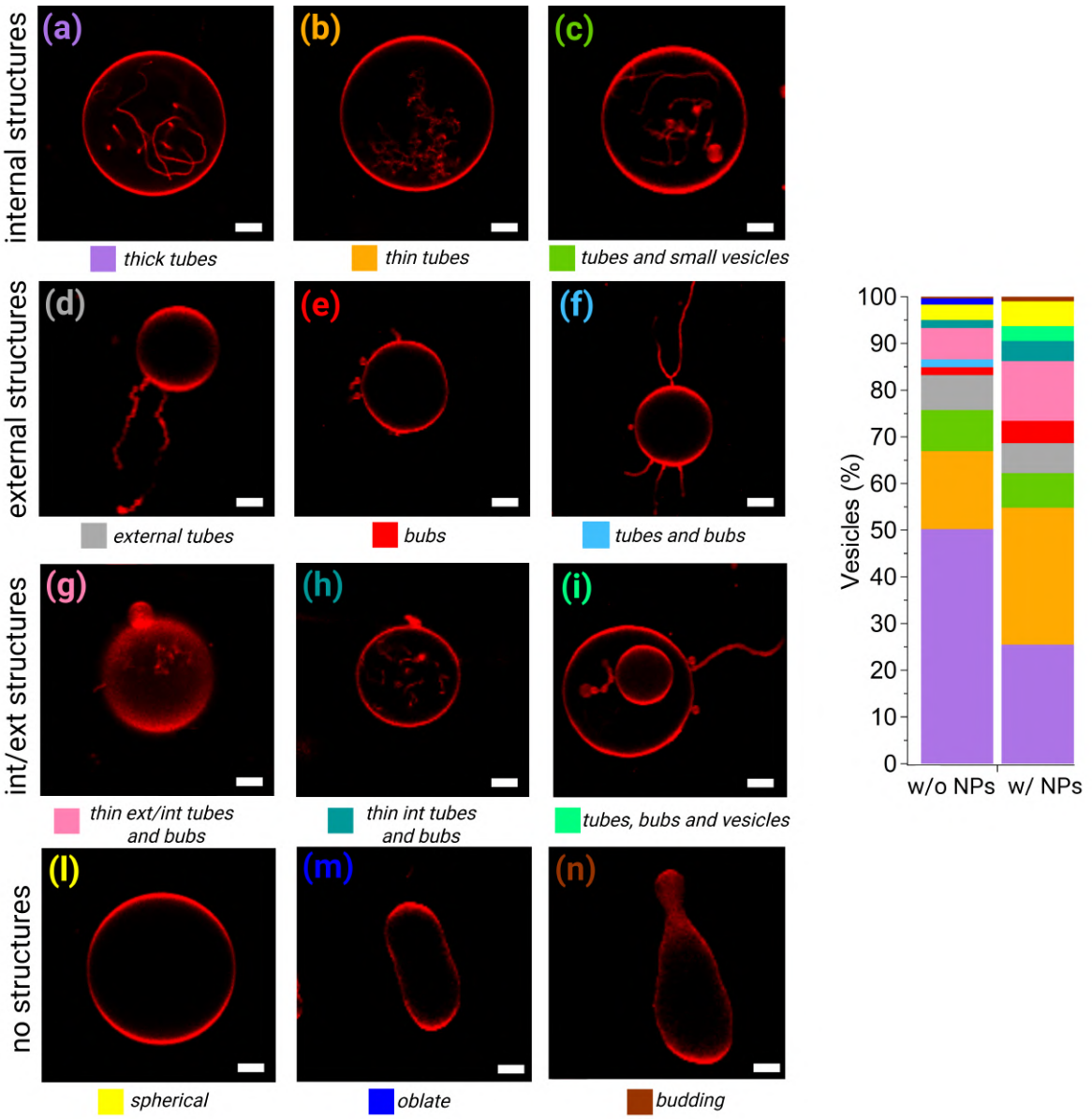

Figure 4.6 – *Representative confocal cross sections of DOPC GUVs showing the various vesicle morphologies observed in the absence and presence of NPs. Images* **(a-c)** *show vesicles exhibiting internal membrane structures, characterized by the presence of thick tubes* (a)*, thin tubes* (b)*, and a combination of tubes and small vesicles* (c)*, all confined within the vesicle lumen. Image* **(d-f)** *show vesicles with external membrane structures, including membrane tubes* (d)*, buds* (e)*, and a combination of tubes and buds* (f)*. Images* **(g-i)** *show vesicles presenting both internal and external (int/ext) structures, such as thin ext/int tubes and bubs* (g)*, int tubules and buds* (h)*, buds* (i)*. Images* **(l-n)** *report vesicles with no visible membrane structures, exhibiting spherical* (l)*, oblate* (m)*, and budding* (n) *shapes. The bar plot on the right shows the percentage distribution of vesicles of each morphology in the absence of NPs (w/o NPs, number of total vesicles analyzed = 239) and in the presence of NPs (w/ NPs, number of total vesicles analyzed = 188). The colors in the bar plot correspond to the vesicles structures illustrated in the representative images. Scale bars* 10 µm.

morphology was examined by acquiring fluorescence z-stacks, allowing reliable identification of membrane structures throughout the three-dimensional volume. Single-vesicle analysis revealed multiple populations of vesicles with distinct morphologies, which were grouped into four categories for the purpose of this study [193]:

- **internal membrane structures:** vesicles exhibiting tubes of varying thickness, as well as vesicles containing both tubes and small internal vesicles (Figure 4.6**a-c**)
- **external membrane structures:** vesicles displaying protrusions extending outward, including tubular extensions and small buds (Figure 4.6**d-f**)
- **combined internal and external structures:** vesicles with both internal and external tubes or buds (Figure 4.6**g-i**)
- **no membrane structures:** vesicles without distinct internal or external structures but exhibiting different shapes, including spherical, oblate, or budding conformations (Figure 4.6**l-n**)

The bar plot in Figure 4.6 summarizes the distribution of these morphologies, comparing control experiments without NPs to experiments with NPs.

To quantify the effect of NPs, a statistical analysis of the four categories was performed (Figure 4.7**a**). The presence of NPs is associated with a significant decrease in the fraction of vesicles displaying only internal structures, accompanied by a significant increase in those presenting both internal and external structures. The fractions of vesicles with only external structures or no visible structures remain similar under both conditions. These results are consistent with computational work by Lavagna et al. [211], showing that aggregates of semi-snorkeled NPs induce positive membrane curvature. Aggregate formation is supported by the experimental conditions, as NPs are known to embed in DOPC membranes at the sugar concentrations of this work [88], and the high NP-to-lipid ratio (1:70) further promotes aggregation. Therefore, the decrease in vesicles with only internal structures and the increase in vesicles exhibiting both internal and external structures are in accordance with an outward membrane deformation, as predicted by computational studies. Moreover, factors such as leaflet or buffer asymmetry conditions [193, 212], and interactions with external agents [213] (e.g., proteins or NPs) are known to influence the spontaneous curvature of lipid membranes. In the case of NP aggregates, the generation of excess membrane area may lead to lipid redistribution and the formation of more complex membrane morphologies.

In addition to the structural characterization of the GUVs, the diameter of each vesicle was measured whenever possible, i.e., for spherical vesicles with and without membrane structures. Figure 4.7**b** shows the size distribution. In both the absence and presence of NPs, vesicle diameters display comparable values, with similar medians and interquartile ranges. No substantial differences in size dispersion are observed between the two conditions, indicating that NP incorporation does not significantly affect GUV size.

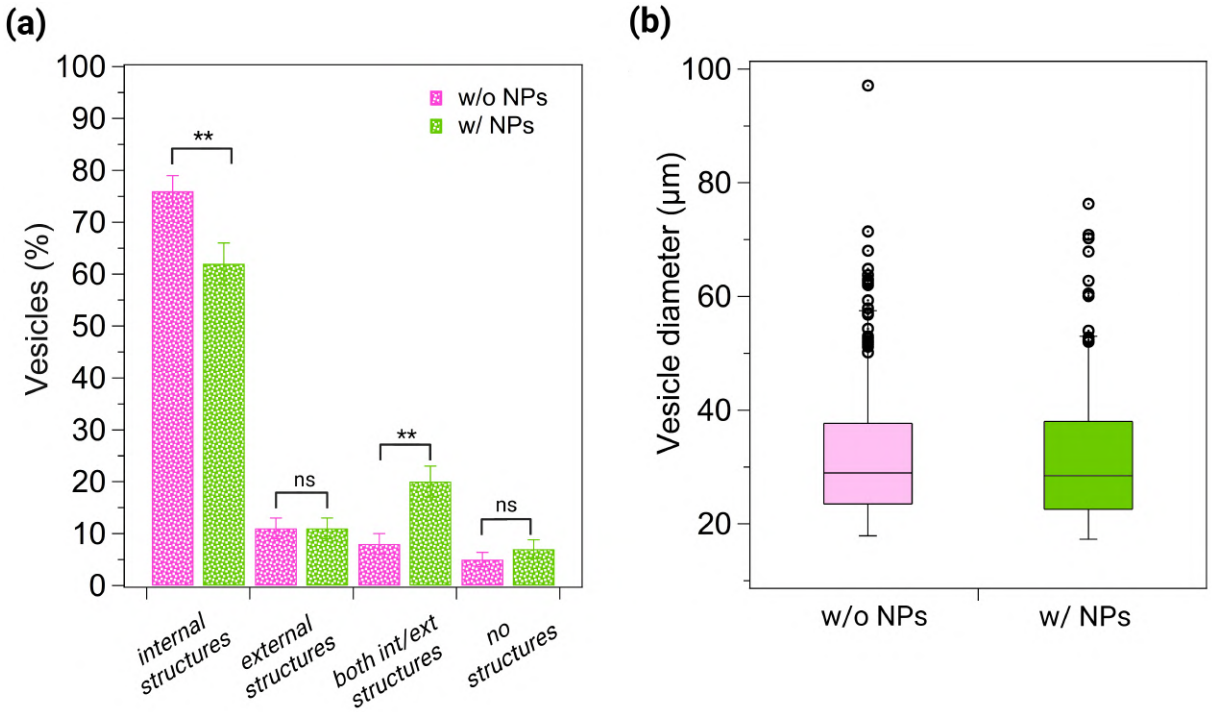

Figure 4.7 – **(a)** *Percentage distribution of vesicles according to their morphology (internal structures, external structures, both internal and external structures, and no structures) in the absence and in the presence of NPs. Error bars represent standard errors calculated from discrete vesicle counts. The statistical analysis was performed using t-test ($p < 0.01^{**}$, ns = non-significant).* **(b)** *Distribution of GUV diameters analyzed in the absence (w/o NPs) and in the presence (w/ NPs) of NPs. Vesicles with diameters smaller than* 15 µm *were excluded from the analysis due to difficulties in resolving internal structures. Box plots: the central line indicates the median; the box spans from the first quartile (Q1, 25th percentile) to the third quartile (Q3, 75th percentile); whiskers represent the lowest and highest values within 1.5 times the interquartile range; data points beyond the whiskers are shown as outliers. 230 vesicles without NPs and 176 vesicles with NPs were used to calculate the diameter.*

Further insights into NP-membrane interactions were obtained through phase-contrast microscopy and fluorescence leakage investigations. Membrane permeability was assessed by detecting NP-induced pore formation in the GUVs via leakage of the fluorescent dye SRB present in the external solution. In addition to the fluorescence from the external medium, vesicle membranes were labeled with a fluorescent lipid to enable their identification in the case of membrane permeabilization. As shown in Figure 4.8, when the membrane remains intact, the vesicle lumen appears dark, allowing the vesicle to be easily recognized. If the membrane becomes permeabilized and SRB enters the lumen, vesicles can no longer be identified based solely on the images in Figure 4.8**b,e**. In these samples, in all acquisitions on two independent GUVs samples, no membrane permeation was observed, either in the presence or absence of NPs, even after one hour of incubation.

In parallel, phase-contrast imaging was performed on all vesicles. In all cases, consistent with the fluorescence assay, the phase-contrast signal was preserved, indicating intact

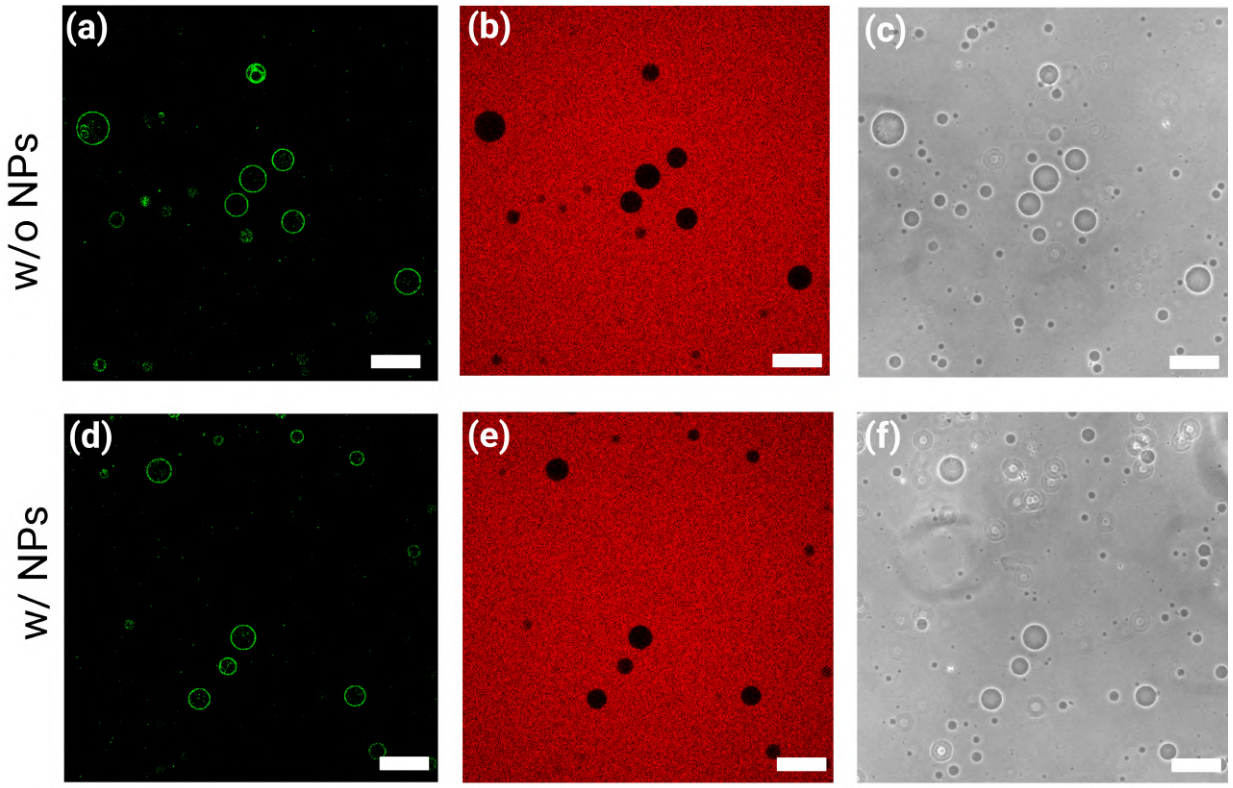

Figure 4.8 – *Representative images of GUV permeability experiments. Vesicles labeled with NPD-PE* **(a, d)** *are dispersed in an external medium containing SRB and their lumens appear dark when no permeation occurs* **(b, e)**. *The phase-contrast image* **(c, f)** *confirms that there is no sucrose and glucose mixing, indicating that no pores are formed in the membrane. No membrane permeation was observed, either in the presence or absence of NPs. Scale bars* 50 µm.

membranes. This observation confirms the absence of mixing between the internal sucrose solution and the external glucose solution. These results demonstrate that the observed morphological changes upon NP incubation are not associated with membrane rupture or loss of vesicle integrity. This also supported by the invariance of the mean GUV size in both the presence and absence of NPs. Moreover, these findings are consistent with previous observations obtained from calcein leakage assays using LUVs [14] and GMVs [81], where amphiphilic AuNPs were shown to insert into lipid membranes without inducing leakage.

4.4 Conclusions

In this work, I investigated the effect of NP uptake on the size distribution, morphology and permeability of GUVs as minimal lipid model for the cellular membrane system. By combining systematic morphological analysis with size characterization, I showed that the presence of NPs does not significantly affect the vesicle diameter distribution. Instead, NPs addition leads to a redistribution of vesicle morphologies, promoting the increase of the configurations characterized by the coexistence of internal and external structures, and

decrease of those showing only internal defects.

Membrane integrity was further assessed through permeability experiments. Analysis of vesicles revealed no SRB permeation in the vesicles or mixing of sucrose and glucose, neither immediately after NPs exposure nor over time, demonstrating that NP-membrane interactions do not induce membrane permeabilization under the conditions investigated. Together, these results indicate that NPs can induce morphological remodeling of lipid membranes without compromising their barrier function providing insight into NP-membrane interactions with potential implications for NPs design and biomimetic membrane studies.

CHAPTER 5

NP effect on membrane permeability under osmotic stress

This chapter presents SAXS measurements carried out to investigate the role of AuNPs in affecting membrane permeability. The experiments were performed at the Italian Institute of Technology (IIT) in collaboration with Dr. Silvia Dante (Materials Characterization Facility, IIT, Morego, Genoa).

5.1 Introduction

Membrane permeability is a key property of biological systems, as it governs the selective transport of water, ions, and small solutes across the lipid bilayer [214]. This process plays a central role in a wide range of biological phenomena, including volume regulation, signal transduction, and the maintenance of electrochemical gradients [215]. In particular, membrane permeability is crucial in the cellular response to osmotic stress. For example, in red blood cells and epithelial tissues, the ability of the membrane to dynamically respond to osmotic gradients is essential to prevent cell damage and preserve functional integrity. Similarly, in bacteria, low external osmotic pressure leads to the development of turgor pressure, which compensate for excessive water influx into the cell [216]. More generally, both eukaryotic and prokaryotic cells can grow under high osmotic pressures, typically in the range of 7 to 10 atm [217]. Therefore, even small variations in membrane permeability can have significant consequences for cellular behavior and physiological functions.

Biomimetic vesicles, such as unilamellar lipid vesicles, have been extensively used to study membrane permeability [218–223], as they mimic key aspects of cellular osmotic behavior [224–226]. In particular, they actually behave as osmometers, with vesicle swelling or shrinking due to water flux between the vesicle interior and exterior in response to a solute gradient.

The relation between solute concentration gradients and osmotic pressure is described by the van 't Hoff equation. The difference in osmotic pressure, $\Delta\pi$, is typically expressed in terms of the difference in solute concentration, Δc, as $\Delta\pi = k_B T \Delta c$, where k_B is the Boltzmann constant and T is the absolute temperature.

In general, factors influencing membrane permeability include lipid bilayer properties such as tail saturation, headgroup interactions, and the presence of membrane proteins, which actively regulate water and ion fluxes [227]. Under osmotic stress, membrane tension can induce transient nanoscale defects, enhancing water transport [228]. Variations in water transport across membranes can also result from external agents that disrupt permeability mechanisms.

Several studies have explored such effects, particularly in the context of nanomedicine and nano-bio interactions. In particular, molecular dynamics simulations showed that AuNPs can alter membrane water permeability by increasing local disorder and lipid fluctuations [229, 230], or by modifying membrane elasticity and promoting transient defect formation [75].

In this study, I used SAXS to investigate how amphiphilic AuNPs influence the permeability of small unilamellar vesicles under osmotic stress induced by sugar concentration gradients.

5.2 Materials and methods

5.2.1 Vesicle preparation

MLVs of DOPC were prepared at a lipid concentration of $10\,\mathrm{mg\,mL^{-1}}$ by hydrating a dry lipid film with a 50 mM sucrose solution, the same as that used for the GUVs described in Chapter 4. This lipid concentration was chosen to ensure a sufficiently high final lipid content for SAXS measurements. The suspension was subsequently sonicated for 15 min at room temperature. SUVs were produced by sequential extrusion through membranes with decreasing pore sizes (0.1 µm, 0.05 µm, and 0.03 µm), performing 31 extrusions through each membrane. See Appendix A for further details on extrusion method. The vesicle batches were stored at 4 °C until use.

The hydrodynamic diameter of the DOPC SUVs was measured in the aqueous sucrose solution before experiments using DLS. An average diameter of (62.8±0.2) nm (Z-average) was obtained (mean value and standard deviation were calculated from $N = 12$ measurements).

5.2.2 SAXS experiments

SAXS experiments were performed using a Malvern PANalytical Empyrean third-generation multipurpose platform operating in transmission geometry. Cu Kα radiation ($\lambda = 1.54$ Å) was used (40 kV, 45 mA). 1D-SAXS measurements were carried out in a vacuum-path chamber (Scatter X[78]) using a beam with line collimation and a GaliPIX^{3D} detector. Scans

were performed in the scattering vector range $q = (0.1 - 3.5)\,\mathrm{nm}^{-1}$ with a step size of 0.35°, and an exposure time of 30 min. The chosen q-range was selected to ensure reliable measurements with the instrument used in this work, as the signal-to-noise ratio decreases at higher q values due to increasing background contributions. Quartz capillaries (Hilgenberg, Germany) with a diameter of 1 mm and a volume of approximately 100 µL were used as sample holders.

Sample preparation. Vesicles containing 50 mM sucrose were diluted in external solutions at different sucrose concentrations in order to obtain controlled osmotic conditions. 100 µL of vesicle suspension (lipid concentration $10\,\mathrm{mg\,mL}^{-1}$) were diluted with:

- 100 µL of ultrapure Milli-Q water, resulting in an external sucrose concentration of 25 mM (hypotonic osmotic gradient);
- 100 µL of a 50 mM sucrose solution, resulting in equal internal and external sucrose concentrations (isotonic osmotic gradient);
- 100 µL of a 100 mM sucrose solution, resulting in an external sucrose concentration of 75 mM (hypertonic osmotic gradient).

In all cases, the final lipid concentration was $5\,\mathrm{mg\,mL}^{-1}$, and the osmotic difference for both hypotonic and hypertonic solutions was $\Delta c = 25\,\mathrm{mM}$.

For the experiments with NPs, the same NP type used in Chapter 4 was employed, namely 2:1 MUS:OT amphiphilic AuNPs with a negative charge. The vesicle-NP solutions were prepared by adding 22 µL of NPs from a stock solution of $5.6\,\mathrm{mg\,mL}^{-1}$ to achieve a lipid/NP molar ratio of $R = 1590$, corresponding to approximately 16 NPs per vesicle. The NPs were then incubated with the vesicles overnight prior to the experiments.

Background measurements of aqueous solutions at different sucrose concentration were performed using the same capillary employed for the vesicles or vesicles incubated with NPs dispersions in order to ensure consistent subtraction of solvent scattering. SUVs were chosen to meet the instrument requirements for resolution at low scattering angles.

Data analysis. Data analysis was carried out using the *EasySAXS* software package (Malvern PANalytical). The software performs the primary data processing steps, including absorption correction, background subtraction, and conversion of the scattering angle 2θ into the scattering vector $\vec{q}$. After background subtraction, the experimental curves were fitted using a spherical shape with radius r and a concentric core-shell structure consisting of three shells: the inner and outer lipid headgroup regions and the hydrophobic bilayer core (Figure 5.3**a**). A fitting step-function model was used, in which the electron density is described as a constant profile across the different radial regions. The scattering intensity is

obtained as the squared modulus of the scattering amplitude, which is given by the sum of the contributions from the individual layers:

$$I(q) = \left| \sum_{i=1}^{3} \Delta\rho_i \, V(R_i) \, F(q, R_i) \right|^2 \tag{5.1}$$

where $\Delta\rho_i$ represents the electron density contrast of each shell, $V(R_i)$ is the volume of a sphere of radius R_i, and $F(q, R_i)$ is the spherical form factor. Each shell is described by three parameters: thickness t, electron density contrast ρ, and polydispersity. The core contrast was set to zero, as the core material (e.g., the vesicle lumen) is the same as the medium surrounding the vesiscles. The contrast of each shell is defined relative to the core.

As a control, SAXS measurements of the NP solution were performed to determine the NP volume distribution. The NP radius was determined using an indirect transform technique implemented in the software. In this method, the experimental SAXS intensity is related to the particle volume distribution function, through a regularization procedure, allowing reconstruction of the NP size distribution from the measured scattering data. The resulting NP radius was (1.6 ± 0.4) nm, consistent with values obtained by TEM (Table 4.1).

5.3 Results and discussion

In these osmotic stress experiments, a sucrose concentration gradient of $\Delta c = 25\,\text{mM}$ (corresponding to approximately $\Delta\pi = 0.6\,\text{atm}$) was imposed between the interior and exterior of the vesicles. Gradients of this magnitude are commonly employed in studies of model membranes to investigate vesicle osmotic responses. Previous works on both LUVs [231, 232] and GUVs [224–226, 233] have shown that even relatively modest osmotic gradients can induce measurable changes in vesicle volume and shape through water flux across the lipid bilayer. In this framework, only water transport across the membrane is considered. Although osmotic gradients generate a driving force for both water and sucrose diffusion across the membrane, depending on the relative concentrations, the permeability of the lipid bilayer to water is approximately six orders of magnitude higher than that to sugars [234–236]. As a result, water flux represents the kinetically dominant process governing the vesicle response.

As a control, DLS measurements were performed prior to the SAXS experiments to ensure that the applied osmotic stress did not cause vesicle disruption. While DLS cannot resolve small changes in vesicle size, it can be used to assess the presence of intact vesicles. Measurements were carried out for vesicles both in the absence and presence of NPs under the same osmotic conditions used for the SAXS experiments. The number distributions indicate that the vesicles remain intact under both hypotonic and hypertonic conditions. In samples containing NPs, the contribution of NPs to the DLS signal is negligible, as scattering

is dominated by the vesicles due to their larger size (Figure 5.1).

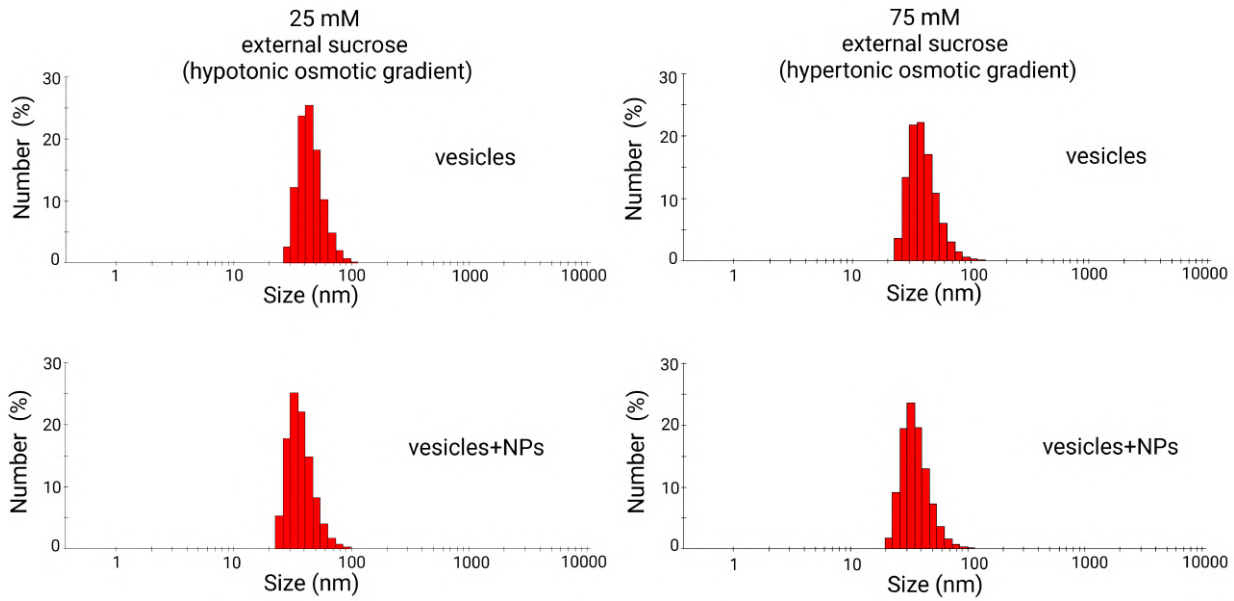

Figure 5.1 – *Representative DLS number size distributions of a sample without NPs and of a sample with NPs, measured under the same conditions as in SAXS experiments. Vesicles remain intact under both hypotonic and hypertonic conditions, indicating that the applied osmotic stress does not induce disruption. The NP contribution is not clearly visible, as the scattering signal is dominated by the vesicles. Internal sucrose concentration* 50 mM.

In Figure 5.2, the SAXS intensities and the corresponding fitted curves (shown as continuous lines) from the three experiments under different osmotic conditions are reported. The parameters obtained from the best fits are summarized in Table 5.1.

Table 5.1 – *Structural parameters obtained from the fitting procedure for the three layers of the spherical core-shell model (t is the layer thickness and ρ the electron density). S1, S2, and S3 represent shell 1, shell 2, and shell 3, respectively.*

		25 mM sucrose		50 mM sucrose		75 mM sucrose	
		ρ (a.u.)	t (nm)	ρ (a.u.)	t (nm)	ρ (a.u.)	t (nm)
Ves	S1	0.90	0.90	1.10	0.72	0.90	0.90
	S2	−0.50	2.40	−0.50	2.40	−0.50	2.40
	S3	0.30	1.27	0.30	1.27	0.40	1.20
Ves+NPs	S1	1.30	1.62	1.30	1.55	1.30	1.62
	S2	−0.50	2.31	−0.50	2.20	−0.50	2.47
	S3	0.90	0.26	1.40	0.90	1.00	0.26

From these fits, the vesicle radius and bilayer thickness were determined as a function of the osmotic gradient (Figure 5.3). Under iso-osmotic conditions, the vesicle radius is approximately ≈ 30 nm, in good agreement with values obtained from DLS measurements. Under hypotonic conditions, the vesicle radius increases (≈ 35 nm), corresponding to vesicle swelling due to water influx. Conversely, under hypertonic conditions, the radius decreases

(≈ 25 nm), corresponding to vesicle shrinking due to water efflux. In both cases, the vesicle radius changes by about ≈ 5 nm.

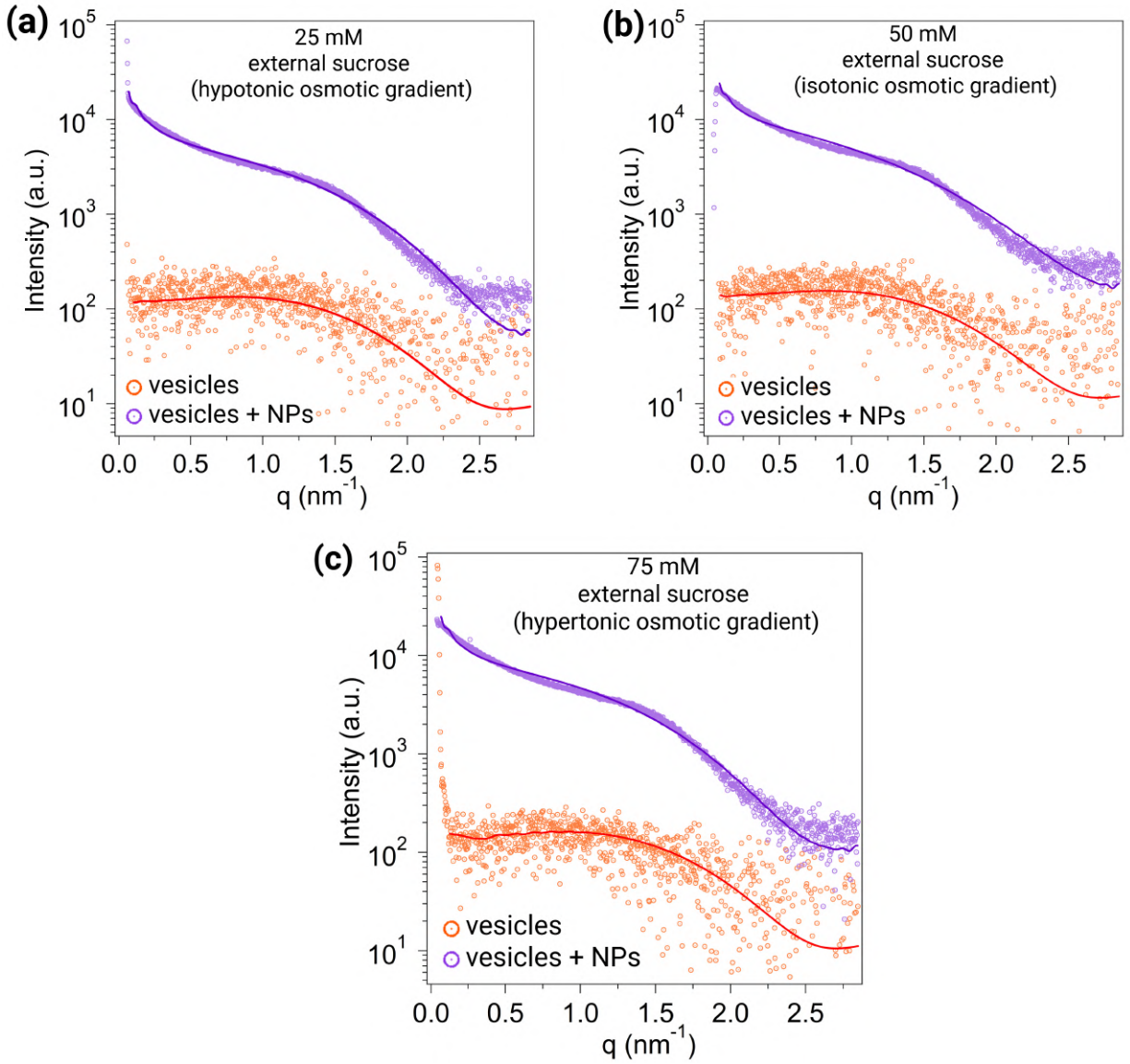

Figure 5.2 – *SAXS experimental curves and corresponding fitted curves obtained from DOPC SUVs containing* 50 mM *sucrose under hypotonic conditions (*25 mM *external sucrose)* **(a)**, *isotonic conditions (*50 mM *external sucrose)* **(b)**, *hypertonic conditions (*75 mM *external sucrose)* **(c)**, *in the presence or absence of NPs. The continuous lines represent the fitted curves. Internal sucrose concentration* 50 mM.

This behavior of the vesicles is consistent with observations reported for SUVs and LUVs in previous studies [231, 232, 237].

For the NP-vesicle system, the scattering curves were analyzed under the assumption that, at the ratio used in this work (vesicles:NPs 1:16), all NPs are incorporated into the membrane [87, 91, 143]. This ratio was chosen to ensure that a sufficient number of NPs are embedded in the membrane to observe their effect, which may also be influenced by possible NP aggregation.

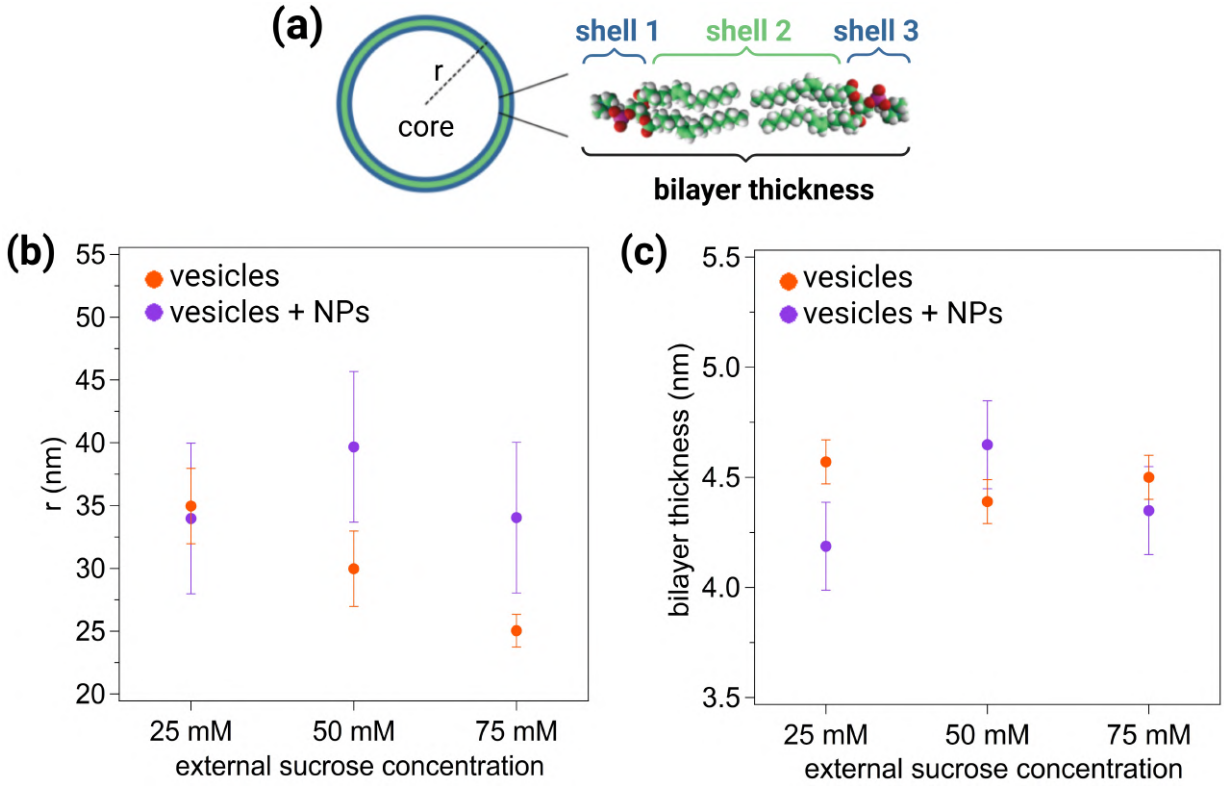

Figure 5.3 – **(a)** *Spherical model employed in the SAXS fitting. A sphere of radius r surrounded by a three-layer shell, representing the distinct regions of the lipid bilayer, was used.* **(b)** *Vesicle radius obtained from the fitting procedure at different external sucrose concentrations, in the presence or absence of NPs.* **(c)** *Bilayer thickness resulting from the fitting procedure under the same conditions. The total thickness was calculated as the sum of the thicknesses of the three shells. Internal sucrose concentration* 50 mM. *Error bars were calculated using the percentage polydispersity obtained from the fitting procedure.*

Under these conditions, the fitted curves yielded a vesicle radius of approximately ≈ 40 nm in the isotonic solution. Under hypertonic conditions, the radius slightly decreases to ≈ 34 nm, and a similar value is observed under hypotonic conditions. Therefore, the NP-vesicle system does not follow the same trend observed for bare vesicles. This behavior could be attributed to an overall stabilization of the membrane, which modifies its tension. Under hypotonic stress, the presence of NPs could reduce membrane tension, thereby limiting the increase in distance between neighboring lipids and suppressing the effects of vesicle swelling. Under hypertonic conditions, the NPs could modulate membrane compression, preventing the vesicles from reaching their maximum shrinkage [238–240].

In both cases, the bilayer thickness is in the range of $(4-5)$ nm, consistent with typical lipid bilayer thickness values. In the presence of NPs, a slight thinning of the bilayer is observed under out-of-equilibrium conditions, likely due to osmotic stress-induced rearrangements within the bilayer. However, due to the low signal-to-noise ratio in the high-q region, it is not possible to draw conclusions about possible internal membrane reorganization.

5.4 Conclusions

In this work, amphiphilic AuNPs were used to investigate how vesicle responses to osmotic stress are affected by the NPs. SAXS experiments allowed the quantification of changes in vesicle size under different osmotic conditions. The results show that the NP-vesicle system behaves differently from bare vesicles. For bare vesicles, the observed trends are consistent with previously reported results [231, 232, 237], with vesicle swelling under hypotonic conditions and shrinkage under hypertonic conditions. In contrast, the presence of NPs appears to limit these osmotic responses, reducing both swelling and shrinking. This behavior can be attributed to the influence of NPs on membrane properties, resulting in modulation of membrane tension and limiting the expansion or compression of the bilayer. Overall, these findings demonstrate that embedding NPs into lipid membranes can significantly alter vesicle structural responses to osmotic stress. Further experiments, such as the use of fluorescence-based techniques, could provide additional insights into the underlying mechanisms [226, 241, 242].

CHAPTER 6

Asymmetric lipid membranes: towards more biomimetic models

This chapter presents a protocol that was developed for the preparation of asymmetric lipid vesicles using cyclodextrin-mediated lipid exchange. The method exploits lipid exchange between the outer leaflets of preformed vesicles to obtain membrane asymmetry. In this work, this approach is used to produce vesicles enriched in negatively charged lipids in the inner leaflet. In addition, a preliminary assessment of the lipid exchange efficiency was performed by zeta potential measurements on the obtained asymmetric vesicles.

6.1 Introduction

Membrane asymmetry is an intrinsic characteristic of cell membranes and consists of the non-uniform distribution of lipid species between the two leaflets of the bilayer (Figure 6.1**a**). This feature is crucial for maintaining both membrane structure and the functional organization of the cell [243, 244]. In particular, asymmetry regulates membrane curvature and stability, bilayer fluidity and thickness, and contributes to the formation of lipid microdomains (or rafts) [245–247]. In addition, the chemical composition and the charge of each leaflet finely regulate and tune membrane mechanics, electrostatics, and protein-lipid interactions [248–252].

Biological processes in which membrane asymmetry plays a key role include vesicle trafficking and signaling [254], regulation of membrane protein activity [255] and apoptosis [256, 257]. Disruption of lipid asymmetry can have significant pathological consequences. For example, phosphatidylserine (PS), which is normally more abundant in the inner leaflet of the plasma membranes of eukaryotic cells, becomes more exposed on the outer leaflet when asymmetry is lost, and this redistribution has been associated with various pathological conditions. PS externalization occurs irreversibly during apoptosis, and transiently during

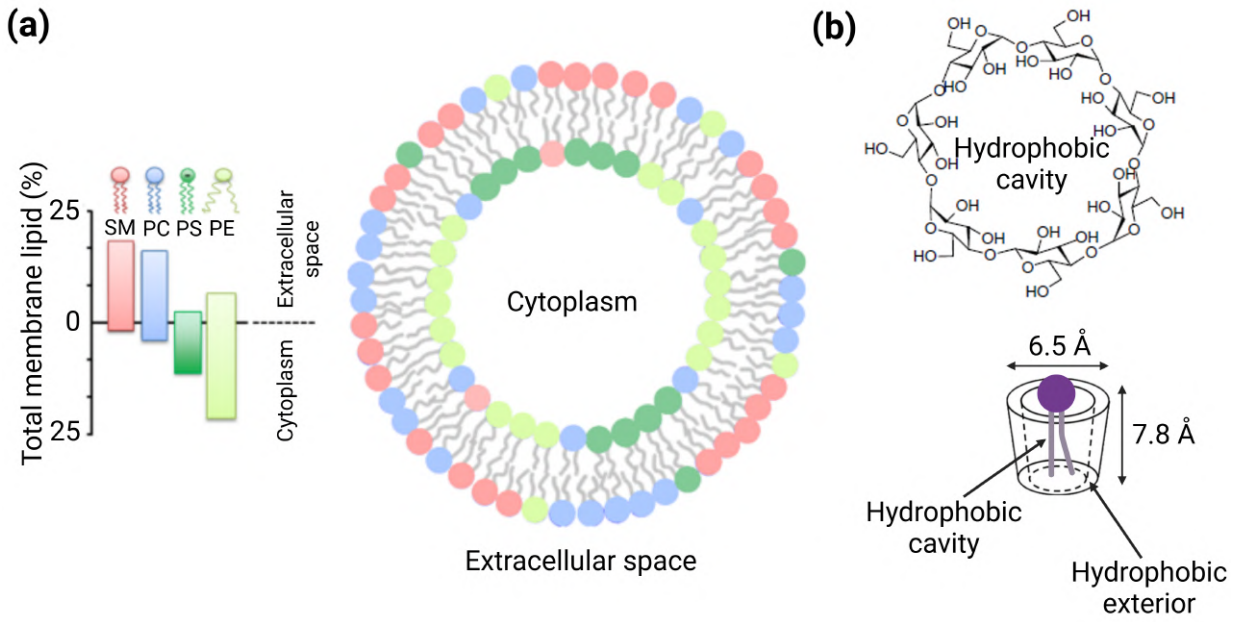

Figure 6.1 – **(a)** *Schematic representation of an asymmetric lipid vesicle, showing some of the main phospholipids present in the plasma membrane of human red blood cells (sphingomyelin, SM; phosphatidylcholine, PC; phosphatidylserine, PS; phosphatidylethanolamine, PE), which are non-uniformly distributed between the outer and inner membrane leaflets. The bar plot indicates the relative enrichment of each lipid species in the two leaflets. Adapted from [253].* **(b)** *The chemical structure of mβCD results in a hydrophilic outer surface and a hydrophobic cavity which can host phospholipids by interacting with their hydrocarbon tails. Adapted from [34].*

physiological processes such as immune cell activation [256, 257]. Moreover, dysregulation of PS exposure contributes also to thrombotic disorders [258], cancer [259], and viral immune evasion [260].

In this context, membrane lipid asymmetry has emerged as a critical parameter of increasing interest, as it regulates interactions with peptides [261], proteins [248, 262, 263], and exogenous agents, such as NPs [264], modulating their binding affinity, insertion, and translocation. In particular, these processes are strongly influenced by electrostatic interactions arising from differences in lipid composition and charge between the inner and outer leaflets [265, 266]. Therefore, the preparation of asymmetric membranes is essential for developing biomimetic systems that better reproduce the asymmetry of biological membranes, enhancing the efficacy and reliability of *in vitro* studies.

Several experimental methods have been developed to generate asymmetry in model systems. Approaches that involve the preparation of planar membranes using sequential deposition techniques, such as Langmuir-Blodgett/Langmuir-Schaefer methods, offer high stability and well-defined asymmetry, but they are limited to supported membranes rather than freely suspended vesicles [267]. Microfluidic and double-emulsion methods allow independent control of the lipid composition of each leaflet during vesicle formation, providing compositional precision, but often they require complex experimental setups [251, 268–271].

Post-vesicle formation approaches based on selective lipid exchange enable leaflet-specific modification of preformed vesicles, offering experimental flexibility, although with limited long-term stability due to lipid flip-flop. These methods include applying a pH gradient to vesicles containing negatively charged lipids [272, 273], adding external enzymes that selectively modify the head groups of lipids in the outer leaflet [274, 275], introducing lipid carrier molecules that facilitate the exchange of outer leaflet lipids between different vesicles [276–278].

Among post-vesicle formation modification approaches, the use of lipid exchange catalyzed by methyl-β-cyclodextrin (mβCD) as lipid carrier has been demonstrated to be a versatile strategy for the preparation of asymmetric vesicles [34, 279–281]. mβCD is a water-soluble, ring-shaped oligosaccharide with a hydrophilic outer surface and a hydrophobic central cavity whose size is suitable to host lipid tails (Figure 6.1**b**).

By forming reversible complexes with lipids, mβCD replaces unfavorable interactions with water with favorable interactions with lipid apolar tails. At high concentrations, mβCD can fully dissolve lipid vesicles, while at lower concentrations an equilibrium between intact vesicles, mβCD-lipid complexes, and free mβCD [282, 283] is established. This mixture is the starting point for the preparation of asymmetric vesicles (aLUVs). This method exploits the ability of mβCD to selectively extract and transfer lipids between membranes, enabling controlled modification of the lipid composition of the outer leaflet of preformed vesicles. As a result, membrane asymmetry can be obtained without disrupting vesicle integrity or altering size.

In this work, the mβCD approach is employed to prepare asymmetric DOPC/DPPC/DPPS vesicles enriched in DPPS in the inner leaflet. This system will enable the future study of amphiphilic AuNP-membrane interactions under conditions that mimic natural lipid asymmetry. Since such studies have not yet been performed using amphiphilic AuNPs, these vesicles will offer a valuable platform for a systematic investigation of their interactions with asymmetric membranes, allowing investigation of leaflet-specific binding, insertion, and effects on membrane organization.

6.2 Materials and methods

6.2.1 Symmetric vesicle preparation and characterization

Vesicle preparation. MLVs of DOPC were prepared at a lipid concentration of $4\,\mathrm{mg\,mL^{-1}}$ by hydrating a dry lipid film, followed by sonication for 15 min at room temperature (see Appendix A for more details).

MLVs of DPPC containing $(0-30)\,\mathrm{mol\,\%}$ DPPS were also prepared. Since the main phase transition temperature of DPPC is approximately $(41-42)\,^{\circ}\mathrm{C}$, whereas that of DPPS is higher, around $(54-55)\,^{\circ}\mathrm{C}$, lipid films were hydrated and sonicated while maintaining

the water temperature at approximately 60 °C to ensure that all lipid components were in the fluid phase. Samples were sonicated for 1 h, vortexing every 15 min. Subsequently, unilamellar vesicles were prepared by extrusion through a 0.1 µm polycarbonate membrane for 31 times, obtaining LUVs with an average diameter of approximately 100 nm. During extrusion, the temperature of the mini-extruder was maintained at 60 °C. The final lipid concentration was 2 mg mL^{-1}.

Both DOPC MLVs and DPPC/DPPS LUVs were prepared in a buffer containing 10 mM Trizma® base and 150 mM NaCl (pH 7.4). Vesicle batches were stored at 4 °C.

Vesicle characterization. The hydrodynamic diameters of both MLVs of DOPC and LUVs of DPPC/DPPS were measured in the buffer solution. MLV donor and LUV acceptor vesicles were prepared in advance and stored at 4 °C. Before starting the aLUV preparation protocol the size and ζ potential were checked to ensure reproducibility and sample quality. In Figure 6.2**a,b** the DLS size distributions of the vesicles are shown. MLV donor vesicles exhibited diameters larger than 1000 nm, while LUV acceptor vesicles a an average diameter of approximately 100 nm. For DPPC/DPPS LUVs, the ζ potential was also measured at different DPPS molar percentages. Prior to the measurements, vesicle suspensions were diluted 50-fold to reduce the salt concentration. For each dilution, measurements were performed on two independent samples, with two measurements acquired for each sample. Figure 6.2**c** shows the ζ potential as a function of total DPPS content (mol %).

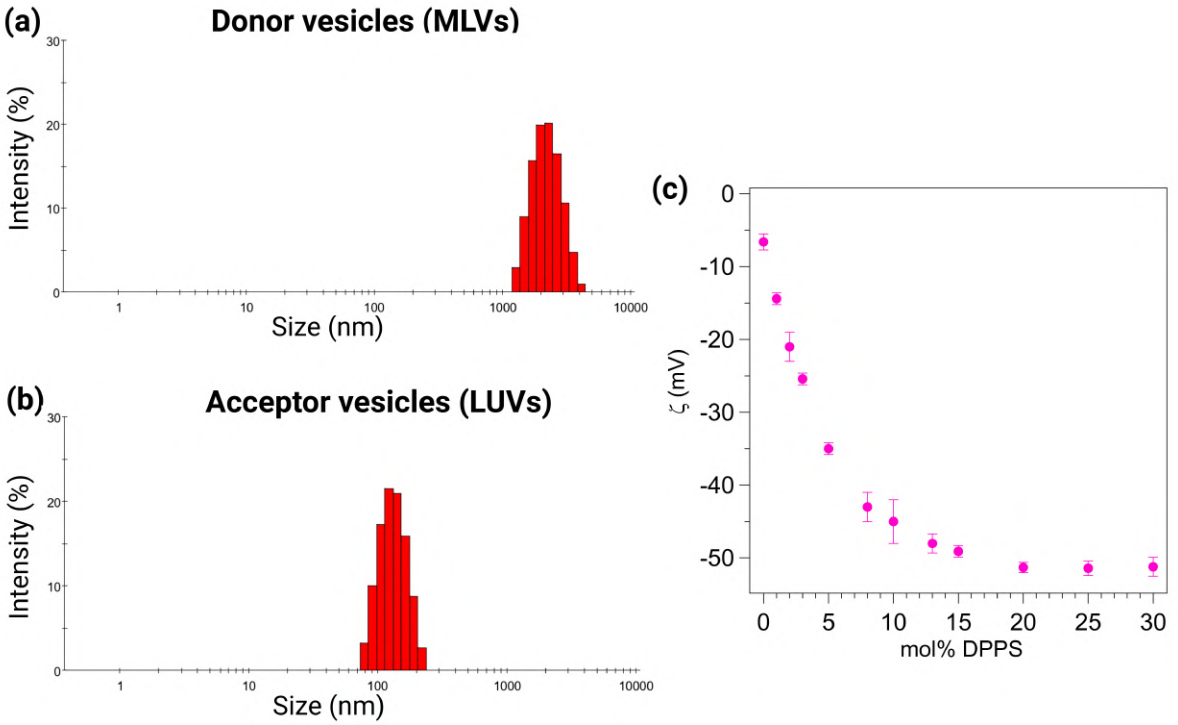

Figure 6.2 – *Representative DLS intensity size distribution of* **(a)** *DOPC MLVs and* **(b)** *DPPC/DPPS symmetric LUVs.* **(c)** *ζ potential as a function of the total DPPS percentage in symmetric DPPC/DPPS LUVs.*

6.3 Results and discussion

6.3.1 Asymmetric vesicle preparation protocol

The cyclodextrin-mediated lipid exchange protocol developed in this thesis is based on a mβCD-mediated donor-acceptor strategy modified from Markones et al [281]. Figure 6.3 schematically illustrates the main steps of the protocol. The procedure starts with a solution of DOPC MLVs, referred to as donor vesicles, which are mixed with mβCD to disrupt the majority of MLVs and form mβCD-lipid complexes. This mixture is then combined with symmetric LUV acceptor vesicles composed of DPPC/DPPS, allowing mβCD-catalyzed lipid exchange to occur and resulting in the formation of aLUVs. Subsequent purification steps are performed to remove residual MLVs, free mβCD, and mβCD-lipid complexes. Therefore, the overall process aims to generate DOPC/DPPC/DPPS aLUVs by exchanging DOPC from the donor vesicles with DPPC or DPPS in the outer leaflet of the symmetric LUV acceptors.

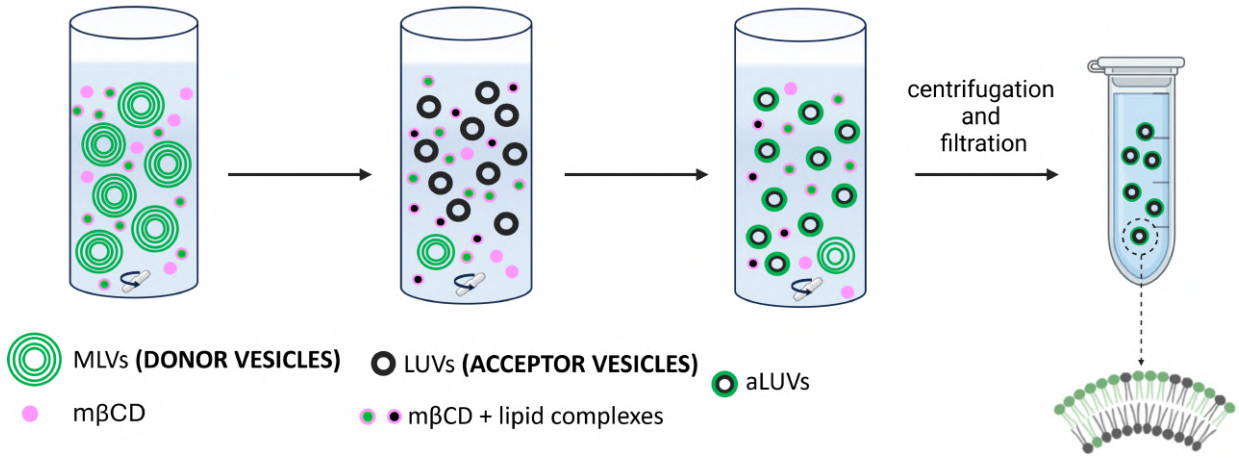

Figure 6.3 – ***Donor-acceptor strategy for aLUV preparation.*** *Schematic representation of the protocol used to prepare aLUVs via cyclodextrin-mediated lipid exchange. In the first step, MLVs (donor vesicles) were incubated under stirring with mβCD, which extracts donor lipids (i.e, DOPC) forming lipid-cyclodextrin complexes and reducing the number of donor vesicles. In the second step, mβCD-treated MLV samples are directly mixed with preformed LUVs (acceptor vesicles made of DPPC/DPPS), enabling lipid exchanges to the outer leaflet of the acceptor membrane. Finally, aLUVs are isolated from excess cyclodextrin, mβCD-lipid complexes, and donor MLV carryover by successive purification steps, including filtration by Amicon Ultra filter tubes (*100 kDa*). Created in Biorender.*

DOPC exchange with DPPC does not alter the overall surface charge, whereas exchanging DOPC with DPPS leads to a reduction of charge at the outer membrane surface, resulting in a higher concentration of negatively charged lipids in the inner leaflet. In addition, unsaturated lipids for donor vesicles and saturated lipids for acceptor vesicles were selected to achieve different interactions with mβCD. In fact, previous work by Huang and London [284] has shown that saturated lipids, such as those present in the acceptor vesicles, require

higher mβCD concentrations for solubilization compared to unsaturated lipids like DOPC. In particular, the resistance of DPPC to solubilization is likely due to its tightly packed gel-phase state at room temperature, which confers higher membrane stability compared to lipids with unsaturated acyl chains. This different behavior, depending on the nature of the acyl chains, allows cyclodextrin to efficiently solubilize the donor vesicles and form mβCD-lipid complexes, while at the same time preserving the structural integrity of the acceptor LUVs during the exchange step.

This protocol was optimized using 85:15 DPPC:DPPS acceptor vesicles with a zeta potential of approximately -50 mV (Figure 6.2**c**). A series of experiments was conducted to fine-tune the steps and timing of the protocol.

In the first step, the mβCD-to-lipid molar ratio R was optimized to obtain the highest lipid concentration solubilized by mβCD. The concentration of mβCD was set at 40 mM, which, according to [284], is sufficient to disrupt most DOPC MLVs while remaining low enough to maintain the integrity of DPPC/DPPS LUVs during the subsequent lipid exchange step. Subsequently, different molar ratios R were tested. Keeping the mβCD concentration constant, the lipid concentration was progressively decreased, corresponding to increasing values of R. In Figure 6.4, the results for $R = 60$, $R = 90$, and $R = 100$ are shown. For $R = 60$ and $R = 90$ (corresponding to lipid concentrations of 667 µM and 444 µM, respectively), no disruption of MLVs was observed. At $R = 100$ (lipid concentration of 400 µM), partial solubilization occurred. The number size distribution reveals the presence of mβCD-lipid complexes in some samples (Figure 6.4**c**, top row), while in others are absent (Figure 6.4**c**, bottom row).

In Figure 6.5**a**, the condition $R = 110$ is shown. Residual MLVs and small complexes can be detected in the intensity size distribution. However, the number distribution indicates that the majority of the sample consists of smaller structures. Therefore, the molar ratio $R = 110$, obtained from a cyclodextrin concentration of 40 mM and a lipid concentration of 363 µM, was fixed. For all conditions tested, DOPC MLVs were disrupted and lipids extracted by cyclodextrin at 55 °C for 45 min under continuous stirring with a magnetic bar.

In the second step, the mβCD-lipid complexes were incubated with symmetric 85:15 DPPC:DPPS LUVs at 60 °C for 30 min under continuous stirring with a magnetic bar. Donor and acceptor vesicles were mixed at a 1:1 molar ratio. Although higher donor-to-acceptor ratios are typically used to enhance lipid exchange efficiency [34], in this case, given the fixed donor concentration of 363 µM, higher ratios would require a proportional reduction of the acceptor concentration. This would lead to a lower overall concentration of purified aLUVs, limiting the amount available for subsequent experiments. Therefore, an equimolar donor-to-acceptor ratio was chosen to balance effective lipid exchange with a sufficient final yield of aLUVs.

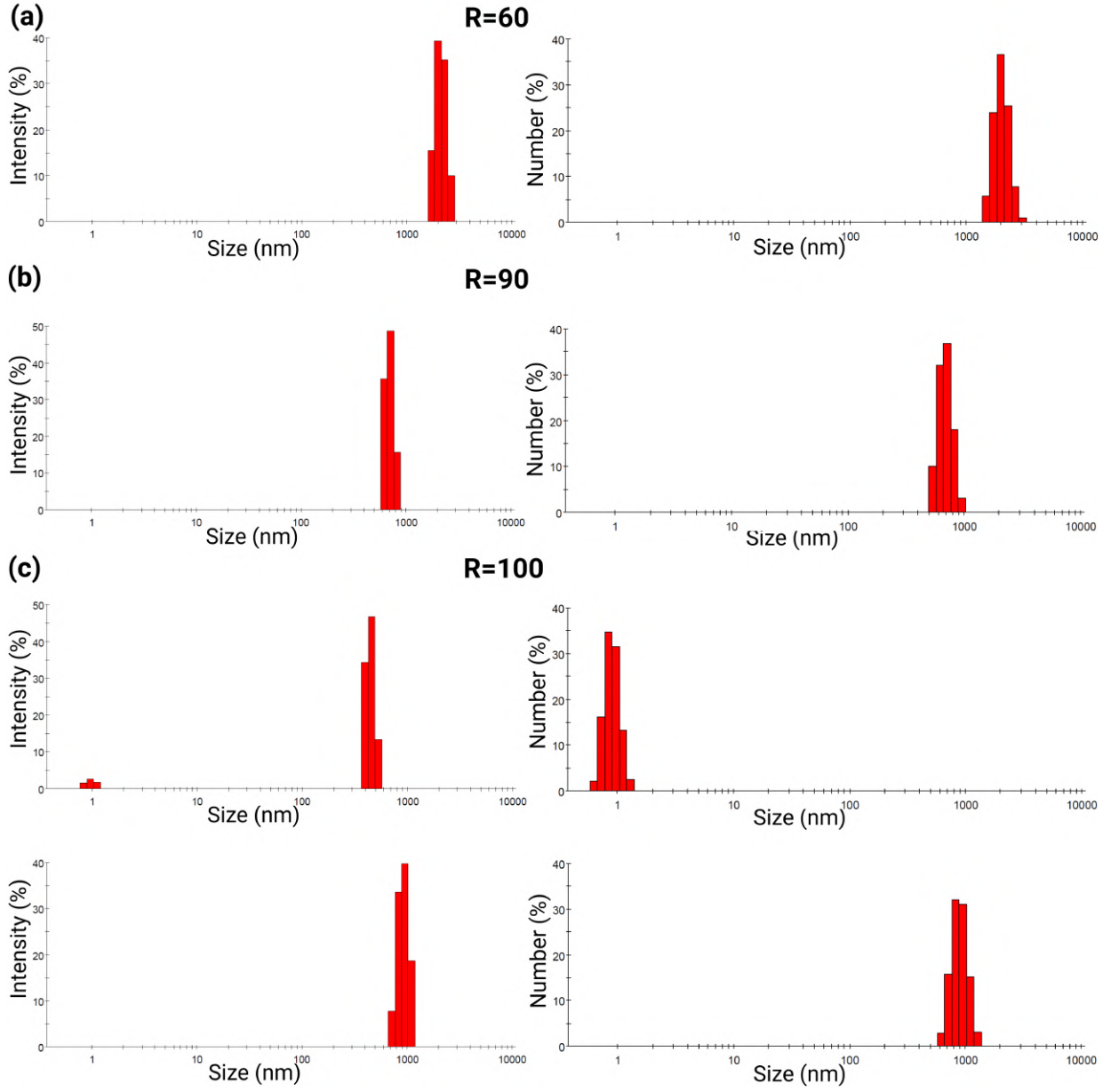

Figure 6.4 – *Representative DLS intensity and number size distributions of MLV donor vesicles incubated with* 40 mM *mβCD at different lipid concentrations.*

Post-exchange aLUVs were purified through successive centrifugation and filtration steps in order to separate the vesicles from residual MLVs, free mβCD-lipid and mβCD-lipid complexes. To isolate post-exchange aLUVs, $(400-500)$ µL of sample were transferred into a buffer-washed Amicon Ultra 2 mL filter (MWCO 100 kDa), centrifugated for $(3-5)$ min at $(3500-4000)$ rpm, and diluted again. Dilution and centrifugation were repeated for tipically six or seven cycles. Finally, after the purification steps, the final sample was analyzed by DLS and was found to predominantly consist of aLUVs. This is confirmed by the number size distribution of the purified aLUVs, as shown in Figure 6.5**b**.

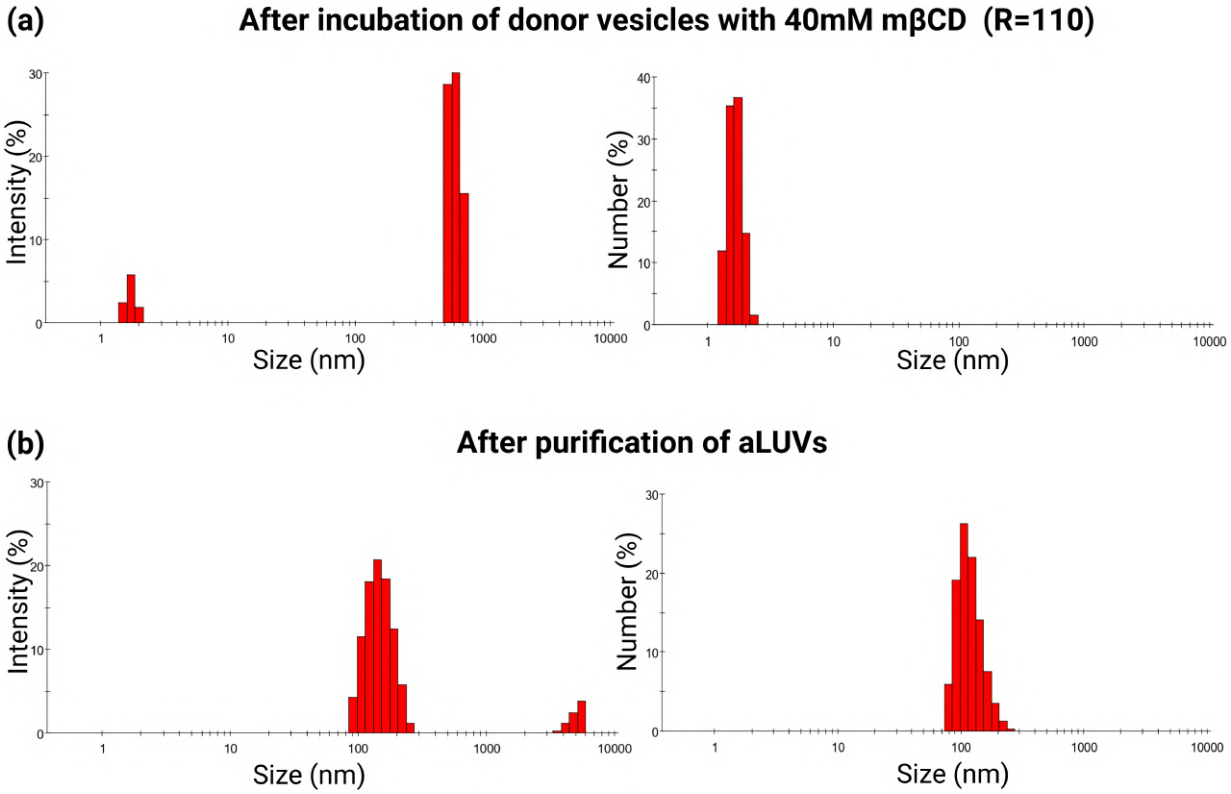

Figure 6.5 – *Representative DLS intensity and number size distributions of vesicles.* **(a)** *After the mixing of donor vesicles with mβCD, two peaks are observed in the intensity distribution, corresponding to the formation of mbCD-lipid complexes and residual MLVs. The number distribution shows that the majority of the sample is composed of the complexes.* **(b)** *Size distribution of aLUVs after purification show that vesicles have a diameter comparable to the initial acceptor vesicles. A secondary peak at larger sizes appears in the intensity distribution but disappears in the number distribution, indicating that the sample mainly consists of aLUVs.*

6.3.2 Evaluation of the lipid exchange

The efficiency of lipid exchange in final aLUV samples was assessed as described by Markones et al [281]. This was achieved by constructing a calibration curve based on ζ-potential measurements of symmetric vesicles prepared with increasing PS concentrations. Since the lipid exchange process alters the surface charge of the outer leaflet, changes in ζ-potential provide a reliable estimate of the extent of lipid exchange, reflecting the amount of DPPS exposed on the external leaflet. Figure 6.6 shows the ζ-potential calibration curve which was fitted using a sixth-degree polynomial function, given by

$$\zeta(x) = -6.5\,\mathrm{mV} - 8.3\,\mathrm{mV}\,x + 0.7\,\mathrm{mV}\,x^2 - 0.03\,\mathrm{mV}\,x^3 + 6.5\cdot10^{-4}\,\mathrm{mV}\,x^4 - 5.7\cdot10^{-6}\,\mathrm{mV}\,x^5 \quad (6.1)$$

where ζ is the ζ-potential expressed in mV, x is the total DPPS molar fraction, and the coefficients were obtained from the fit.

In Figure 6.6, the ζ-potential of the 85:15 DPPC:DPPS LUV acceptor vesicles is shown (blue circle), along with the zeta potential of the aLUV sample (blue star) obtained after

lipid exchange, approximately −21 mV. Using Equation 6.1, the corresponding percentage of PS was determined to be around 2 %. This result indicates a significant modification of the surface charge compared to the symmetric reference vesicles and supports the use of ζ-potential measurements as a preliminary method to evaluate lipid exchange efficiency and the redistribution of DPPS in the outer leaflet. Therefore, the system functions as expected, with the charge decreasing consistently with the exchange, but nothing can be inferred about its stability over time.

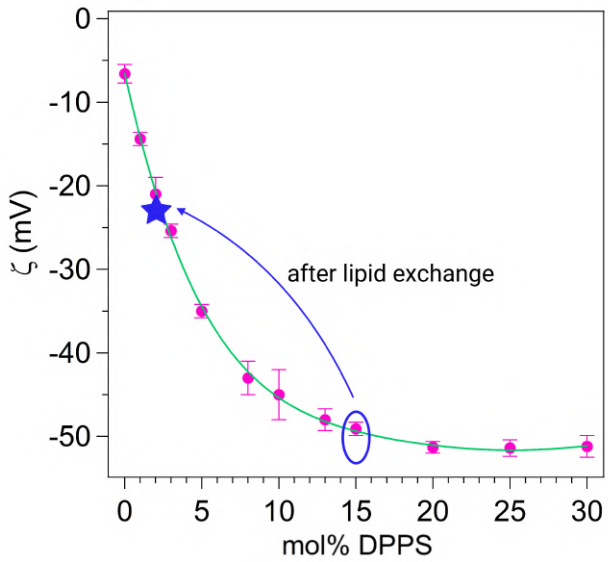

Figure 6.6 – *Fitted calibration curve of the zeta potential measured for symmetric LUV acceptor vesicles. The x-axis represents the total DPPS molar percentage in the vesicles. The green line corresponds to the empirical fit using Equation 6.1. The blue circle indicate the zeta potential of the symmetric acceptor LUVs used in the lipid exchange, while the star represents the zeta potential of the resulting aLUVs after lipid exchange between donor and acceptor vesicles.*

6.4 Conclusions and future perspectives

In this work, I focused on optimizing a protocol for the formation of model membranes characterized by an asymmetric lipid composition. A protocol based on mβCD-mediated lipid exchange was used to obtain asymmetric vesicles with a higher percentage of negatively charged lipid in the inner leaflet. The lipid exchange occurs between donor MLVs composed of DOPC and acceptor symmetric LUVs composed of DPPC/DPPS. Vesicles were characterized using DLS and zeta potential measurements. DLS was used to investigate the size of the symmetric vesicles and the post-exchange asymmetric vesicles. Zeta potential measurements provided information on vesicle surface charge, related to the amount of DPPS in the outer membrane leaflet. Symmetric acceptor vesicles were prepared at different DPPC/DPPS molar ratios, and zeta potential measurements were used to construct a calibration curve to assess the zeta potential of asymmetric vesicles.

Lipid exchange was performed on symmetric vesicles with a DPPC:DPPS molar ratio of 85:15. This process resulted in final asymmetric vesicles showing a significant decrease in zeta potential, providing preliminary evidence of efficient lipid exchange.

For future studies, further optimization of the protocol could focus on improving the purification of aLUVs to more efficiently remove residual mβCD and donor vesicles. In addition, advanced characterization techniques, such as NMR spectroscopy, could be employed to quantify the final lipid concentration [285] and composition [286, 287], providing a more precise assessment of membrane asymmetry. Studies could also assess the temporal stability of asymmetry, including investigation of lipid flip-flop between leaflets [286]. These optimized asymmetric vesicles could then be used as a versatile platform for studying interactions with anionic or cationic NPs, offering insights into membrane perturbation and NP uptake. Moreover, these membrane models could play a crucial role in investigating the effects of asymmetry on biological relevant processes, such as membrane fusion [288].

Conclusions

This thesis explores the interactions of sub-6 nm amphiphilic AuNPs with model lipid membranes, exploiting a combination of complementary biophysical techniques. The results provide original insights into the effects of AuNPs on lipid vesicles of varying size and composition, as reported below.

NP-mediated membrane fusion (Chapter 3). In this study, I investigated the interplay between membrane curvature and vesicle size in regulating the mechanism of NP-induced biomimetic membrane fusion. To this purpose, I employed MUS:OT AuNPs and DOPC vesicles containing a biologically relevant fraction of cholesterol [91]. I used AuNPs with core diameters, respectively, smaller than the lipid bilayer thickness and comparable to the bilayer thickness, and vesicles of different curvatures, in particular LUVs and SUVs. QCM-D experiments enabled the investigation of AuNP uptake into vesicle bilayers as well as vesicle-vesicle interactions occurring during NP-mediated fusion. Fluorescence spectroscopy provided complementary information on hemifusion and full fusion, including pore formation, between vesicles. The results show that both small and large AuNPs can penetrate the membrane without causing damage. However, only the small AuNPs promote vesicle fusion regardless of membrane curvature, whereas large AuNPs exhibit no fusogenic activity with low-curvature membranes but can induce fusion in membranes with high curvature. These findings were further supported by MD simulations, which provided molecular-level insights into the stalk formation mechanism, and showed that the stalk formed in the presence of smaller AuNPs is energetically more stable than that formed with larger AuNPs. This is due, on one hand, to the size of the AuNP core, which provides greater ligand conformational flexibility in smaller AuNPs [183], and on the other hand, to membrane curvature, which favors hydrophobic connections between leaflets promoting the formation of fusion intermediates.

The results obtained in this work indicate that understanding the factors governing NP-mediated synthetic vesicle fusion is essential for the design of efficient fusion machineries.

As relatively subtle differences in NP size and membrane curvature can result into very different outputs of the fusion process, a precise tuning of these physical determinants is required for the future development of powerful synthetic fusion tools.

Structural changes in GUVs doped with NPs (Chapter 4). This project focuses on the effect of NPs on the morphology of GUVs, which mimic essential properties of cellular membranes and provide a valuable platform for studying membrane-NP interactions. While NP uptake into giant vesicles is widely reported in the literature [81, 88, 90], a systematic investigation of NP-induced morphological changes is still lacking.

To this purpose, I employed MUS:OT AuNPs with a gold core diameter of 3.2 nm and fluid-phase DOPC GUVs. Changes in membrane morphology, including tubulation and pore formation, were studied using a single-vesicle approach, visualizing the vesicles with confocal fluorescence and phase-contrast microscopy. Labeled GUVs were used to quantify membrane structures in the presence or absence of NPs, while an SRB fluorescence leakage assay and phase-contrast imaging allowed detection of pore formation. Image analysis revealed that incubation with NPs induced morphological changes in GUV membranes, particularly an increase in external structures, consistent with trends suggested by computational studies [211]. Importantly, no detectable increase in membrane permeability was observed. These results are in agreement with previous findings indicating that the amphiphilic coating of AuNPs stabilizes NP-membrane interactions while preventing disruptive effects on bilayer integrity [14, 81].

Effect of NPs on regulating membrane permeability under osmotic stress (Chapter 5). In this project, I investigated the effect of NPs on vesicles exposed to a sugar concentration gradient between the vesicle lumen and the surrounding solution. This gradient drives water diffusion through the membrane, resulting in changes in vesicle volume. To monitor these changes, I performed SAXS experiments to obtain quantitative information on vesicle size and bilayer thickness. The results show that, without NPs, the vesicle radius increases under hyposmotic conditions due to swelling, and decreases under hyperosmotic conditions due to shrinking. In the presence of NPs, the effect on vesicles changes, likely due to a stabilizing effect of NPs on the membrane. Indeed, under non-equilibrium conditions, the vesicle radius remains similar. This behavior can be explained by the fact that, under hyposmotic gradient, NPs prevent the membrane from reaching its maximum tension and, consequently, the maximum expansion volume. Conversely, under hyperosmotic conditions, NPs can limit membrane reorganization, reducing vesicle shrinking.

To gain a more detailed understanding of these mechanisms, further investigations could be performed, for example using Laurdan fluorescence measurements. This fluorescent probe has already been used to study osmotic stress in biomembranes [242] and can provide information on membrane organization, bending, tension, and dynamics.

Asymmetric lipid membranes: towards more biomimetic models (Chapter 6). This project aimed to optimize a protocol to prepare model lipid membranes with enhanced biomimicry. To obtain asymmetric vesicles, I employed a cyclodextrin-mediated lipid exchange protocol combined with the donor-acceptor strategy [34, 281], producing DOPC/DPPC/DPPS vesicles with a higher fraction of charged lipids in the inner leaflet. The vesicles were characterized using DLS and zeta potential measurements, providing information on hydrodynamic diameter and surface charge, respectively. In particular, zeta potential proved to be a reliable method for validating the efficiency of the protocol by measuring the fraction of charged lipids in the outer leaflet.

Further studies are required to fully characterize the asymmetry. Future experiments could include quantitative determination of lipid content in each leaflet (e.g., via nuclear magnetic resonance [34, 286]) and assessment of long-term stability, in terms of quantification of the time window in which the asymmetry is maintained.

Future perspectives

The experiments discussed in this thesis have provided new insights into NP-membrane interactions, paving the way for future investigations. The studies on membrane permeability in the presence of osmotic stress could be extended to more complex lipid mixtures and to other biomimetic systems, such as GUVs, allowing direct comparisons of stress-induced effects across vesicles of different sizes and compositions. Asymmetric vesicles could be employed to investigate the uptake of both anionic and cationic NPs, enabling a systematic exploration of electrostatically driven mechanisms of interaction. The fusogenic properties of AuNPs could be investigated using asymmetric vesicles and GUVs that mimic biologically relevant lipid compositions, allowing the mimicking of cellular fusion processes. Although challenging, especially for what concerns the use of asymmetric membranes, these experiments could yield valuable information both for basic research and for the design of safe fusogenic agents or drug carriers.

APPENDIX A

Materials and methods for vesicle preparation

For the vesicles used in Chapters 3, 4, 5, and 6, the following lipids were employed:

- 1,2-dioleoyl-sn-glycero-3-phosphocholine (18:1 (Δ9-cis) PC, DOPC, ≥ 99 %, Avanti Polar Lipids);
- cholesterol (Chol, ≥ 99 %, Sigma-Aldrich);
- 1,2-dipalmitoyl-sn-glycero-3-phosphocholine (16:0 PC, DPPC, ≥ 99 %, Avanti Polar Lipids);
- 1,2-dipalmitoyl-sn-glycero-3-phospho-L-serine (16:0 PS, DPPS, sodium salt), ≥ 99 %, Avanti Polar Lipids);

The first two probes are labelled glycerophospholipids, while the third one is a water-soluble fluorescent dye. Their chemical structures are shown in Figure A.1.

In addition, the following fluorescent probes were used in the experiments of Chapters 3, and 4:

- 1,2-dioleoyl-sn-glycero-3-phosphoethanolamine-N-(7-nitro-2-1,3-benzoxadiazol-4-yl) (18:1 NBD-PE, ammonium salt ≥ 99 %, Avanti Polar Lipids);
- 1,2-dioleoyl-sn-glycero-3-phosphoethanolamine-N-(lissamine rhodamine B sulfonyl) (18:1 Liss Rhod-PE, ammonium salt, ≥ 99 %, Avanti Polar Lipids);
- Sulphorodamine B (acid form) (SRB, dye content 95 %, Sigma-Aldrich)

The chemical structures are shown in Figure A.2.

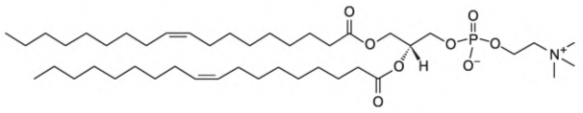

1,2-dioleoyl-sn-glycero-3-phosphocholine, 18:1(Δ9-Cis) PC (**DOPC**)

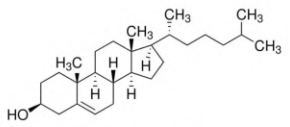

Cholesterol, **chol**

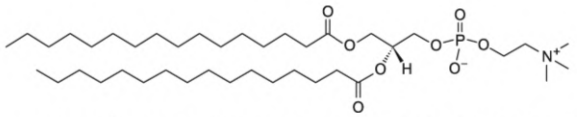

1,2-dipalmitoyl-sn-glycero-3-phosphocholine, 16:0 PC (**DPPC**)

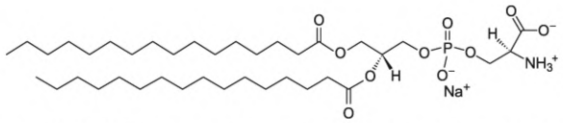

1,2-dipalmitoyl-sn-glycero-3-phospho-L-serine (sodium salt), 16:0 PS (**DPPS**)

Figure A.1 – *Chemical structures and corresponding names of the lipids used in the experiments presented in Chapters 3, 4, 5, and 6.*

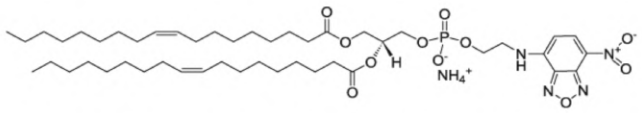

1,2-dioleoyl-sn-glycero-3-phosphoethanolamine-N-(7-nitro-2-1,3-benzoxadiazol-4-yl) (ammonium salt) (18:1 **NBD-PE**)

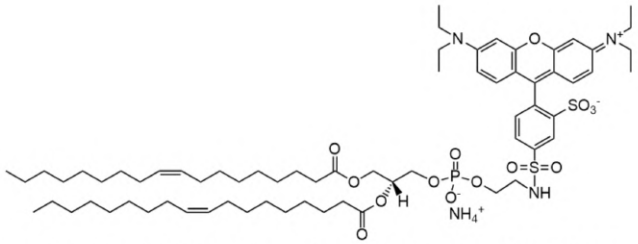

1,2-dioleoyl-sn-glycero-3-phosphoethanolamine-N-(lissamine rhodamine B sulfonyl) (ammonium salt) (18:1 **Liss Rhod-PE**)

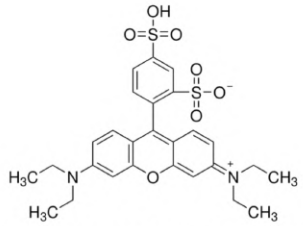

Sulphorodamine B (acid form) (**SRB**)

Figure A.2 – *Chemical structures and corresponding names of the fluorescent probes used in the experiments presented in Chapters 3, and 4.*

A.1 Extrusion method

This method was used for the preparation of both SUVs and LUVs in Chapters 3, 5, and 6.

Lipid stock solutions were prepared in organic solvents, chloroform ($CHCl_3$) was used for neutral lipids, whereas a chloroform:methanol mixture (2:1, v/v, $CHCl_3$:CH_3OH) was employed for charged lipids. Appropriate stoichiometric amounts of the lipids were withdrawn from these stock solutions and mixed in a glass vial to achieve the desired total lipid concentration. A gentle flow of nitrogen was applied to facilitate the evaporation of the organic solvents. Removal of the solvents resulted in the formation of a uniform lipid film deposited at the bottom of the vial. The entire procedure was performed in a chemical fume hood.

The resulting lipid film was kept under vacuum overnight to remove any residual organic solvent that could hinder vesicle formation. The following day, the film was either stored at −20 °C for future vesicle preparations or used immediately. The film was then rehydrated with the desired aqueous solution for the experiment, yielding the final lipid concentration. After vortex mixing for 1 min, the hydrated samples were placed in an ultrasonic bath at room temperature and sonicated for 15 min. For lipid mixtures with high phase transition temperatures, the water in the ultrasonic bath was preheated to the desired temperature and multiple cycles of sonication were performed. This procedure promotes film hydration and leads to the formation of multilamellar vesicles.

Finally, to obtain monodisperse unilamellar vesicles, the lipid suspension was extruded. To this purpose, an Avanti Mini-Extruder (Avanti Polar Lipids) equipped with polycarbonate membranes (Nuclepore filters, Whatman) was used. The membrane pore diameter was selected according to the desired final vesicle size. When necessary, the system can be maintained at the required temperature using a heating plate, as shown in Figure A.3**a**.

The extruder consists of a central body in which a polycarbonate membrane is mounted, as illustrated in the figure. Two gas-tight glass Hamilton syringes are connected to the device. An empty syringe is inserted on one side of the mini-extruder (Figure A.3**a**, left), while the syringe containing the vesicle suspension is placed on the opposite side (Figure A.3**a**, right). By pushing the plunger, the lipid suspension is forced through the polycarbonate membrane and fills the syringe on the opposite side. This procedure is repeated multiple times to ensure homogeneity of the vesicle population, ultimately resulting in the filling of the initially empty syringe.

To ensure that extrusion occurs above the lipid phase transition temperatures, the instrument is equipped with a support that can be heated to the desired temperature using a heating plate.

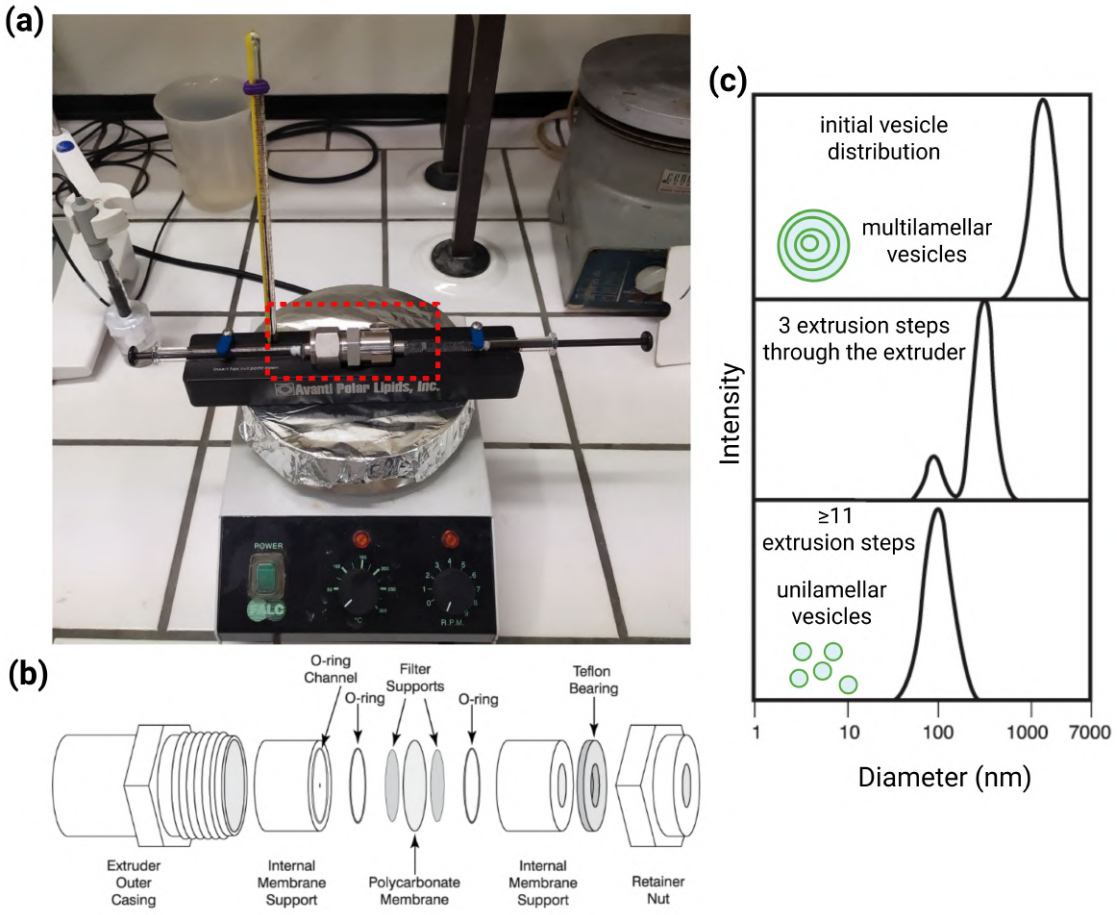

Figure A.3 – ***Experimental setup used for extrusion.*** **(a)** *A fully assembled mini-extruder placed on a heating plate.* **(b)** *Components of the central part of the mini-extruder (framed in* **(a)***) containing the polycarbonate membrane through which the vesicle suspension flows during the extrusion process.* **(c)** *Starting from MLVs, repeated extrusion through a polycarbonate membrane with a fixed pore size result in a homogeneous suspension of unilamellar vesicles.*

A.2 Electroformation method

This method was used to prepare GUVs employed in Chapter 4.

The electroformation method is one of the most widely used techniques for the preparation of GUVs [37]. It is based on the principle of electroswelling and consists in the formation of vesicles from a multilamellar lipid film deposited on a solid, conductive surface [209] [289]. Subsequently, the film is hydrated and the formation of the GUVs is driven by an applied alternating electric field. The most commonly used electrodes are indium tin oxide (ITO)–coated glass slides. Other systems can be employed, including platinum or stainless steel wires, as well as silicon substrates. However, ITO slides offers the advantage of providing a larger swelling area resulting in a higher amount of vesicles (Figure A.4**a**).

For the production of GUVs via electroformation, commercially available systems exist. Nevertheless, homebuilt systems can be adapted for complex membrane compositions and various buffers in which the GUVs are grown. Indeed, the two main factors to be considered

when designing a protocol for GUV preparation are the complexity of the lipid composition and the buffer. When lipids containing polyunsaturated acyl chains are used, oxidized products may form. Similarly, the presence of charged lipids may introduce electrostatic effects that influence vesicle formation. Using the electroformation method, vesicles can be formed in aqueous solutions or in solutions with low ionic strength. In addition, factors that may affect the formation of GUVs include the method used for lipid spreading on solid substrates, which can be performed manually or by spin coating, and the characteristics of the applied electric field (e.g., amplitude, frequency, and duration), which can significantly influence the size of the resulting GUVs.

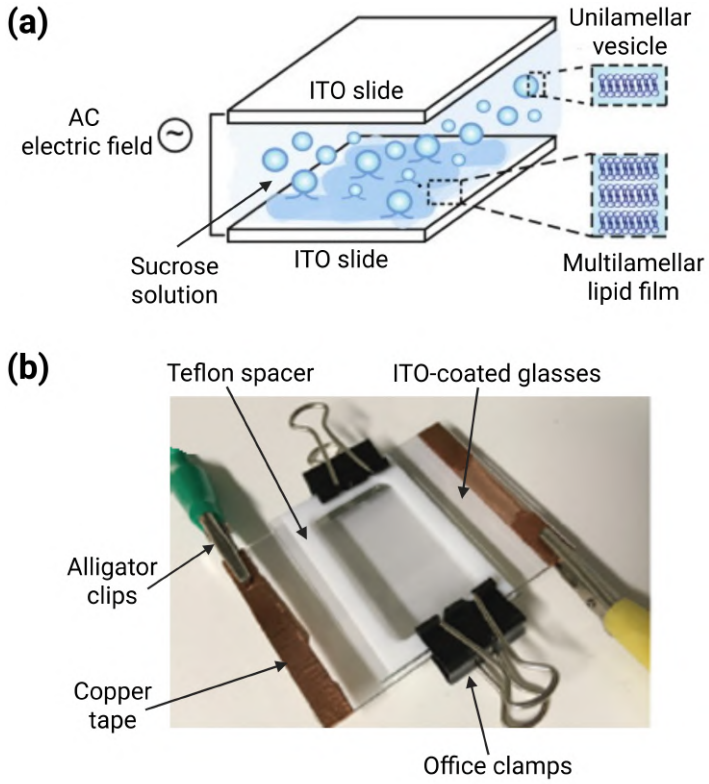

Figure A.4 – ***Electroformation setup for GUV preparation.*** **(a)** *Schematic representation of the electroformation process showing an AC electric field applied across the ITO slides which hydrates the lipid film in a sucrose solution, leading to the formation of GUVs from the multilamellar lipid film.* **(b)** *Homebuilt electroformation chamber composed of two ITO-coated glass slides separated by a Teflon spacer. Electrical contact is ensured by copper tape and alligator clips, while the chamber is assembled using office clamps.*

In this work, a standard electroformation protocol was employed to prepare GUVs of DOPC in a sucrose solution. Before use, the substrates were verified to be electrically conductive by measuring their resistance using an multimeter. The ITO slides were then cleaned sequentially with ultrapure water, ethanol, chloroform, ethanol, and ultrapure water, and then dried under a nitrogen flow. The Teflon spacer was also exposed to a nitrogen flow in order to remove any residual dust. From the lipid stock solutions, prepared as described

in the previous section, 10 µL of lipid solution were withdrawn using glass Hamilton syringes and uniformly spread onto one side of each ITO slide. The slides were then placed in a desiccator and left to dry for at least 1 h to ensure complete removal of the organic solvent. Subsequently, the electroformation chamber was assembled and filled with a sucrose solution of known osmolarity, previously measured using an osmometer. The ITO-plate chambers were then assembled and held together using office clamps, as shown in Figure A.4**b**. The electrodes were connected to an AC field generator. The frequency was set to 10 Hz, and the voltage was adjusted to 1.6 V, the root mean square value was verified with a multimeter. The electric field was applied for approximately 1 h. Finally, approximately 2 mL of the solution containing the GUVs were collected. The vesicles were used immediately for experiments, or stored and used within the following day.

APPENDIX B

Amphiphilic AuNPs synthesis

In this Appendix, a brief overview of the main steps of the synthesis and the subsequent characterization by TEM and ^{1}H-NMR is provided. For a complete and detailed description of the protocol, materials, and TEM images and ^{1}H-NMR spectra analysis, see [74] [87].

The MUS:OT (2:1) AuNPs were synthesized using the thiol-for-oleylamine ligand exchange method. This approach allows the preparation of NPs with a very narrow size distribution, compared to other surface-functionalized AuNP synthetic methods. Controlling this parameter is crucial for experiments involving interactions with lipid membranes, since even small variations in NP size can significantly influence the NP mechanisms of action [143] [183].

This synthesis follows a two-step procedure in which the NP size is controlled first, followed by tuning of the surface ligand composition. Thiol-protected AuNPs were prepared according to the protocol reported by Yang et al. [290], with minor modifications. Briefly, the main steps of this synthetic strategy include:

- Step 1: *controlled growth of the NP Au core.* The NPs were synthesized from a Au precursor dissolved in a mixture of oleylamine (OAm, acting as the capping agent)[1] and the hydrocarbon *n*-octane[2]. OAm, combined with stronger reductants, allows generating spherical OAm-capped AuNPs (OAm-AuNPs) with remarkably narrow size dispersion. Moreover, the core size can be finely tuned between $\sim (1-10)$ nm by varying the reaction temperature at which the reducing agent is injected. Typical reaction temperatures are in the range $\sim (1-50)\,^{\circ}$C. In general, smaller core sizes are

[1] OAm is a weakly bound capping agent known to act as a stabilizer, solvent, and reducing agent.

[2] *n*-octane is a linear hydrocarbon commonly used as a solvent to optimize the final size dispersion of OAm-AuNPs.

favored by higher temperatures. All OAm-AuNPs were washed both in organic solvents and water, and vacuum-dried before performing the thiol-for-OAm ligand exchange.

- Step 2: *formation of the tailored ligand coating.* At this stage, the OAm-coated AuNPs were subjected to the ligand exchange procedure. In thiol-for-OAm ligand exchange, alkylthiols are partially replaced by thiolated species in a dynamic equilibrium process to obtain 2:1 MUS:OT monolayer-protected AuNPs. The exchange efficiency depends on the interaction time and the ligand molar feed ratio. The reaction was carried out overnight at room temperature under continuous stirring (Figure B.1).

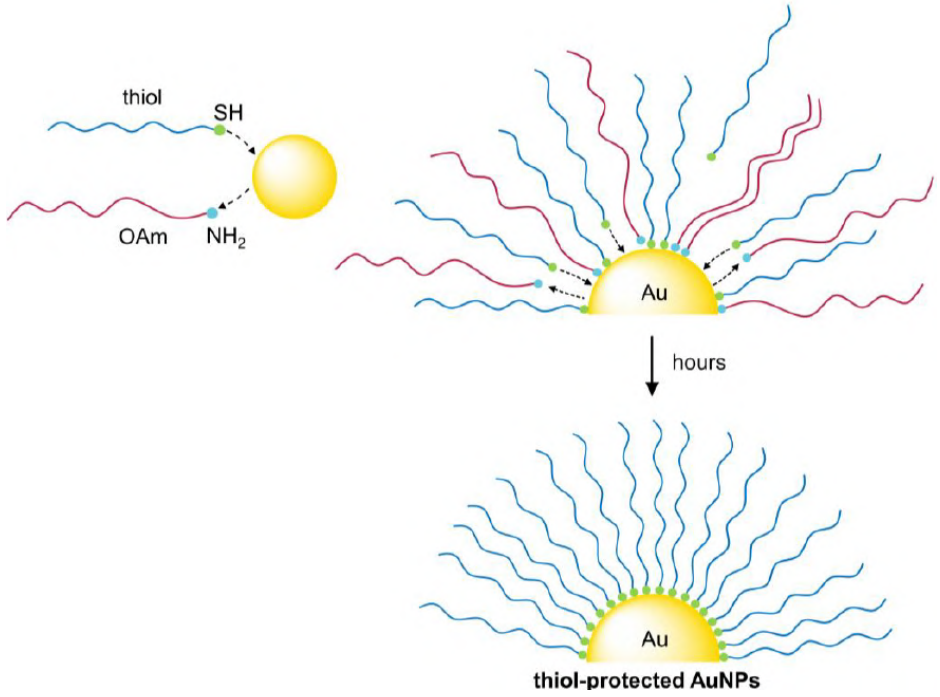

Figure B.1 – *Schematic illustration of the thiol-for-OAm ligand exchange on AuNPs in solution. OAm-coated AuNPs were mixed with an excess of thiol ligands. In the case of mixed monolayers, such as those used in the experiments of this thesis, predefined ligand feed ratios were employed. The strong chemisorption of thiols on Au leads to complete replacement of OAm within* $\sim (12 - 15)$ h. *Reprinted from [74].*

The NPs were characterized by TEM to assess their shape and core size distribution both before and after the thiol ligand- exchange. OAm-coated AuNPs exhibited average sub-6 nm diameters a spherical morphology, with standard deviations in the range $\sim (0.3 - 0.6)$ nm. Monodispersed AuNPs presented a size distribution (i.e., standard deviation/mean diameter $\cdot$ 100) between 20 % and 30 %. In general, smaller NPs were minimally more polydisperse than larger ones. TEM characterization was repeated after OAm-thiol ligands exchange to verify the core size remained unchanged. The resulting thiol-protected AuNPs, originating from the same OAm-coated precursor, show that this two-step approach enables the production of monodisperse amphiphilic NPs with the same Au core sizes and different surface mixtures.

All thiol-functionalized AuNPs were further analyzed by ^{1}H-NMR after iodine etching of the Au core. This analysis allowed calculation of the final (yield) molar ratio between OT and MUS thiols and comparison with the initial ligand feed ratio used during the exchange. In addition, it confirmed the complete removal of OAm, as evidenced by the disappearance of its characteristic signals in the NMR spectra.

The amphiphilic AuNPs used in this thesis have different core sizes but the same MUS:OT surface ratio (2:1). As discussed in previous chapters,chapters, they were characterized by DLS and ζ-potential measurements prior to experiments with lipid membranes.

APPENDIX C

Molecular weight estimation of AuNPs

The NP molecular weight (MW) depends on both the particle size and the ligand composition of the coating. Determining the MW of a NP is crucial for calculating the lipid/NP molar ratio, a key parameter for understanding the mechanisms regulating NP-membrane interactions. This ratio was used in the experiments presented in this thesis to properly interpret the NP effects on model lipid membranes.

The mean MW of the NPs was estimated based on the thiolate-protected Au cluster model reported by Lopez-Acevedo et al [291]. This work considers a NP with a core diameter of 2 nm, composed of 144 Au atoms in icosahedral symmetry, and 60 S atoms bonded on its surface – i.e. Au144(SR)60. From these values, an Au volume density of 34.377 atoms/nm^3 and a ligand surface density of 4.775 molecules/nm^2 can be obtained. In addition, for each NP type, the average core diameters determined by TEM and the surface ligand compositions obtained from ^{1}H-NMR analysis were used. From the ligand surface density, the number of ligands on each NP can be estimated by multiplying this value by the NP surface area. Similarly, the number of Au atoms for each NP can be obtained from the Au volume density by multiplying it by the NP volume. After the number of Au atoms and ligands has been determined, the MW of the NP can be calculated. For Au, an atomic weight of 197 g mol^{-1} was used. The molecular weights of the ligands were calculated from the atomic weight of their constituent atoms. In particular, it has been obtained 266.42 g mol^{-1} for MUS and 145.28 g mol^{-1} for OT, according to their chemical formulas.

Finally, the MW of the NP can be obtained by summing the MW contributions of the Au atoms and the ligands, considering the molar ratios. Based on these calculations, the following MWs were determined for the NPs used in this thesis:

- 2.4 nm core diameter, 2:1 MUS:OT (-), 68 689 $\mathrm{g\,mol^{-1}}$
- 3.2 nm core diameter, 2:1 MUS:OT (-), 151 163 $\mathrm{g\,mol^{-1}}$
- 4.8 nm core diameter, 2:1 MUS:OT (-), 470 836 $\mathrm{g\,mol^{-1}}$

Bibliography

[1] M. C. Roco. "Nanotechnology: convergence with modern biology and medicine". In: *Current Opinion in Biotechnology* 14 (2003), pp. 337–346. DOI: 10.1016/S0958-1669(03)00068-5.

[2] G. M. Whitesides. "Nanoscience, nanotechnology, and chemistry". In: *Small* 1 (2005), pp. 172–179. DOI: 10.1002/smll.200400130.

[3] A. Nel et al. "Toxic potential of materials at the nanolevel". In: *Science* 311 (2006), pp. 622–627. DOI: 10.1126/science.1114397.

[4] Y. Kumar et al. "Functionalized nanoparticles: tailoring properties through surface energetics and coordination chemistry for advanced biomedical applications". In: *Nanoscale* 15 (2023), pp. 6075–6104. DOI: 10.1039/D2NR07163K.

[5] R. Mout et al. "Surface functionalization of nanoparticles for nanomedicine". In: *Chemical Society Reviews* 41 (2012), p. 2539. DOI: 10.1039/c2cs15294k.

[6] L. A. Dykman and N. G. Khlebtsov. "Gold nanoparticles in biomedical applications: recent advances and perspectives". In: *Chemical Society Reviews* 41 (2012), pp. 2256–2282. DOI: 10.1039/C1CS15166E.

[7] M. C. Daniel and D. Astruc. "Gold nanoparticles: assembly, supramolecular chemistry, quantum-size-related properties, and applications toward biology, catalysis, and nanotechnology". In: *Chemical Reviews* 104 (2004), pp. 293–346. DOI: 10.1021/cr030698+.

[8] D. A. Giljohann et al. "Gold nanoparticles for biology and medicine". In: *Angewandte Chemie International Edition* 49 (2010), pp. 3280–3294. DOI: 10.1002/anie.200904359.

[9] A. Albanese, P. S. Tang, and W. C. W. Chan. "The effect of nanoparticle size, shape, and surface chemistry on biological systems". In: *Annual Review of Biomedical Engineering* 14 (2012), pp. 1–16. DOI: 10.1146/annurev-bioeng-071811-150124.

[10] S. B. Gould. "Membranes and evolution". In: *Current Biology* 28 (2018), R381–R385. DOI: 10.1016/j.cub.2018.01.086.

[11] S. J. Singer and G. L. Nicolson. "The fluid mosaic model of the structure of cell membranes". In: *Membranes and viruses in immunopathology*. Elsevier, 1972. DOI: 10.1016/B978-0-12-207250-5.50008-7.

[12] D. Casares, P. V. Escribá, and C. A. Rosselló. "Membrane lipid composition: effect on membrane and organelle structure, function and compartmentalization and therapeutic avenues". In: *International Journal of Molecular Sciences* 20 (2019), p. 2167. DOI: 10.3390/ijms20092167.

[13] A. Verma et al. "Surface-structure-regulated cell-membrane penetration by monolayer-protected nanoparticles". In: *Nature Materials* 7 (2008), pp. 588–595. DOI: 10.1038/nmat2202.

[14] E. Canepa et al. "Non-disruptive uptake of anionic and cationic gold nanoparticles in neutral zwitterionic membranes". In: *Scientific Reports* 11 (2021). DOI: 10.1038/s41598-020-80953-3.

[15] P. L. Yeagle. *The membranes of cells*. Cambridge, MA: Academic Press, 2016.

[16] A. Luchini and G. Vitiello. "Mimicking the mammalian plasma membrane: an overview of lipid membrane models for biophysical studies". In: *Biomimetics* 6 (2021), p. 3. DOI: 10.3390/biomimetics6010003.

[17] H. I. Ingólfsson et al. "Lipid organization of the plasma membrane". In: *Journal of the American Chemical Society* 136 (2014), pp. 14554–14559. DOI: 10.1021/ja507832e.

[18] V. K. Sharma and E. Mamontov. "Multiscale lipid membrane dynamics as revealed by neutron spectroscopy". In: *Progress in Lipid Research* 87 (2022). DOI: 10.1016/j.plipres.2022.101179.

[19] M. Nakano et al. "Flip-flop of phospholipids in vesicles: kinetic analysis with time-resolved small-angle neutron scattering". In: *Journal of Physical Chemistry B* 113 (2009), pp. 6745–6748. DOI: 10.1021/jp900913w.

[20] R. H. Garrett and C. M. Grisham. *Biochimica*. Padova, IT: Piccin Nuova Libraria, 2014.

[21] T. Harayama and H. Riezman. "Understanding the diversity of membrane lipid composition". In: *Nature Reviews Molecular Cell Biology* 19 (2018), pp. 281–296. DOI: 10.1038/nrm.2017.138.

[22] R. Pignatello. *Drug–biomembrane interaction studies*. Cambridge, UK: Woodhead Publishing Limited, 2013. DOI: 10.1533/9781908818348.

[23] K. Palmano et al. "The role of gangliosides in neurodevelopment". In: *Nutrients* 7 (2015), pp. 3891–3913. DOI: 10.3390/nu7053891.

[24] S. Sipione et al. "Gangliosides in the brain: physiology, pathophysiology and therapeutic applications". In: *Frontiers in Neuroscience* 14 (2020). DOI: 10.3389/fnins.2020.572965.

[25] J. N. Israelachvili. *Intermolecular and surface forces*. Cambridge, MA: Academic Press, 2011. DOI: 10.1016/C2009-0-21560-1.

[26] R. A. L. Jones. *Soft condensed matter*. Oxford, UK: Oxford University Press, 2002.

[27] T. Mužić et al. "Melting transitions in biomembranes". In: *Biochimica et Biophysica Acta (BBA) - Biomembranes* 1861 (2019), p. 183026. DOI: 10.1016/j.bbamem.2019.07.014.

[28] K. Simons and E. Ikonen. "Functional rafts in cell membranes". In: *Nature* 387 (1997), pp. 569–572. DOI: 10.1038/42408.

[29] K. Simons and W. L. C. Vaz. "Model systems, lipid rafts, and cell membranes". In: *Annual Review of Biophysics and Biomolecular Structure* 33 (2004), pp. 269–295. DOI: 10.1146/annurev.biophys.32.110601.141803.

[30] M. Eeman and M. Deleu. "From biological membranes to biomimetic model membranes". In: *Biotechnologie, Agronomie, Société et Environnement* 14 (2010), pp. 691–708. URL: https://orbi.uliege.be/bitstream/2268/81993/1/2010_Eeman_Deleu_%20BASE.pdf.

[31] E. Rascol, J.-M. Devoisselle, and J. Chopineau. "The relevance of membrane models to understand nanoparticles–cell membrane interactions". In: *Nanoscale* 8 (2016), pp. 4780–4798. DOI: 10.1039/C5NR07954C.

[32] J. Y. Wong et al. "Polymer-cushioned bilayers. An investigation of interaction forces and fusion using the surface forces apparatus". In: *Biophysical Journal* 77 (1999), pp. 1458–1468. DOI: 10.1016/S0006-3495(99)76993-6.

[33] P. Mühlenbrock et al. "Fusion pore formation observed during SNARE-mediated vesicle fusion with pore-spanning membranes". In: *Biophysical Journal* 119 (2020), pp. 151–161. DOI: 10.1016/j.bpj.2020.05.023.

[34] M. Doktorova et al. "Preparation of asymmetric phospholipid vesicles for use as cell membrane models". In: *Nature Protocols* 13 (2018), pp. 2086–2101. DOI: 10.1038/s41596-018-0033-6.

[35] O. López et al. “Kinetic studies of liposome solubilization by sodium dodecyl sulfate based on a dynamic light scattering technique”. In: *Langmuir* 14 (1998), pp. 4671–4674. DOI: 10.1021/la980219f.

[36] K. Komorowski et al. “Vesicle adhesion and fusion studied by small-angle X-ray scattering”. In: *Biophysical Journal* 114 (2018), pp. 1908–1920. DOI: 10.1016/j.bpj.2018.02.040.

[37] R. Dimova and C. M. Marques. *The giant vesicle book*. Boca Raton, FL: CRC Press, Taylor & Francis Group, 2020.

[38] R. Dimova. “Giant vesicles and their use in assays for assessing membrane phase state, curvature, mechanics, and electrical properties”. In: *Annual Review of Biophysics* 48 (2019), pp. 93–119. DOI: 10.1146/annurev-biophys-052118-115342.

[39] T. Robinson. “Microfluidic handling and analysis of giant vesicles for use as artificial cells: a review”. In: *Advanced Biosystems* 3 (2019), p. 1800318. DOI: 10.1002/adbi.201800318.

[40] R. R. M. Cavalcanti et al. “Efficient liposome fusion to phase-separated giant vesicles”. In: *Biophysical Journal* 122 (2023), pp. 2099–2111. DOI: 10.1016/j.bpj.2022.12.008.

[41] G. M. Whitesides. “The ’right’ size in nanobiotechnology”. In: *Nature Biotechnology* 21 (2003), pp. 1161–1165. DOI: 10.1038/nbt872.

[42] E. Roduner. “Size matters: why nanomaterials are different”. In: *Chemical Society Reviews* 35 (2006), p. 583. DOI: 10.1039/b502142c.

[43] A. P. Alivisatos. “Perspectives on the physical chemistry of semiconductor nanocrystals”. In: *The Journal of Physical Chemistry* 100 (1996), pp. 13226–13239. DOI: 10.1021/jp9535506.

[44] J. J. Giner-Casares et al. “Inorganic nanoparticles for biomedicine: where materials scientists meet medical research”. In: *Materials Today* 19 (2016), pp. 19–28. DOI: 10.1016/j.mattod.2015.07.004.

[45] M. De, P. S. Ghosh, and V. M. Rotello. “Applications of nanoparticles in biology”. In: *Advanced Materials* 20 (2008), pp. 4225–4241. DOI: 10.1002/adma.200703183.

[46] O. Salata. “Applications of nanoparticles in biology and medicine”. In: *Journal of Nanobiotechnology* 2 (2004), p. 3. DOI: 10.1186/1477-3155-2-3.

[47] J. Lin et al. “Understanding the synergistic effect of physicochemical properties of nanoparticles and their cellular entry pathways”. In: *Communications Biology* 3 (2020), p. 205. DOI: 10.1038/s42003-020-0917-1.

[48] R. A. Revia and M. Zhang. "Magnetite nanoparticles for cancer diagnosis, treatment, and treatment monitoring: recent advances". In: *Materials Today* 19 (2016), pp. 157–168. DOI: 10.1016/j.mattod.2015.08.022.

[49] M. R. Lewis and R. Kannan. "Development and applications of radioactive nanoparticles for imaging of biological systems". In: *WIREs Nanomedicine and Nanobiotechnology* 6 (2014), pp. 628–640. DOI: 10.1002/wnan.1292.

[50] J. A. Lemire, J. J. Harrison, and R. J. Turner. "Antimicrobial activity of metals: mechanisms, molecular targets and applications". In: *Nature Reviews Microbiology* 11 (2013), pp. 371–384. DOI: 10.1038/nrmicro3028.

[51] Y. Cai et al. "Phototherapy in cancer treatment: strategies and challenges". In: *Signal Transduction and Targeted Therapy* 10 (2025), p. 115. DOI: 10.1038/s41392-025-02140-y.

[52] M. Kim, J. H. Lee, and J. M. Nam. "Plasmonic photothermal nanoparticles for biomedical applications". In: *Advanced Science* 6 (2019). DOI: 10.1002/advs.201900471.

[53] D. Peer et al. "Nanocarriers as an emerging platform for cancer therapy". In: *Nature Nanotechnology* 2 (2007), pp. 751–760. DOI: 10.1038/nnano.2007.387.

[54] E. Blanco, H. Shen, and M. Ferrari. "Principles of nanoparticle design for overcoming biological barriers to drug delivery". In: *Nature Biotechnology* 33 (2015), pp. 941–951. DOI: 10.1038/nbt.3330.

[55] W. Zhang et al. "Effects of morphology and size of nanoscale drug carriers on cellular uptake and internalization process: a review". In: *RSC Advances* 13 (2023), pp. 80–114. DOI: 10.1039/D2RA06888E.

[56] E. C. Dreaden et al. "The golden age: gold nanoparticles for biomedicine". In: *Chem. Soc. Rev.* 41 (2012), pp. 2740–2779. DOI: 10.1039/C1CS15237H.

[57] H. Hadji and K. Bouchemal. "Effect of micro- and nanoparticle shape on biological processes". In: *Journal of Controlled Release* 342 (2022), pp. 93–110. DOI: 10.1016/j.jconrel.2021.12.032.

[58] K. S. Suhas et al. "A comprehensive review on nanoparticles: classification, properties, and mechanical effects". In: *Discover Materials* 6 (2025), p. 4. DOI: 10.1007/s43939-025-00455-9.

[59] C. A. Huang-Zhu and R. C. Van Lehn. "Engineering the nano-bio interface: challenges and opportunities for predicting the surface properties of monolayer-protected nanoparticles". In: *Materials Horizons* 12 (2025), pp. 6428–6439. DOI: 10.1039/D5MH00310E.

[60] Y. Wang and et al. "Surface engineering of nanoparticles for therapeutic delivery". In: *Chemical Society Reviews* 49 (2020), pp. 4623–4647. DOI: 10.1039/D0CS00287B.

[61] F. Zhao et al. “Cellular uptake, intracellular trafficking, and cytotoxicity of nanomaterials”. In: *Small* 7 (2011), pp. 1322–1337. DOI: 10.1002/smll.201100001.

[62] L. Shang, K. Nienhaus, and G. Ulrich Nienhaus. “Engineered nanoparticles interacting with cells: size matters”. In: *Journal of Nanobiotechnology* 12 (2014), p. 5. DOI: 10.1186/1477-3155-12-5.

[63] L. Y. T. Chou, K. Ming, and W. C. W. Chan. “Strategies for the intracellular delivery of nanoparticles”. In: *Chemical Society Reviews* 40 (2011), pp. 233–245. DOI: 10.1039/C0CS00003E.

[64] S. Zhang, H. Gao, and G. Bao. “Physical principles of nanoparticle cellular endocytosis”. In: *ACS Nano* 9 (2015), pp. 8655–8671. DOI: 10.1021/acsnano.5b03184.

[65] T. G. Iversen, T. Skotland, and K. Sandvig. “Endocytosis and intracellular transport of nanoparticles: Present knowledge and need for future studies”. In: *Nano Today* 6 (2011), pp. 176–185. DOI: 10.1016/j.nantod.2011.02.003.

[66] J. H. Park and N. Oh. “Endocytosis and exocytosis of nanoparticles in mammalian cells”. In: *International Journal of Nanomedicine* (2014), p. 51. DOI: 10.2147/IJN.S26592.

[67] S. Behzadi et al. “Cellular uptake of nanoparticles: journey inside the cell”. In: *Chemical Society Reviews* 46 (2017), pp. 4218–4244. DOI: 10.1039/C6CS00636A.

[68] S. Zhang et al. “Mechanistic insights into passive membrane permeability of drug-like molecules from a weighted ensemble of trajectories”. In: *Journal of Chemical Information and Modeling* 62 (2022), pp. 1891–1904. DOI: 10.1021/acs.jcim.1c01540.

[69] D. Pei and M. Buyanova. “Overcoming endosomal entrapment in drug delivery”. In: *Bioconjugate Chemistry* 30 (2019), pp. 273–283. DOI: 10.1021/acs.bioconjchem.8b00778.

[70] M. Sousa de Almeida et al. “Understanding nanoparticle endocytosis to improve targeting strategies in nanomedicine”. In: *Chemical Society Reviews* 50 (2021), pp. 5397–5434. DOI: 10.1039/D0CS01127D.

[71] Y. Roiter et al. “Interaction of lipid membrane with nanostructured surfaces”. In: *Langmuir* 25 (2009), pp. 6287–6299. DOI: 10.1021/la900119a.

[72] N. Javanmard, M. Sovizi, and M. Aliannezhadi. “Theoretical and experimental study into laser-induced gold nanoparticles for superior surface-enhanced raman spectroscopy applications”. In: *Scientific Reports* 15 (2025), p. 36781. DOI: 10.1038/s41598-025-20662-x.

[73] A. Verma and F. Stellacci. “Effect of surface properties on nanoparticle–cell interactions”. In: *Small* 6 (2010), pp. 12–21. DOI: 10.1002/smll.200901158.

[74] E. Canepa. *Nonspecific interactions of amphiphilic nanoparticles and biomimetic membranes*. Genoa, IT: University of Genoa, PhD thesis, 2021. DOI: https://dx.doi.org/10.15167/canepa-ester_phd2021-05-28.

[75] R. C. Van Lehn and A. Alexander-Katz. "Membrane-embedded nanoparticles induce lipid rearrangements similar to those exhibited by biological membrane proteins". In: *The Journal of Physical Chemistry B* 118 (2014), pp. 12586–12598. DOI: 10.1021/jp506239p.

[76] S. Salassi et al. "Au nanoparticles in lipid bilayers: a comparison between atomistic and coarse-grained models". In: *The Journal of Physical Chemistry C* 121 (2017), pp. 10927–10935. DOI: 10.1021/acs.jpcc.6b12148.

[77] S. Salassi et al. "Anionic nanoparticle-lipid membrane interactions: the protonation of anionic ligands at the membrane surface reduces membrane disruption". In: *RSC Advances* 9 (2019), pp. 13992–13997. DOI: 10.1039/C9RA02462J.

[78] P. E. G. Thorén et al. "Membrane binding and translocation of cell-penetrating peptides". In: *Biochemistry* 43 (2004), pp. 3471–3489. DOI: 10.1021/bi0360049.

[79] I. Ruseska and A. Zimmer. "Internalization mechanisms of cell-penetrating peptides". In: *Beilstein Journal of Nanotechnology* 11 (2020), pp. 101–123. DOI: 10.3762/bjnano.11.10.

[80] E. Canepa et al. "Amphiphilic gold nanoparticles: a biomimetic tool to gain mechanistic insights into peptide-lipid interactions". In: *Membranes* 12 (2022), p. 673. DOI: 10.3390/membranes12070673.

[81] R. C. Van Lehn et al. "Effect of particle diameter and surface composition on the spontaneous fusion of monolayer-protected gold nanoparticles with lipid bilayers". In: *Nano Letters* 13 (2013), pp. 4060–4067. DOI: 10.1021/nl401365n.

[82] R. C. Van Lehn and A. Alexander-Katz. "Pathway for insertion of amphiphilic nanoparticles into defect-free lipid bilayers from atomistic molecular dynamics simulations". In: *Soft Matter* 11 (2015), pp. 3165–3175. DOI: 10.1039/C5SM00287G.

[83] R. P. Carney et al. "Dynamic cellular uptake of mixed-monolayer protected nanoparticles". In: *Biointerphases* 7 (2012). DOI: 10.1007/s13758-011-0017-3.

[84] S. Sabella et al. "A general mechanism for intracellular toxicity of metal-containing nanoparticles". In: *Nanoscale* 6 (2014), p. 7052. DOI: 10.1039/c4nr01234h.

[85] P. U. Atukorale et al. "Influence of the glycocalyx and plasma membrane composition on amphiphilic gold nanoparticle association with erythrocytes". In: *Nanoscale* 7 (2015), pp. 11420–11432. DOI: 10.1039/C5NR01355K.

[86] S. T. Kim et al. "The role of surface functionality in determining nanoparticle cytotoxicity". In: *Accounts of Chemical Research* 46 (2013), pp. 681–691. DOI: 10.1021/ar3000647.

[87] E. Canepa et al. "Amphiphilic gold nanoparticles perturb phase separation in multidomain lipid membranes". In: *Nanoscale* 12 (2020), pp. 19746–19759. DOI: 10.1039/D0NR05366J.

[88] P. U. Atukorale et al. "Structure–property relationships of amphiphilic nanoparticles that penetrate or fuse lipid membranes". In: *Bioconjugate Chemistry* 29 (2018), pp. 1131–1140. DOI: 10.1021/acs.bioconjchem.7b00777.

[89] R. C. Van Lehn et al. "Lipid tail protrusions mediate the insertion of nanoparticles into model cell membranes". In: *Nature Communications* 5 (2014), p. 4482. DOI: 10.1038/ncomms5482.

[90] M. A. Tahir et al. "Calcium-triggered fusion of lipid membranes is enabled by amphiphilic nanoparticles". In: *Proceedings of the National Academy of Sciences* 117 (2020), pp. 18470–18476. DOI: 10.1073/pnas.1902597117.

[91] E. Canepa et al. "Cholesterol hinders the passive uptake of amphiphilic nanoparticles into fluid lipid membranes". In: *The Journal of Physical Chemistry Letters* 12 (2021), pp. 8583–8590. DOI: 10.1021/acs.jpclett.1c02077.

[92] E. Canepa et al. "Cholesterol-containing liposomes decorated with Au nanoparticles as minimal tunable tusion machinery". In: *Small* 19 (2023). DOI: 10.1002/smll.202207125.

[93] Y. Mély and G. Duportail. *Fluorescent methods to study biological membranes*. Berlin, Germany: Springer, 2013. DOI: 10.1007/978-3-642-33128-2.

[94] A. Kyrychenko. "Using fluorescence for studies of biological membranes: a review". In: *Methods and Applications in Fluorescence* 3 (2015), p. 042003. DOI: 10.1088/2050-6120/3/4/042003.

[95] F. M. Harris, K. B. Best, and J. D. Bell. "Use of laurdan fluorescence intensity and polarization to distinguish between changes in membrane fluidity and phospholipid order". In: *Biochimica et Biophysica Acta (BBA) - Biomembranes* 1565 (2002), pp. 123–128. DOI: 10.1016/S0005-2736(02)00514-X.

[96] N. Kahya and P. Schwille. "Fluorescence correlation studies of lipid domains in model membranes (Review)". In: *Molecular Membrane Biology* 23 (2006), pp. 29–39. DOI: 10.1080/09687860500489099.

[97] E. Sezgin and P. Schwille. "Fluorescence techniques to study lipid dynamics". In: *Cold Spring Harbor Perspectives in Biology* 3 (2011), a009803–a009803. DOI: 10.1101/cshperspect.a009803.

[98] M. Nakano et al. “FRET detects lateral interaction between transmembrane domain of EGF receptor and ganglioside GM3 in lipid bilayers”. In: *Biochimica et Biophysica Acta (BBA) - Biomembranes* 1863 (2021), p. 183623. DOI: 10.1016/j.bbamem.2021.183623.

[99] G. G. Stokes. “On the change of refrangibility of light”. In: *Philosophical Transactions of the Royal Society of London* 142 (1852), pp. 463–562.

[100] J. R. Lakowicz. *Principles of fluorescence spectroscopy*. Boston, MA: Springer US, 2006. DOI: 10.1007/978-0-387-46312-4.

[101] N. Duzgunes et al. “Lipid mixing during membrane aggregation and fusion: why fusion assays disagree”. In: *Biochemistry* 26 (1987), pp. 8435–8442. DOI: 10.1021/bi00399a061.

[102] R. B. Lira and R. Dimova. “Fusion assays for model membranes: a critical review”. In: *Advances in biomembranes and lipid self-assembly*. Elsevier, 2019. DOI: 10.1016/bs.abl.2019.09.003.

[103] L. Loura. “FRET in membrane biophysics: an overview”. In: *Frontiers in Physiology* 2 (2011). DOI: 10.3389/fphys.2011.00082.

[104] M. Kyoung et al. “Studying calcium-triggered vesicle fusion in a single vesicle-vesicle content and lipid-mixing system”. In: *Nature Protocols* 8 (2013), pp. 1–16. DOI: 10.1038/nprot.2012.134.

[105] Y. Lai et al. “Fusion pore formation and expansion induced by Ca^{2+} and synaptotagmin 1”. In: *Proceedings of the National Academy of Sciences* 110 (2013), pp. 1333–1338. DOI: 10.1073/pnas.1218818110.

[106] P. Mühlenbrock et al. “Fusion pore formation observed during SNARE-mediated vesicle fusion with pore-spanning membranes”. In: *Biophysical Journal* 119 (2020), pp. 151–161. DOI: 10.1016/j.bpj.2020.05.023.

[107] W. G. Cady. “The piezo-electric resonator”. In: *Proceedings of the IRE* 10 (1922), pp. 83–114. DOI: 10.1109/JRPROC.1922.219800.

[108] F. R. Lack, G. W. Willard, and I. E. Fair. “Some improvements in quartz crystal circuit elements”. In: *Bell System Technical Journal* 13 (1934), pp. 453–463. DOI: https://doi.org/10.1002/j.1538-7305.1934.tb00674.x.

[109] *Quartz Crystal Microbalance (QCM)*. 2026. URL: https://www.nanoscience.com/techniques/quartz-crystal-microbalance/.

[110] G. Liu and G. Zhang. “Basic principles of QCM-D”. In: *Quantitative Human Physiology*. 2013. DOI: 10.1007/978-3-642-39790-5_1.

[111] G. Sauerbrey. "Verwendung von schwingquarzen zur wogung donner schichten und zur mikrowogung". In: *Zeitschrift for Physik* 155 (1959), pp. 206–222. DOI: 10.1007/BF01337937.

[112] R. M. Mueller and W. White. "Direct gravimetric calibration of a quartz crystal microbalance". In: *Review of Scientific Instruments* 39 (1968), pp. 291–295. DOI: 10.1063/1.1683352.

[113] T. Nomura and M. Okuhara. "Frequency shifts of piezoelectric quartz crystals immersed in organic liquids". In: *Analytica Chimica Acta* 142 (1982), pp. 281–284. DOI: 10.1016/S0003-2670(01)95290-0.

[114] K. K. Kanazawa and J. G. Gordon. "The oscillation frequency of a quartz resonator in contact with liquid". In: *Analytica Chimica Acta* 175 (1985), pp. 99–105. DOI: 10.1016/S0003-2670(00)82721-X.

[115] S. Kurosawa et al. "Oscillating frequency of piezoelectric quartz crystal in solutions". In: *Analytica Chimica Acta* 230 (1990), pp. 41–49. DOI: 10.1016/S0003-2670(00)82759-2.

[116] M. Rodahl et al. "Quartz crystal microbalance setup for frequency and Q -factor measurements in gaseous and liquid environments". In: *Review of Scientific Instruments* 66 (1995), pp. 3924–3930. DOI: 10.1063/1.1145396.

[117] *What is QCM-D?* 2025. URL: https://www.biolinscientific.com/blog/what-is-qcmd.

[118] D. B. Murphy and M. W. Davidson. *Fundamentals of light microscopy and electronic imaging*. Hoboken, New Jersey: John Wiley & Sons, Inc., 2013.

[119] F. Zernike. "How I Discovered Phase Contrast". In: *Science* 121 (1955), pp. 345–349. DOI: 10.1126/science.121.3141.345.

[120] *Phase Contrast and Microscopy*. 2023. URL: https://www.leica-microsystems.com/science-lab/microscopy-basics/phase-contrast-and-microscopy/.

[121] F. Zernike. "The wave theory of microscopic image formation". In: *Concepts of classical optics*. W. H. Freeman and Co, 1958.

[122] E. Abbe. "Beiträge zur theorie des mikroskops und der mikroskopischen wahrnehmung". In: *Archiv für Mikroskopische Anatomie* 9 (1873), pp. 413–468. DOI: 10.1007/BF02956173.

[123] M. Minsky. "Memoir on inventing the confocal scanning microscope". In: *Scanning* 10 (1988), pp. 128–138. DOI: 10.1002/sca.4950100403.

[124] W. B. Amos and J. G. White. "How the confocal laser scanning microscope entered biological research". In: *Biology of the Cell* 95 (2003), pp. 335–342. DOI: 10.1016/S0248-4900(03)00078-9.

[125] J. B. Pawley. *Handbook of biological confocal microscopy*. New York, NY: Springer US, 2006.

[126] N. S. Claxton, T. J. Fellers, and M. W. Davidson. "Microscopy, Confocal". In: *Encyclopedia of Medical Devices and Instrumentation*. Wiley, 2006. DOI: 10.1002/0471732877.emd291.

[127] S. Da Vela and D. I. Svergun. "Methods, development and applications of small-angle X-ray scattering to characterize biological macromolecules in solution". In: *Current Research in Structural Biology* 2 (2020), pp. 164–170. DOI: 10.1016/j.crstbi.2020.08.004.

[128] T. Li, A. J. Senesi, and B. Lee. "Small angle X-ray scattering for nanoparticle research". In: *Chemical Reviews* 116 (2016), pp. 11128–11180. DOI: 10.1021/acs.chemrev.5b00690.

[129] M. Sakuragi. "Evaluation of the supramolecular structure of drug delivery carriers using synchrotron X-ray scattering". In: *Polymer Journal* 53 (2021), pp. 1335–1344. DOI: 10.1038/s41428-021-00533-8.

[130] Y. Sun et al. "Recent advances in structural characterization of biomacromolecules in foods via small-angle X-ray scattering". In: *Frontiers in Nutrition* 9 (2022). DOI: 10.3389/fnut.2022.1039762.

[131] M. Gräwert and D. Svergun. "A beginner's guide to solution small-angle X-ray scattering (SAXS)". In: *The Biochemist* 42 (2020), pp. 36–42. DOI: 10.1042/BIO04201036.

[132] A. Guinier and G. Fournet. *Small-angle scattering of X-rays*. New York: John Wiley & Sons, Inc., 1955.

[133] I. Pilz, O. Glatter, and O. Kratky. "Small-angle x-ray scattering". In: Academic Press, 1979. DOI: 10.1016/0076-6879(79)61013-3.

[134] A. Einstein. *Investigations on the theory of the brownian movement*. English translation by R. Fürth. Mineola, NY: Dover Publications, 1956.

[135] Malvern Instruments. *Zetasizer Nano User Manual*. MAN0317. 2009.

[136] B. J. Berne and R. Pecora. *Dynamic light scattering: with applications to chemistry, biology, and physics*. New York, NY: Wiley, 1976.

[137] A. J. F. Siegert. *On the fluctuations in signals returned by many independently moving scatterers*. Tech. rep. Radiation Laboratory, Massachusetts Institute of Technology, 1943.

[138] G. Mie. "Beiträge zur Optik trüber Medien, speziell kolloidaler Metallösungen". In: *Annalen der Physik* 330 (1908), pp. 377–445. DOI: https://doi.org/10.1002/andp.19083300302.

[139] *Calculating volume distributions from dynamic light scattering data*. 2017. URL: https://www.materials-talks.com/wp-content/uploads/2017/01/FAQ-Calculating-volume-distributions-from-DLS-data.pdf.

[140] R. J. Hunter. *Zeta potential in colloid science: principles and applications*. Cambridge, MA, USA: Academic Press, 1981.

[141] A. V. Delgado et al. "Measurement and interpretation of electrokinetic phenomena (IUPAC technical report)". In: *Pure and Applied Chemistry* 77 (2005), pp. 1753–1805. DOI: 10.1351/pac200577101753.

[142] F. Durst. "Studies of particle motion by laser doppler techniques". In: *Proceedings of the dynamic flow conference 1978 on dynamic measurements in unsteady flows*. Springer Netherlands, 1978. DOI: 10.1007/978-94-009-9565-9_19.

[143] B. Leonardini et al. "Physical determinants of nanoparticle-mediated lipid membrane fusion". In: *Nanoscale* 17 (2025), pp. 8923–8932. DOI: 10.1039/D4NR04851B.

[144] R. Jahn, T. Lang, and T. C. Südhof. "Membrane Fusion". In: *Cell* 112 (2003), pp. 519–533. DOI: 10.1016/S0092-8674(03)00112-0.

[145] R. Jahn and T. C. Südhof. "Membrane fusion and exocytosis". In: *Annual Review of Biochemistry* 68 (1999), pp. 863–911. DOI: 10.1146/annurev.biochem.68.1.863.

[146] J. Rizo and C. Rosenmund. "Synaptic vesicle fusion". In: *Nature Structural & Molecular Biology* 15 (2008), pp. 665–674. DOI: 10.1038/nsmb.1450.

[147] D. G. Myles. "Molecular mechanisms of sperm-egg membrane binding and fusion in mammals". In: *Developmental Biology* 158 (1993), pp. 35–45. DOI: 10.1006/dbio.1993.1166.

[148] D. M. Eckert and P. S. Kim. "Mechanisms of viral membrane fusion and its inhibition". In: *Annual Review of Biochemistry* 70 (2001), pp. 777–810. DOI: 10.1146/annurev.biochem.70.1.777.

[149] F. Mazur and R. Chandrawati. "Membrane fusion models for bioapplications". In: *ChemNanoMat* 7 (2021), pp. 223–237. DOI: 10.1002/cnma.202000582.

[150] N. T. Ho et al. "Membrane fusion and drug delivery with carbon nanotube porins". In: *Proceedings of the National Academy of Sciences* 118 (2021). DOI: 10.1073/pnas.2016974118.

[151] Y. Zeng et al. "Enhanced liposomal drug delivery via membrane fusion triggered by dimeric coiled-coil peptides". In: *Small* 19 (2023). DOI: 10.1002/smll.202301133.

[152] L. V. Chernomordik and M. M. Kozlov. "Mechanics of membrane fusion". In: *Nature Structural & Molecular Biology* 15 (2008), pp. 675–683. DOI: 10.1038/nsmb.1455.

[153] B. Leonardini et al. “Understanding, mimicking, and exploiting lipid membrane fusion in biomedicine and synthetic biology”. In: *Advances in Physics: X* 11 (2026). DOI: 10.1080/23746149.2026.2636806.

[154] S. Martens and H. T. McMahon. “Mechanisms of membrane fusion: disparate players and common principles”. In: *Nature Reviews Molecular Cell Biology* 9 (2008), pp. 543–556. DOI: 10.1038/nrm2417.

[155] R. Jahn and R. H. Scheller. “SNAREs — engines for membrane fusion”. In: *Nature Reviews Molecular Cell Biology* 7 (2006), pp. 631–643. DOI: 10.1038/nrm2002.

[156] S. Martens, M. M. Kozlov, and H. T. McMahon. “How synaptotagmin promotes membrane fusion”. In: *Science* 316 (2007), pp. 1205–1208. DOI: 10.1126/science.1142614.

[157] R. Jahn, D. C. Cafiso, and L. K. Tamm. “Mechanisms of SNARE proteins in membrane fusion”. In: *Nature Reviews Molecular Cell Biology* 25 (2024), pp. 101–118. DOI: 10.1038/s41580-023-00668-x.

[158] L. Yang and H. W. Huang. “Observation of a Membrane Fusion Intermediate Structure”. In: *Science* 297 (2002), pp. 1877–1879. DOI: 10.1126/science.1074354.

[159] R. B. Lira et al. “The underlying mechanical properties of membranes tune their ability to fuse”. In: *Journal of Biological Chemistry* 299 (2023), p. 105430. DOI: 10.1016/j.jbc.2023.105430.

[160] S. T. Yang et al. “HIV gp41–mediated membrane fusion occurs at edges of cholesterol-rich lipid domains”. In: *Nature Chemical Biology* 11 (2015), pp. 424–431. DOI: 10.1038/nchembio.1800.

[161] S. T. Yang, V. Kiessling, and L. K. Tamm. “Line tension at lipid phase boundaries as driving force for HIV fusion peptide-mediated fusion”. In: *Nature Communications* 7 (2016), p. 11401. DOI: 10.1038/ncomms11401.

[162] S. T. Yang et al. “HIV virions sense plasma membrane heterogeneity for cell entry”. In: *Science Advances* 3 (2017). DOI: 10.1126/sciadv.1700338.

[163] C. S. Poojari, K. C. Scherer, and Jochen S. Hub. “Free energies of membrane stalk formation from a lipidomics perspective”. In: *Nature Communications* 12 (2021), p. 6594. DOI: 10.1038/s41467-021-26924-2.

[164] M. Accorsi et al. “Protein-free membrane fusion: a refined view of the delicate fusogenic properties of calcium”. In: *Biophysical Journal* (2026). DOI: 10.1016/j.bpj.2026.03.040.

[165] K. Stebelska, P. M. Dubielecka, and A. F. Sikorski. "The effect of PS content on the ability of natural membranes to fuse with positively charged liposomes and lipoplexes". In: *Journal of Membrane Biology* 206 (2005), pp. 203–214. DOI: 10.1007/s00232-005-0793-0.

[166] R. B. Lira et al. "Highly efficient protein-free membrane fusion: a giant vesicle study". In: *Biophysical Journal* 116 (2019), pp. 79–91. DOI: 10.1016/j.bpj.2018.11.3128.

[167] J. Wilschut and D. Papahadjopoulos. "Ca^{2+}-induced fusion of phospholipid vesicles monitored by mixing of aqueous contents". In: *Nature* 281 (1979), pp. 690–692. DOI: 10.1038/281690a0.

[168] N. Düzgünes et al. "Studies on the mechanism of membrane fusion. Role of head-group composition in calcium- and magnesium-induced fusion of mixed phospholipid vesicles". In: *Biochimica et Biophysica Acta (BBA)-Biomembranes* 642 (1981), pp. 182–195. DOI: 10.1016/0005-2736(81)90148-6.

[169] D. L. Floyd et al. "Single-particle kinetics of influenza virus membrane fusion". In: *Proceedings of the National Academy of Sciences* 105 (2008), pp. 15382–15387. DOI: 10.1073/pnas.0807771105.

[170] D. A. Costello et al. "Influenza virus-membrane fusion triggered by proton uncaging for single particle studies of fusion kinetics". In: *Analytical Chemistry* 84 (2012), pp. 8480–8489. DOI: 10.1021/ac3006473.

[171] Z. Zhang and M. B. Jackson. "Temperature dependence of fusion kinetics and fusion pores in Ca^{2+}-triggered exocytosis from PC12 Cells". In: *The Journal of General Physiology* 131 (2008), pp. 117–124. DOI: 10.1085/jgp.200709891.

[172] J. Dufloo and R. Sanjuán. "Temperature impacts SARS-CoV-2 spike fusogenicity and evolution". In: *mBio* 15 (2024). DOI: 10.1128/mbio.03360-23.

[173] M. Ma and D. Bong. "Controlled fusion of synthetic lipid membrane vesicles". In: *Accounts of Chemical Research* 46 (2013), pp. 2988–2997. DOI: 10.1021/ar400065m.

[174] G. A. Daudey et al. "Liposome fusion with orthogonal coiled coil peptides as fusogens: The efficacy of roleplaying peptides". In: *Chemical Science* 12 (2021), pp. 13782–13792. DOI: 10.1039/d0sc06635d.

[175] A. Rabe et al. "Programmable fusion of liposomes mediated by lipidated PNA". In: *Chemical Communications* 53 (2017), pp. 11921–11924. DOI: 10.1039/c7cc06058k.

[176] P. M. G. Löffler et al. "Lipidated polyaza crown ethers as membrane anchors for DNA-controlled content mixing between liposomes". In: *Scientific Reports* 9 (2019). DOI: 10.1038/s41598-019-49862-y.

[177] P. M. G. Löffler, O. Ries, and Stefan Vogel. "DNA-mediated liposome fusion observed by fluorescence spectrometry". In: *Nucleic acid detection and structuralinvestigations*. Springer, 2020. DOI: 10.1007/978-1-0716-0138-9_9.

[178] D. Mukherjee et al. "Polyethylene glycol-mediated fusion of extracellular vesicles with cationic liposomes for the design of hybrid delivery systems". In: *ACS Applied Bio Materials* 4 (2021), pp. 8259–8266. DOI: 10.1021/acsabm.1c00804.

[179] N. Marušič et al. "Fusion-induced growth of biomimetic polymersomes: behavior of poly(dimethylsiloxane)-poly(ethylene oxide) vesicles in saline solutions under high agitation". In: *Macromolecular Rapid Communications* 43 (2022). DOI: 10.1002/marc.202100712.

[180] A. Rørvig-Lund et al. "Vesicle fusion triggered by optically heated gold nanoparticles". In: *Nano Letters* 15 (2015), pp. 4183–4188. DOI: 10.1021/acs.nanolett.5b01366.

[181] A. Bahadori, L. B. Oddershede, and P. M. Bendix. "Hot-nanoparticle-mediated fusion of selected cells". In: *Nano Research* 10 (2017), pp. 2034–2045. DOI: 10.1007/s12274-016-1392-3.

[182] M. Arribas Perez and P. A. Beales. "Biomimetic curvature and tension-driven membrane fusion induced by silica nanoparticles". In: *Langmuir* 37 (2021), pp. 13917–13931. DOI: 10.1021/acs.langmuir.1c02492.

[183] G. Brosio, G. Rossi, and D. Bochicchio. "Nanoparticle-induced biomembrane fusion: unraveling the effect of core size on stalk formation". In: *Nanoscale Advances* 5 (2023), pp. 4675–4680. DOI: 10.1039/d3na00430a.

[184] S. Blasco, L. Sukeník, and R. Vácha. "Nanoparticle induced fusion of lipid membranes". In: *Nanoscale* 16 (2024), pp. 10221–10229. DOI: 10.1039/D4NR00591K.

[185] C. A. Keller and B. Kasemo. "Surface specific kinetics of lipid vesicle adsorption measured with a quartz crystal microbalance". In: *Biophysical Journal* 75 (1998), pp. 1397–1402. DOI: 10.1016/S0006-3495(98)74057-3.

[186] F. Mashali et al. "Simultaneous electrophysiology and imaging reveal changes in lipid membrane thickness and tension upon uptake of amphiphilic gold nanoparticles". In: *Langmuir* 39 (2023), pp. 15031–15045. DOI: 10.1021/acs.langmuir.3c01973.

[187] S. J. Marrink et al. "The MARTINI force field: c oarse grained model for biomolecular simulations". In: *The Journal of Physical Chemistry B* 111 (2007), pp. 7812–7824. DOI: 10.1021/jp071097f.

[188] J. Kästner. "Umbrella sampling". In: *WIREs computational molecular science* 1 (2011), pp. 932–942. DOI: 10.1002/wcms.66.

[189] F. G. Strobl et al. “Intake of silica nanoparticles by giant lipid vesicles: influence of particle size and thermodynamic membrane state”. In: *Beilstein Journal of Nanotechnology* 5 (2014), pp. 2468–2478. DOI: 10.3762/bjnano.5.256.

[190] A. Azadbakht et al. “Wrapping pathways of anisotropic dumbbell particles by giant unilamellar vesicles”. In: *Nano Letters* 23 (2023), pp. 4267–4273. DOI: 10.1021/acs.nanolett.3c00375.

[191] M. M. Sirch et al. “Phase-state-dependent silica nanoparticle uptake of giant unilamellar vesicles”. In: *The Journal of Physical Chemistry B* 128 (2024), pp. 7172–7179. DOI: 10.1021/acs.jpcb.4c02383.

[192] L. Wang and N. Malmstadt. “Interactions between charged nanoparticles and giant vesicles fabricated from inverted-headgroup lipids”. In: *Journal of Physics D: Applied Physics* 50 (2017), p. 415402. DOI: 10.1088/1361-6463/aa86e6.

[193] M. Karimi et al. “Asymmetric ionic conditions generate large membrane curvatures”. In: *Nano Letters* 18 (2018), pp. 7816–7821. DOI: 10.1021/acs.nanolett.8b03584.

[194] M. A. S. Karal et al. “Deformation and poration of giant unilamellar vesicles induced by anionic nanoparticles”. In: *Chemistry and Physics of Lipids* 230 (2020), p. 104916. DOI: 10.1016/j.chemphyslip.2020.104916.

[195] S. Akter et al. “Effects of cholesterol on the anionic magnetite nanoparticle-induced deformation and poration of giant lipid vesicles”. In: *RSC Advances* 12 (2022), pp. 28283–28294. DOI: 10.1039/D2RA03199J.

[196] S. Li and N. Malmstadt. “Deformation and poration of lipid bilayer membranes by cationic nanoparticles”. In: *Soft Matter* 9 (2013), p. 4969. DOI: 10.1039/c3sm27578g.

[197] L. Wang et al. “Effect of protein corona on nanoparticle–plasma membrane and nanoparticle–biomimetic membrane interactions”. In: *Environmental Science: Nano* 7 (2020), pp. 963–974. DOI: 10.1039/D0EN00035C.

[198] R. Chairil and N. Malmstadt. “Curvature preference of cubic CsPbBr 3 quantum dots embedded onto phospholipid bilayer membranes”. In: *Soft Matter* 19 (2023), pp. 3966–3974. DOI: 10.1039/D3SM00409K.

[199] E. Ewins et al. “Poly(ionic liquid) nanoparticles selectively disrupt biomembranes”. In: *Advanced Science* 6 (2019). DOI: 10.1002/advs.201801602.

[200] X. Wei et al. “Effect of silica nanoparticles on cell membrane fluidity: The role of temperature and membrane composition”. In: *Science of The Total Environment* 838 (2022), p. 156552. DOI: 10.1016/j.scitotenv.2022.156552.

[201] A. Elbaradei et al. “Interaction of polymer-coated silicon nanocrystals with lipid bilayers and surfactant interfaces”. In: *Physical Review E* 94 (2016), p. 042804. DOI: 10.1103/PhysRevE.94.042804.

[202] Y. Yu and S. Granick. "Pearling of lipid vesicles induced by nanoparticles". In: *Journal of the American Chemical Society* 131 (2009), pp. 14158–14159. DOI: 10.1021/ja905900h.

[203] P. B. Santhosh et al. "Influence of nanoparticle–membrane electrostatic interactions on membrane fluidity and bending elasticity". In: *Chemistry and Physics of Lipids* 178 (2014), pp. 52–62. DOI: 10.1016/j.chemphyslip.2013.11.009.

[204] I. U. Foreman-Ortiz et al. "Anionic nanoparticle-induced perturbation to phospholipid membranes affects ion channel function". In: *Proceedings of the National Academy of Sciences* 117 (2020), pp. 27854–27861. DOI: 10.1073/pnas.2004736117.

[205] M. Arribas Perez et al. "Mechanomodulation of Lipid Membranes by Weakly Aggregating Silver Nanoparticles". In: *Biochemistry* 58 (2019), pp. 4761–4773. DOI: 10.1021/acs.biochem.9b00390.

[206] S. Zuraw-Weston et al. "Nanoparticles binding to lipid membranes: from vesicle-based gels to vesicle tubulation and destruction". In: *Nanoscale* 11 (2019), pp. 18464–18474. DOI: 10.1039/C9NR06570A.

[207] J. T. Wiemann et al. "Membrane poration, wrinkling, and compression: deformations of lipid vesicles induced by amphiphilic Janus nanoparticles". In: *Nanoscale* 12 (2020), pp. 20326–20336. DOI: 10.1039/D0NR05355D.

[208] R. Dimova and K. A. Riske. "Electrodeformation, electroporation, and electrofusion of giant unilamellar vesicles". In: *Handbook of Electroporation*. Springer, 2016. DOI: 10.1007/978-3-319-26779-1_199-1.

[209] M. I. Angelova and D. S. Dimitrov. "Liposome electroformation". In: *Faraday Discussions of the Chemical Society* 81 (1986), p. 303. DOI: 10.1039/dc9868100303.

[210] J. Steinkühler et al. "Charged giant unilamellar vesicles prepared by electroformation exhibit nanotubes and transbilayer lipid asymmetry". In: *Scientific Reports* 8 (2018), p. 11838. DOI: 10.1038/s41598-018-30286-z.

[211] E. Lavagna et al. "Amphiphilic nanoparticles generate curvature in lipid membranes and shape liposome–liposome interfaces". In: *Nanoscale* 13 (2021), pp. 16879–16884. DOI: 10.1039/D1NR05067B.

[212] R. Dasgupta et al. "The glycolipid GM1 reshapes asymmetric biomembranes and giant vesicles by curvature generation". In: *Proceedings of the National Academy of Sciences* 115 (2018), pp. 5756–5761. DOI: 10.1073/pnas.1722320115.

[213] F. Yuan et al. "The ins and outs of membrane bending by intrinsically disordered proteins". In: *Science Advances* 9 (2023). DOI: 10.1126/sciadv.adg3485.

[214] B. Alberts et al. *Molecular biology of the cell*. New York, NY: W. W. Northon & Co, 2015.

[215] R. Phillips et al. *Physical biology of the cell*. New York, NY: Garland Science, 2009.

[216] E. Bremer and R. Krämer. "Responses of Microorganisms to Osmotic Stress". In: *Annual Review of Microbiology* 73 (2019), pp. 313–334. DOI: 10.1146/annurev-micro-020518-115504.

[217] H. Wennerström et al. "Colloidal stability of the living cell". In: *Proceedings of the National Academy of Sciences* 117 (2020), pp. 10113–10121. DOI: 10.1073/pnas.1914599117.

[218] A. D. Bangham, J. De Gier, and G. D. Greville. "Osmotic properties and water permeability of phospholipid liquid crystals". In: *Chemistry and Physics of Lipids* 1 (1967), pp. 225–246. DOI: 10.1016/0009-3084(67)90030-8.

[219] B. L. Mui et al. "Osmotic properties of large unilamellar vesicles prepared by extrusion". In: *Biophysical Journal* 64 (1993), pp. 443–453. DOI: 10.1016/S0006-3495(93)81385-7.

[220] S. Paula et al. "Permeation of protons, potassium ions, and small polar molecules through phospholipid bilayers as a function of membrane thickness". In: *Biophysical Journal* 70 (1996), pp. 339–348. DOI: 10.1016/S0006-3495(96)79575-9.

[221] J. Pencer, G. F. White, and F. Ross Hallett. "Osmotically induced shape changes of large unilamellar vesicles measured by dynamic light scattering". In: *Biophysical Journal* 81 (2001), pp. 2716–2728. DOI: 10.1016/S0006-3495(01)75914-0.

[222] A. Carruthers and D. L. Melchior. "Study of the relationship between bilayer water permeability and bilayer physical state". In: *Biochemistry* 22 (1983), pp. 5797–5807. DOI: 10.1021/bi00294a018.

[223] M. Sugita et al. "Lipid composition is critical for accurate membrane permeability prediction of cyclic peptides by molecular dynamics simulations". In: *Journal of Chemical Information and Modeling* 62 (2022), pp. 4549–4560. DOI: 10.1021/acs.jcim.2c00931.

[224] X. Liu et al. "Vesicles balance osmotic stress with bending energy that can be released to form daughter vesicles". In: *The Journal of Physical Chemistry Letters* 13 (2022), pp. 498–507. DOI: 10.1021/acs.jpclett.1c03369.

[225] T. Bhatia, T. Robinson, and Ru. Dimova. "Membrane permeability to water measured by microfluidic trapping of giant vesicles". In: *Soft Matter* 16 (2020), pp. 7359–7369. DOI: 10.1039/D0SM00155D.

[226] W. Zhang et al. "Spatiotemporal measurement of osmotic pressures by FRET imaging". In: *Angewandte Chemie International Edition* 60 (2021), pp. 6488–6495. DOI: 10.1002/anie.202011983.

[227] J. Frallicciardi et al. “Membrane thickness, lipid phase and sterol type are determining factors in the permeability of membranes to small solutes”. In: *Nature Communications* 13 (2022), p. 1605. DOI: 10.1038/s41467-022-29272-x.

[228] Y. Levin and M. A. Idiart. “Pore dynamics of osmotically stressed vesicles”. In: *Physica A: Statistical Mechanics and its Applications* 331 (2004), pp. 571–578. DOI: 10.1016/j.physa.2003.05.001.

[229] A. Torchi et al. “Local enhancement of lipid membrane permeability induced by irradiated gold nanoparticles”. In: *ACS Nano* 11 (2017), pp. 12553–12561. DOI: 10.1021/acsnano.7b06690.

[230] P. A. Oroskar, C. J. Jameson, and S. Murad. “Surface-functionalized nanoparticle permeation triggers lipid displacement and water and ion leakage”. In: *Langmuir* 31 (2015), pp. 1074–1085. DOI: 10.1021/la503934c.

[231] M. C. Blok, L. L. M. van Deenen, and J. de Gier. “Effect of the gel to liquid crystalline phase transition on the osmotic behaviour of phosphatidycholine liposomes”. In: *Biochimica et Biophysica Acta (BBA) - Biomembranes* 433 (1976), pp. 1–12. DOI: 10.1016/0005-2736(76)90172-3.

[232] A. Piccinini et al. “The effect of phosphate buffered saline and osmotic stress on phosphatidylcholine vesicles”. In: *Journal of Colloid and Interface Science* 691 (2025), p. 137363. DOI: 10.1016/j.jcis.2025.137363.

[233] W. Zong et al. “Deformation of giant unilamellar vesicles under osmotic stress”. In: *Colloids and Surfaces B: Biointerfaces* 172 (Dec. 2018), pp. 459–463. DOI: 10.1016/j.colsurfb.2018.08.053.

[234] R. E. Wood, F. P. Wirth, and H. E. Morgan. “Glucose permeability of lipid bilayer membranes”. In: *Biochimica et Biophysica Acta (BBA) - Biomembranes* 163 (1968), pp. 171–178. DOI: 10.1016/0005-2736(68)90095-3.

[235] K. Olbrich et al. “Water Permeability and Mechanical Strength of Polyunsaturated Lipid Bilayers”. In: *Biophysical Journal* 79 (2000), pp. 321–327. DOI: 10.1016/S0006-3495(00)76294-1.

[236] J. de Gier. “Osmotic behaviour and permeability properties of liposomes”. In: *Chemistry and Physics of Lipids* 64 (1993), pp. 187–196. DOI: 10.1016/0009-3084(93)90065-B.

[237] B. Lerebours, E. Wehrli, and H. Hauser. “Thermodynamic stability and osmotic sensitivity of small unilamellar phosphatidylcholine vesicles”. In: *Biochimica et Biophysica Acta (BBA) - Biomembranes* 1152 (Oct. 1993), pp. 49–60. DOI: 10.1016/0005-2736(93)90230-W.

[238] A. Maiti and S. Daschakraborty. "Effect of TMAO on the structure and phase transition of lipid membranes: potential role of TMAO in stabilizing cell membranes under osmotic stress". In: *The Journal of Physical Chemistry B* 125 (2021), pp. 1167–1180. DOI: 10.1021/acs.jpcb.0c08335.

[239] S. Yamazaki et al. "Osmotic pressure-induced lipid membrane phase separation within macromolecular environments". In: *The Journal of Physical Chemistry B* 130 (2026), pp. 2157–2163. DOI: 10.1021/acs.jpcb.5c07221.

[240] R. Whiting et al. "Hypo-osmotic stress and pore-forming toxins adjust the lipid order in sheep red blood cell membranes". In: *Membranes* 13 (2023), p. 620. DOI: 10.3390/membranes13070620.

[241] K. J. Seu. "Osmotic stressing, membrane leakage, and fluorescence: an introductory biochemistry demonstration". In: *Journal of Chemical Education* 92 (2015), pp. 1522–1525. DOI: 10.1021/acs.jchemed.5b00023.

[242] E. Zapata-Mercado, E. V. Azarova, and K. Hristova. "Effect of osmotic stress on live cell plasma membranes, probed via Laurdan general polarization measurements". In: *Biophysical Journal* 121 (2022), pp. 2411–2418. DOI: 10.1016/j.bpj.2022.05.016.

[243] M. Doktorova, J. L. Symons, and I. Levental. "Structural and functional consequences of reversible lipid asymmetry in living membranes". In: *Nature Chemical Biology* 16 (2020), pp. 1321–1330. DOI: 10.1038/s41589-020-00688-0.

[244] I. S. Oliveira et al. "The Importance of bilayer asymmetry in biological membranes: insights from model membranes". In: *Membranes* 15 (2025), p. 79. DOI: 10.3390/membranes15030079.

[245] E. A. Cino and D. P. Tieleman. "Curvature-based sorting of eight lipid types in asymmetric buckled plasma membrane models". In: *Biophysical Journal* 121 (2022), pp. 2060–2068. DOI: 10.1016/j.bpj.2022.05.002.

[246] J. D. Perlmutter and J. N. Sachs. "Interleaflet interaction and asymmetry in phase separated lipid bilayers: molecular dynamics simulations". In: *Journal of the American Chemical Society* 133 (2011), pp. 6563–6577. DOI: 10.1021/ja106626r.

[247] E. London. "Ordered domain (raft) formation in asymmetric vesicles and its induction upon Loss of lipid asymmetry in artificial and natural membranes". In: *Membranes* 12 (2022). DOI: 10.3390/membranes12090870.

[248] J. M. Machin et al. "Protein–lipid charge interactions control the folding of outer membrane proteins into asymmetric membranes". In: *Nature Chemistry* 15 (2023), pp. 1754–1764. DOI: 10.1038/s41557-023-01319-6.

[249] O. Farago. "Measuring the mechanical properties of asymmetric membranes in computer simulations — new methods and insights". In: *Faraday Discussions* 259 (2025), pp. 321–341. DOI: 10.1039/D4FD00182F.

[250] L. Lu et al. "Membrane mechanical properties of synthetic asymmetric phospholipid vesicles". In: *Soft Matter* 12 (2016), pp. 7521–7528. DOI: 10.1039/C6SM01349J.

[251] Y. Elani et al. "Measurements of the effect of membrane asymmetry on the mechanical properties of lipid bilayers". In: *Chemical Communications* 51 (2015), pp. 6976–6979. DOI: 10.1039/C5CC00712G.

[252] R. F. Vázquez et al. "Asymmetric bilayers mimicking membrane rafts prepared by lipid exchange: Nanoscale characterization using AFM-Force spectroscopy". In: *Biochimica et Biophysica Acta (BBA) - Biomembranes* 1863 (2021), p. 183467. DOI: 10.1016/j.bbamem.2020.183467.

[253] D. Marquardt, B. Geier, and G. Pabst. "Asymmetric lipid membranes: towards more realistic model systems". In: *Membranes* 5 (2015), pp. 180–196. DOI: 10.3390/membranes5020180.

[254] M. Caputo et al. "Lipid asymmetry and membrane trafficking: Transbilayer distribution of structural phospholipids as regulators of exocytosis and endocytosis". In: *Journal of Biological Chemistry* 301 (2025), p. 110441. DOI: 10.1016/j.jbc.2025.110441.

[255] G. Pabst and S. Keller. "Exploring membrane asymmetry and its effects on membrane proteins". In: *Trends in Biochemical Sciences* 49 (2024), pp. 333–345. DOI: 10.1016/j.tibs.2024.01.007.

[256] S. M. Van den Eijnde et al. "Phosphatidylserine plasma membrane asymmetry in vivo: a pancellular phenomenon which alters during apoptosis". In: *Cell Death & Differentiation* 4 (1997), pp. 311–316. DOI: 10.1038/sj.cdd.4400241.

[257] N. M. Rysavy et al. "Beyond apoptosis: the mechanism and function of phosphatidylserine asymmetry in the membrane of activating mast cells". In: *BioArchitecture* 4 (2014), pp. 127–137. DOI: 10.1080/19490992.2014.995516.

[258] D. Tong et al. "Phosphatidylserine-exposing blood and endothelial cells contribute to the hypercoagulable state in essential thrombocythemia patients". In: *Annals of Hematology* 97 (2018), pp. 605–616. DOI: 10.1007/s00277-018-3228-6.

[259] I. M. Kur and A. Weigert. "Phosphatidylserine externalization as immune checkpoint in cancer". In: *Pflügers Archiv - European Journal of Physiology* 476 (2024), pp. 1789–1802. DOI: 10.1007/s00424-024-02948-7.

[260] A. Amara and J. Mercer. "Viral apoptotic mimicry". In: *Nature Reviews Microbiology* 13 (2015), pp. 461–469. DOI: 10.1038/nrmicro3469.

[261] M. H. L. Nguyen et al. “Peptide-Induced Lipid Flip-Flop in Asymmetric Liposomes Measured by Small Angle Neutron Scattering”. In: *Langmuir* 35 (2019), pp. 11735–11744. DOI: 10.1021/acs.langmuir.9b01625.

[262] J. M. Machin, N. A. Ranson, and S. E. Radford. “Protein-induced membrane asymmetry modulates OMP folding kinetics and stability”. In: *Faraday Discussions* 259 (2025), pp. 579–596. DOI: 10.1039/D4FD00180J.

[263] J. Ji and E. Lyman. “Lipid–GPCR interactions in an asymmetric plasma membrane model”. In: *Faraday Discussions* 259 (2025), pp. 545–558. DOI: 10.1039/D4FD00210E.

[264] L. Ou et al. “Atomistic Simulations on Interactions between Amphiphilic Janus Nanoparticles and Lipid Bilayers: Effects of Lipid Ordering and Leaflet Asymmetry”. In: *The Journal of Physical Chemistry B* 124 (2020), pp. 4466–4475. DOI: 10.1021/acs.jpcb.9b11989.

[265] P. Bigdelou et al. “Loss of membrane asymmetry alters the interactions of erythrocytes with engineered silica nanoparticles”. In: *Biointerphases* 15 (2020). DOI: 10.1116/6.0000246.

[266] Y. Zhang and J. Lou. “Impact of lipid asymmetry on membrane biophysical properties: Insights from molecular dynamics simulations”. In: *Quantitative Biology* 13 (2025). DOI: 10.1002/qub2.89.

[267] J. M. Crane, V. Kiessling, and L. K. Tamm. “Measuring lipid asymmetry in planar supported bilayers by fluorescence interference contrast microscopy”. In: *Langmuir* 21 (2005), pp. 1377–1388. DOI: 10.1021/la047654w.

[268] P. C. Hu, S. Li, and N. Malmstadt. “Microfluidic fabrication of asymmetric giant lipid vesicles”. In: *ACS Applied Materials & Interfaces* 3 (2011), pp. 1434–1440. DOI: 10.1021/am101191d.

[269] K. Karamdad et al. “Studying the effects of asymmetry on the bending rigidity of lipid membranes formed by microfluidics”. In: *Chemical Communications* 52 (2016), pp. 5277–5280. DOI: 10.1039/C5CC10307J.

[270] L. R. Arriaga et al. “Single-step assembly of asymmetric vesicles”. In: *Lab on a Chip* 19 (2019), pp. 749–756. DOI: 10.1039/C8LC00882E.

[271] D. Mion et al. “Biomimetic membrane in a microfluidic chip for the electrical and optical monitoring of biological reactions”. In: *Nature Protocols* 20 (2025), pp. 3477–3508. DOI: 10.1038/s41596-025-01171-7.

[272] M. J. Hope et al. “Phospholipid asymmetry in large unilamellar vesicles induced by transmembrane pH gradients”. In: *Biochemistry* 28 (1989), pp. 4181–4187. DOI: 10.1021/bi00436a009.

[273] T. E. Redelmeier, M. J. Hope, and P. R. Cullis. "On the mechanism of transbilayer transport of phosphatidylglycerol in response to transmembrane pH gradients". In: *Biochemistry* 29 (1990), pp. 3046–3053. DOI: 10.1021/bi00464a022.

[274] Y. M. Denkins and A. J. Schroit. "Phosphatidylserine decarboxylase: generation of asymmetric vesicles and determination of the transbilayer distribution of fluorescent phosphatidylserine in model membrane systems". In: *Biochimica et Biophysica Acta (BBA) - Biomembranes* 862 (1986), pp. 343–351. DOI: 10.1016/0005-2736(86)90237-3.

[275] R. Takaoka et al. "Formation of asymmetric vesicles via phospholipase D-mediated transphosphatidylation". In: *Biochimica et Biophysica Acta (BBA) - Biomembranes* 1860 (2018), pp. 245–249. DOI: 10.1016/j.bbamem.2017.10.011.

[276] B. Bloj and D. B. Zilversmit. "Asymmetry and transposition rate of phosphatidylcholine in rat erythrocyte ghosts". In: *Biochemistry* 15 (Mar. 1976), pp. 1277–1283. DOI: 10.1021/bi00651a017.

[277] A. Herrmann, A. Zachowski, and P. F. Devaux. "Protein-mediated phospholipid translocation in the endoplasmic reticulum with a low lipid specificity". In: *Biochemistry* 29 (1990), pp. 2023–2027. DOI: 10.1021/bi00460a010.

[278] H. T. Cheng and E. London. "Preparation and properties of asymmetric large unilamellar vesicles: interleaflet coupling in asymmetric vesicles Is dependent on temperature but not curvature". In: *Biophysical Journal* 100 (2011), pp. 2671–2678. DOI: 10.1016/j.bpj.2011.04.048.

[279] S. Chiantia et al. "Asymmetric GUVs prepared by MβCD-mediated lipid exchange: an FCS study". In: *Biophysical Journal* 100 (2011), pp. L1–L3. DOI: 10.1016/j.bpj.2010.11.051.

[280] L.i Lu, J. W. Schertzer, and P. R. Chiarot. "Continuous microfluidic fabrication of synthetic asymmetric vesicles". In: *Lab on a Chip* 15 (2015), pp. 3591–3599. DOI: 10.1039/C5LC00520E.

[281] M. Markones et al. "Engineering asymmetric lipid vesicles: accurate and convenient control of the outer leaflet lLipid composition". In: *Langmuir* 34 (2018), pp. 1999–2005. DOI: 10.1021/acs.langmuir.7b03189.

[282] J. Szejtli. "Introduction and general overview of cyclodextrin chemistry". In: *Chemical Reviews* 98 (1998), pp. 1743–1754. DOI: 10.1021/cr970022c.

[283] J. C. Bozelli, Y. H. Hou, and R. M. Epand. "Thermodynamics of Methyl-β-cyclodextrin-Induced Lipid Vesicle Solubilization: Effect of Lipid Headgroup and Backbone". In: *Langmuir* 33 (2017), pp. 13882–13891. DOI: 10.1021/acs.langmuir.7b03447.

[284] Z. Huang and E. London. "Effect of cyclodextrin and membrane lipid structure upon cyclodextrin-lipid interaction". In: *Langmuir* 29 (2013), pp. 14631–14638. DOI: 10.1021/la4031427.

[285] R. Hein, C. B. Uzundal, and A. Hennig. "Simple and rapid quantification of phospholipids for supramolecular membrane transport assays". In: *Org. Biomol. Chem.* 14 (2016), pp. 2182–2185. DOI: 10.1039/C5OB02480C.

[286] D. Marquardt et al. "^{1}H-NMR shows slow phospholipid flip-flop in gel and fluid bilayers". In: *Langmuir* 33 (2017), pp. 3731–3741. DOI: 10.1021/acs.langmuir.6b04485.

[287] F. A. Heberle et al. "Subnanometer structure of an asymmetric model membrane: interleaflet coupling influences domain properties". In: *Langmuir* 32 (2016), pp. 5195–5200. DOI: 10.1021/acs.langmuir.5b04562.

[288] P. Shendrik, R. Sorkin, and G. Golani. "Fusion of asymmetric membranes: the emergence of a preferred direction". In: *Faraday Discussions* 259 (2025), pp. 416–436. DOI: 10.1039/D4FD00189C.

[289] D. S. Dimitrov and M. I. Angelova. "Lipid swelling and liposome formation mediated by electric fields". In: *Bioelectrochemistry and Bioenergetics* 19 (1988), pp. 323–336. DOI: 10.1016/0302-4598(88)80013-8.

[290] Y. Yang, L. A. Serrano, and S. Guldin. "A versatile AuNP synthetic platform for decoupled control of size and surface composition". In: *Langmuir* 34 (2018), pp. 6820–6826. DOI: 10.1021/acs.langmuir.8b00353.

[291] O. Lopez-Acevedo et al. "Structure and bonding in the ubiquitous icosahedral metallic gold cluster Au 144 (SR) 60". In: *The Journal of Physical Chemistry C* 113 (2009), pp. 5035–5038. DOI: 10.1021/jp8115098.

Acknowledgements

Arriving at the end of this journey, I would like to express my deepest gratitude to all the people who have supported me throughout my PhD.

First, I would like to thank my supervisors, *Prof. Annalisa Relini* and *Dr. Ester Canepa*, for their constant guidance, valuable advice, continuous support, and trust.

I would also like to thank everyone with whom I had the pleasure of collaborating over the years on various research topics. In particular, I am grateful to *Dr. Silvia Dante* and *Prof. Giulia Rossi*. Silvia, thank you for introducing me to the use of QCM and SAXS, and for your kindness and availability. Giulia, thank you for the valuable scientific discussions and exchanges we shared.

My sincere thanks also go to *Dr. Rumiana Dimova* and *Matilde* for welcoming me into their group and making me feel part of such a stimulating and inspiring environment.

I would also like to thank all my colleagues in the biophysics lab, with whom I shared days filled with laughter, making the time spent in the lab enjoyable and the working days fly by.

Finally, I would like to thank my family and all my friends, both those who have been by my side since childhood and those I met along the way, for always being there for me and for sharing with me both the hardest and the happiest moments of these years.